DEVELOPMENT OF A MULTI-FREQUENCY BEIDOU PPP ALGORITHM

BY

Robert Galatiya Suya

A thesis submitted to the University of Nottingham for the degree of Doctor of Philosophy

JULY 2023

Abstract

BeiDou Navigation Satellite System (BDS) is a full global positioning system with multiple satellites in three different orbits. It is also equipped with the modernised frequency signals that are compatible and interoperable with other satellite systems. With these merits, BDS can now be used in positioning, navigation, and timing independent of other satellite constellations. Currently, the precise point positioning (PPP) technique has become a versatile tool for computing the receiver position. However, the inter-system biases (ISB) and hardware biases are a major concern in combined Global Navigation Satellite System (GNSS) and multi-frequency data processing. To improve data processing, this thesis aims at developing a novel multi-frequency BDS PPP algorithm.

To enhance the multi-BDS constellation, this thesis reparameterises the PPP functional model in terms of ISB and multi-GNSS precise products using two different generations of BDS satellites. The results establish an improvement in position, convergence, and pseudorange residuals. This thesis also proposes a hardware bias handling scheme based on the BDS multi-frequency signals. This is achieved by extending the traditional triple-frequency PPP model to a quad-PPP model. The experimental tests are conducted to test the validity of the proposed model, and the results reveal that the suggested model generally outperforms the traditional one in terms of the quality of the estimated position and biases. Furthermore, this work also puts forward an extended mathematical model for addressing biases emanating from BDS satellite orientation. The model deploys the satellite attitude quaternions in the modelling of BDS satellite attitude, and is validated using the standard attitude. As part of model testing, the thesis undertakes kinematic and static PPP experiments. The results uncover that the technique can upgrade positioning solutions in both modes. In addition, the approach is also capable of lowering the estimated phase residuals.

Keywords: PPP, ISB, hardware biases, satellite attitude, residuals

Acknowledgment

I am deeply grateful to all those who have played a significant role in the completion of my doctoral research. Their invaluable insights, guidance, and support have shaped my journey and the outcomes of my work.

My heartfelt thanks go to my supervisors, Dr. Yung-Tsang Chen, Dr. Chiew-Foong Kwong, and Dr. Penghe Zhang, for their unwavering dedication, profound knowledge, and insightful perspectives. Their indispensable guidance in model development and commitment to excellence have been transformative. Dr. Chiew-Foong Kwong's advice and the motivating video by Sylvester Stallone on "Never Give Up" have been invaluable in overcoming challenges and keeping me inspired in my study.

I would like to express my sincere appreciation to Dr. Craig Hancock for his fruitful suggestions in my PhD work, which have significantly refined my research. His mentorship has been instrumental in my development as a researcher.

I am grateful to Dr. Lei Yang, my second-year internal examiner, for his valuable suggestions and critical evaluation of my work, which broadened my understanding. I also extend my thanks to Dr. David Chieng, my internal assessor during the third-year annual review, for his constructive input on the GNSS signal structure and dedication to academic excellence. I also thank Dr. David Chieng for inviting me to deliver a lecture on GNSS to undergraduate students in Electrical and Electronic Engineering (EEE).

I am deeply appreciative of the resources and conducive environment provided by Dr. Yung-Tsang Chen and Dr. Chiew-Foong Kwong, which have been vital to the successful completion of my PhD.

I also wish to acknowledge the support of my colleagues, friends, and family members who have provided encouragement throughout this challenging journey. Their trust in me has been a constant source of motivation.

This journey would not have been possible without each and every one of you. Thank you for being a part of my success.

Dedication

In loving memory of my dear mother, whose presence and love continue to guide me even though she is no longer with us. Although I was in a foreign country and unable to attend her burial, her spirit, and unwavering support have remained steadfast in my heart.

Table of Contents

List of Figures

List of Tables

Acronyms and Abbreviations

AC	Analysis Centre
AI	Artificial Intelligence
Alt-BOC	Alternative Binary Offset Carrier
BDS	BeiDou Navigation Satellite System
BNSS	BeiDou Navigation Satellite System
BSSD	Between-Satellite-Single-Differencing
BPSK	Binary Phase-Shift Keying
CDMA	Code Division Multiple Access
CIO	Conventional International Origin
CLS	Collecte Localisation Satellites
CNES	Centre National d'Etudes Spatiales
CODE	Center for Orbit Determination in Europe
CoM	(Earth's) Center of Mass
CSNO	China Satellite Navigation Office
CTS	Conventional Terrestrial System
DCB	Differential Code Bias
DLR	Deutsches Zentrum für Luft- und Raumfahrt (German Aerospace Center)
DOP	Dilution of Precision
DPB	Differential Phase Bias
ERP	Earth Rotation Parameters
EWD	Epoch-Wise-Differencing

EWL	Extra Wide Lane
FCB	Fractional Cycle Bias
FDMA	Frequency Division Multiple Access
FOC	Full Operational Capability
GIOVE	Galileo In-Orbit Validation Element
GEO	Geostationary Earth Orbit
GF/IF	Geometry-Free/Ionosphere-Free
GFZ	Deutsches GeoForschungsZentrum
GIM	Global Ionospheric Map
GMF	Global Mapping Function
GLONASS	Global'naya Navigatsionnaya Sputnikkovaya Sistema (GLObal NAvigation Satellite System)
GNSS	Global Navigation Satellite System
GNSS-IR	GNSS-Interferometric Reflectometry
GPS	Global Positioning System
GRGS	Groupe de Recherche de Géodésie Spatiale
HAS	High-Accuracy Service (Galileo High-Accuracy Service)
HMW	Hatch-Melbourne-Wübbena
ICB	Initial Clock Biases
ICD	Interface Control Document
IERS	International Earth Rotation and Reference Systems Service
IF	Ionosphere Free
IFB	Inter-Frequency Bias

IFCB	Inter-Frequency Clock Bias
IFPB	Inter-Frequency Phase Bias
IGS	International GNSS Service
IGSO	Inclined Geo-Synchronous Orbit
IOV	In-Orbit Validation
JAXA	Japan Aerospace Exploration Agency
LOS	Line of Sight
MEO	Medium Earth Orbit
MGEX	Multi-GNSS Experiment
MD	Mixed Difference
MJD	Modified Julian Day
ORBEX	ORBit EXchange
OB	Orbit Normal
OSB	Observable-Specific Signal Bias
PCE	Precise Clock Estimation
PCO	Phase Center Offset
PCV	Phase Center Variation
PDOP	Position Dilution of Precision
PPP	Precise Point Positioning
PPP AR	Precise Point Positioning Ambiguity Resolution
PRN	Pseudo Random Noise
QMBOC	Quadrature Multiplexed Binary Offset Carrier
QPSK	Quadrature Phase-Shift Keying

QZSS	Quasi-Zenith Satellite System
RNSS	Regional Navigation Satellite System
RMSE	Root Mean Square Error
SBAS	Satellite-Based Argumentation Services
SED	Satellite and Epoch Differenced
SINEX	Solution (Software/technique) INdependent Exchange
SISRE	Signal-In-Space Ranging Error
SF-PPP	Single-Frequency PPP
SHAO	Shanghai Astronomical Observatory
SP3	Standard Product 3
SPP	Single Point Positioning
SVN	Space Vehicle Number
TARC	Test and Assessment Research Center of China Satellite Navigation
TUM	Technische Universität München
UCD	Uncalibrated Code Delay
UNOOSA	United Nations Office for Outer Space Affairs
UPD	Uncalibrated Phase Delay
WU	Wuhan University
YS	Yaw Steering
ZHD	Zenith Hydrostatic Delay
ZTD	Zenith Tropospheric Delay

Chapter 1: Introduction

1.1 Motivation

The booming number of satellites, improvements in satellite technology, and signal designs are persistently expanding BeiDou Navigation Satellite System (BDS) domains of application. The advances in Global Navigation Satellite System (GNSS) signal compatibility and interoperability continue to extend the margin of service availability. The increasing number of satellites among different constellations has induced technological advances in GNSS receiver technology. Moreover, the flexibility among GNSS signals, coupled with the robust and multiple frequencies in distinct GNSS constellations, equates to the hindmost goal of multi-GNSS and multi-frequency integrated processing.

Currently, the multi-GNSS Experiment (MGEX) tracking stations that can observe the modernised BDS signals are constantly being densified in order to meet the positioning, navigation, and timing (PNT) global user requirement. Thus, being recently deployed, the BDS satellites offer tremendous opportunities to exploit BDS precise point positioning (PPP). As BDS attains prominence as a feasible alternative to other established GNSS such as the Global Positioning System (GPS), GLObal NAvigation Satellite System (GLONASS or Global'naya Navigatsionnaya Sputnikkovaya Sistema), and Galileo, there is a pressing necessity to advance the BDS algorithm development to enable its widespread applications.

1.1.1 BDS Nominal Constellation

The BDS hybrid constellation consists of a Regional Navigation Satellite System (RNSS or BDS-2, formerly called the Compass) confined to the Asia Pacific region, and a BeiDou GNSS (BDS-3 or BeiDou-3) providing worldwide PNT services (Shen, 2019). Both the former and the latter constellations constitute satellites in three distinct orbits namely the Geostationary Earth Orbit (GEO), the Inclined Geo-Synchronous Orbit (IGSO), and Medium Earth Orbit (MEO) satellites. According to the China Satellite Navigation Office (CNSO, 2023), BDS has 44 pseudorandom noise (PRN, 15 BDS-2, and 29 BDS-3) codes incorporated in the operational orbital constellation as of the day of the year (DOY) 142, 2023 (22nd May 2023). Table 1.1 summarises the BDS nominal constellation. With unique features are the BDS-3S (where S denotes S-band) category of satellites that are still in-orbit validation (IOV). The BDS-3S satellites are experimental that transmit an S-band signal whose signals are in the range of 2483.5 to 2500 MHz (Montenbruck et al., 2017). In addition to the PRNs presented in Table 1.1, BDS-3 has 5 IOV PRNs including C61 (GEO), C31 (IGSO-1S), C58 (IGSO-2S), C57 (MEO-1S), and C58 (MEO-2S).

Table 1.1: Overview of BDS constellation status as of May, 2023.

Orbit	BDS-2	BDS-3	BDS-2, BDS-3
GEO	C01-C05	C59, C60	5, 2
IGSO	C06-C10, C13, C16	C38-C40	7, 3
MEO	C11, C12, C14	C19 - C25, C26-C30, C32, C33, C34-C37, C41-C43, C44-C46	3, 24

Aimed at providing first-class navigation, timing, and data communication services, The People's Republic of China successfully completed the commissioning of its modernised BDS-3 satellites in June 2020 (CNSO, 2020). As a result of the fusion of BDS-2 and BDS-3 satellites, service availability is currently more than 99% in both the Asia-Pacific region

and worldwide. Currently, the visible number of BDS-2 and BDS-3 satellites can reach up to 16 (Figure 1.1).

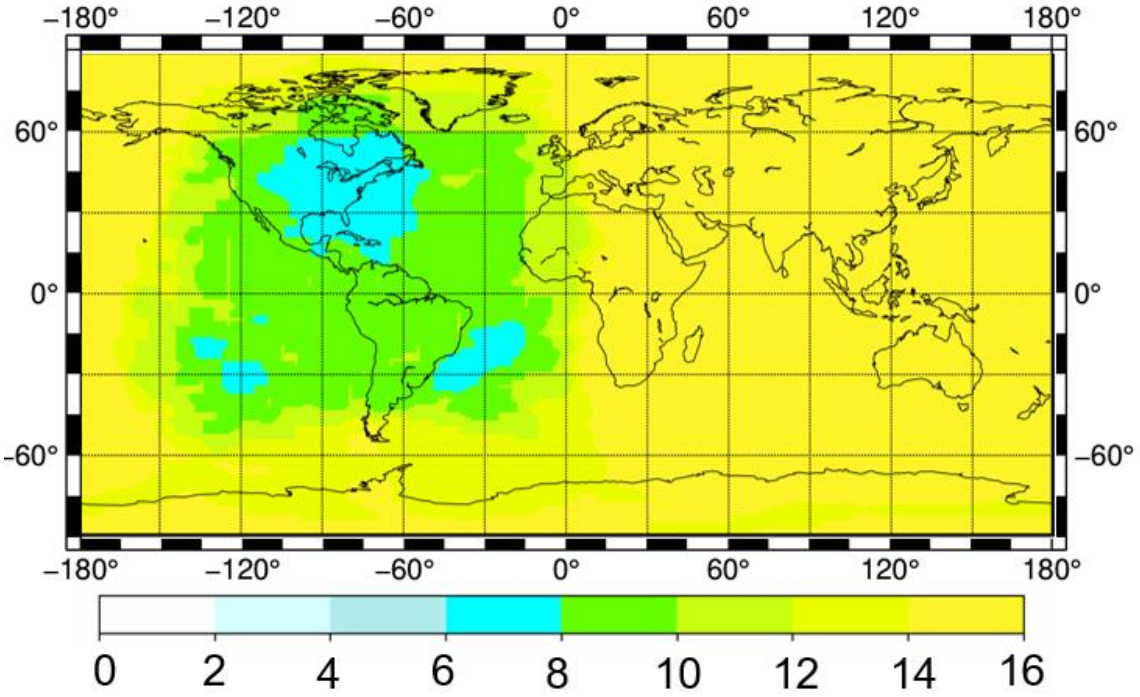

Figure 1.1: BDS visible number of satellites on May 23, 2023.

1.1.2 BDS Navigation Signals

In addition to the increased number of satellites, both BDS-2 and BDS-3 satellites also have multi-frequency broadcasting capability. According to Lu et al. (2019), the BDS-2 satellites transmit three navigation signals in three different frequency bands (B1I, B2I, and B3I), of which B2I is equivalent to E5b of Galileo. The in-phase (I) and quadrature (Q) components are used to modulate the carrier frequency using a ranging code chip rate of either 2.046 or 10.23 Megachips per second (Mchip/s). All the BDS-2 signals are modulated with the Binary Phase-Shift Keying (BPSK) modulation scheme.

Unlike BDS-2, the modernised BDS-3 satellites broadcast six public service signals, namely B1I, B3I, B2a+b, B2a, B2b, and B1C. The B2a+b is also specified as B2(B2a+B2b). The BeiDou-3 B1I uses a different modulation mode (BPSK) to its counterpart BeiDou-2 B1I signal. The modernised signal B2a+b utilises the asymmetric constant envelope binary offset carrier (ACE-BOC). More details about the properties of the ACE-BOC modulation scheme can be found in Yao et al. (2016). The rest of the BDS-3 signals employ BPSK modulation with B1C signal utilising Quadrature Multiplexed Binary Offset Carrier (QMBOC) as an additional modulation mode. Table 1.2 outlines an overview of the signal structure for BDS-2 and BDS-3, as summarised from CNSO (2019). To enhance signal compatibility with other GNSS, BI-C is interoperable with GPS L1C signal (CNSO, 2017).

Table 1.2: Overview of navigation signals for BDS-2 and BDS-3 satellites.

Constellation	Band	Frequency [MHz]	Wavelength [cm]	Chip rate [Mcps]	Modulation
BDS-2	B1I	1561.098	19.20	2.046	BPSK
	B2I	1207.140	24.83	2.046/10.23	BPSK
	B3I	1268.520	23.63	10.23	BPSK
BDS-3	B1I	1561.098	19.20	2.046	BPSK
	B1C	1575.420	19.03	1.023/2.046	QMBOC
	B2a	1176.450	25.48	10.23	QPSK
	B2b	1207.140	24.83	10.23	QPSK
	B2a+b	1191.795	25.15	15/10	ACE-BOC
	B3I	1268.520	23.63	10.23	BPSK

Besides the navigation signals outlined in Table 1.2, BDS has other special signals for the PPP and Satellite-Based Argumentation Services (SBAS) services. The two services are offered by GEO satellites specifically designed to broadcast on B2b and B2a/B1C service signals, respectively. Furthermore, it is worth mentioning that all the types of BDS-2 satellites are fitted with rubidium atomic clocks (CSNO, 2019). In the case of BDS-3

satellites, about 44% are equipped with spaceborne hydrogen maser clocks whereas the rest (56%) are equipped with rubidium atomic clocks just like BDS-2 satellites.

To further advance BDS-3 signal compatibility, B2a/L5/E5a, B1C/L1/E1, and B2b/E5b frequencies for BDS, GPS, and Galileo overlap. Out of the five, B1I and B3I signals are returned in the BDS-3 satellites whereas B1C, B2a, and B2b are new signals for MEO and IGSO modernised BDS-3 satellites. In addition to the five frequency signals, there is also a Bs (2483.5-2500 MHz) carrier frequency in the s-band for the BDS-3 modernised satellites (Montenbruck et al., 2017). With the decommissioning of BDS-2 satellites, B2a will gradually replace the B2I signal (CSNO, 2019).

1.2 Research Objectives

From the discussion above, it can be discerned that BDS is both a multi-constellation and multi-frequency navigation system with potential promising PNT benefits. In response to this, the central focus of this research is to develop a multi-frequency BDS PPP algorithm. In order to achieve the overall goal, the specific objectives to be addressed are as follows:

- To investigate the ISB between BDS-2 and BDS-3 constellations.
- To model the physical factors that cause hardware biases in BDS constellations.
- To develop a rigorous mathematical method for estimating BDS hardware biases emanating from satellite orientation.

1.3 Problem Statement

A limited number of BDS-2 satellites has been providing reliable PNT services within the Asia-Pacific region since its full operational capability (FOC). The emergence of BDS-3,

BDS-3S, and BDS-3e (experimental) satellites continues to not only supplement the service area, but also to complement the overall global PNT services alongside the other navigation systems. As such, different combinations of BDS GEO, IGSO, and MEO satellites have always been integrated to improve PPP performance. Furthermore, establishing the contribution of BDS-3 new-generation satellites to BDS-2 has diversified the portfolio of PPP research between the three types of BDS satellites. Consequently, researchers in the GNSS community have resorted to pursuing studies in the realm of BDS frequency combinations, satellite combinations, and precise products.

Taking advantage of the modernised BDS frequency signals, single-, and multi-frequency BDS PPP are a given example of the research interest among researchers (for example, Li et al., 2019; Shi et al., 2021). What is relevant is that multiple BDS frequencies allow unique signal combinations with exceptional properties. While the BDS signal structure permits multi-frequency combinations, hardware biases are inevitable among GEO, IGSO, and MEO BeiDou satellites reaching up to a few decimetres. Moreover, the combined BDS-2 and BDS-3 processing also attracts an ISB. Such biases impair GNSS positioning performance if not properly treated in data processing.

Different attempts have been reported in the literature to estimate hardware biases (e.g.: Ye et al., 2018; Zhang et al., 2019; Li et al., 2020). However, the overall PPP improvement integrating the three types of BDS satellites from both navigation systems has not been investigated in detail. The techniques are based on the traditional dual-frequency PPP model, and may be deficient in addressing the advances in BDS satellites and signal structure. Therefore, with the booming influence of BDS robust signals and the modernised satellites on PPP, bias estimation is thus a worthy motivation to refine in terms of algorithm development.

1.4 Summary of Contributions

From Sections 1.2 and 1.3, the key contributions of this PhD work can be summarised as follows:

- **ISB Parameterisation using Different MGEX Products**

The influence of the ISB on PPP has been investigated comprehensively in consideration of the different MGEX precise products. Since high-quality MGEX products are crucial for multi-constellation PPP, precise orbits and clock products that support GEO, IGSO, and MEO have been accounted for. A PPP functional model has been parameterised in terms of ISB and MGEX precise products using the BDS-2 and BDS-3 observations. Before validating the impact of the ISB on PPP, the MGEX products are intensively scrutinised in order to recommend an optimal processing scheme for the BDS datasets.

- **Formulation of a Hardware Bias Handling Scheme**

Heterogeneous receivers track multiple signals from different GNSS constellations. When these signals are combined in data processing, the solution is not only affected by systematic errors but also hardware biases that impair the overall positioning performance. In response to that, the existing triple-frequency PPP technique for estimating biases is extended to the quad-frequency PPP model. The mathematical relation between the traditional method and the proposed one has been rigorously proved and validated using BDS and Galileo observations.

- **Bias Modelling Based on the Satellite Attitude Quaternions**

This thesis develops an extended model for characterising biases based on the satellite attitude. The work also investigates the effect of considering satellite attitude quaternions in BDS data processing. Coupled with the advent of integer clocks, this research thoroughly establishes the potential effect of these products on PPP solutions. Moreover, weighting

schemes suitable for handling BDS satellites in three different orbits are proposed. Then, numerical verification is undertaken to support the technique using raw observation datasets.

Publications arising from this Thesis

- **Journal Papers**

Suya, R. G., Chen, Y.-T., Kwong, C.F., and Zhang, P. (2022) 'BeiDou intra-system bias using different precise orbit and clock products', Measurement: Journal of the International Measurement Confederation. Elsevier Ltd, 191(January), p. 110804. doi: 10.1016/j.measurement.2022.110804.

Suya, R.G., Chen, Y.T., Kwong, C.F. and Zhang, P., (2023) 'Enhancing BDS-3 PPP-AR with observable-specific signal biases'. Measurement Science and Technology, 34(12), p.125911. DOI 10.1088/1361-6501/acf8e4

Suya, R. G., Chen, Y.-T., Kwong, C.F., and Zhang, P. (2023) 'Satellite Orientation Modelling with Quaternions and its impact on BDS/Galileo PPP-AR', Measurement: Journal of the International Measurement Confederation. Elsevier Ltd (Under review)

- **Peer-reviewed Conference Papers**

Suya, R. G., Chen, Y.-T., Kwong, C.F., Zhang, P., & Hancock, C. M. (2021) 'The Contribution of BeiDou-3 Binary Offset Carrier Signals to Single Point Positioning', in FIG e-Working Week 2021 Smart Surveyor for Land and Water Management - challenges in a new reality, 21–25 June 2021. Copenhagen, Denmark: FIG. Available at: https://fig.net/fig2021/technical_program.htm.

Suya, R. G., Chen, Y.-T., Kwong, C.F., and Zhang, P.(2022) 'Considering Satellite Attitude Quaternions in BeiDou Precise Point Positioning Performance', EGU General Assembly 2022, Vienna, Austria, 23–27 May 2022, EGU22-12926, https://doi.org/10.5194/egusphere-egu22-12926, 2022.

Suya, R. G., Chen, Y.-T., Kwong, C.F., and Zhang, P. (2022) 'Noise Characterization in BeiDou-3 Multi-Frequency Observables', in XXVII FIG Congress, Volunteering for the future-Geospatial excellence for a better living. Warsaw, Poland: FIG, pp. 11–15. Available at: https://www.fig.net/fig2022/technical_program.htm.

1.5 Thesis Outline

This thesis is organised into six Chapters arranged as follows:

Chapter 2 presents research work on biases reported extensively in different literature. The distinctive characteristics of biases including their estimation method in PPP are discussed.

Chapter 3 highlights the proposed ISB parameterisation using the BDS constellation. The implementation of the estimation method is thoroughly discussed.

Chapter 4 focuses on the hardware bias handling scheme in a multi-frequency BDS system. The mathematical model for estimating hardware biases is developed and validated using the traditional technique.

Chapter 5 deals with the reparameterisation of BDS observations that considers satellite attitude quaternions.

Chapter 6 summarises the research work presented in this thesis, and suggests the potential research directions based on the un-addressed issues in this work.

Chapter 2: Theoretical Framework for Bias Parameter Estimation

2.1 Introduction

Biases in multi-constellation and multi-frequency data processing have a significant influence on the overall performance of the estimated parameters. Hence, this chapter first classifies and reviews the methods for the estimation of biases, then highlights their theoretical comparison. Moreover, the treatment of such biases in multi-GNSS data processing is discussed before summing up the chapter with relevant weaknesses in the existing methods.

2.2 Biases in GNSS Constellations

In GNSS data processing, biases need to be accounted for to achieve robust and reliable results. During data processing, the biases can either be modelled or eliminated. Before exploring the different methods for treating such biases, it is necessary to carefully categorise the biases for different observables. Currently, the existing literature does not provide a clear categorisation of biases. However, this thesis endeavours to classify them as shown in Figure 2.1.

The MGEX clock correction applied to GNSS observables during data processing contains code biases that are, in turn, introduced into carrier phase observables. Then both biases, the code and phase, lump with other parameters such as the ionosphere delay, clock parameters, ambiguity parameter, or the residuals (Geng et al., 2010). In addition to this characteristic, understanding the terminology of biases and their associated nomenclature is also important in data processing. For instance, the code biases are known by different names such as differential signal biases (DSB); differential code biases (DCB); uncalibrated code delay (UCD); fractional cycle biases (FCB); code inter-frequency clock

biases (IFCB), or code observable-specific signal bias (code OSB). Similarly, the phase biases have distinct names such as differential signal biases (DSB); differential phase biases (DCB); uncalibrated phase delay (UPD); FCB; phase IFCB, or phase observable-specific signal bias (phase OSB).

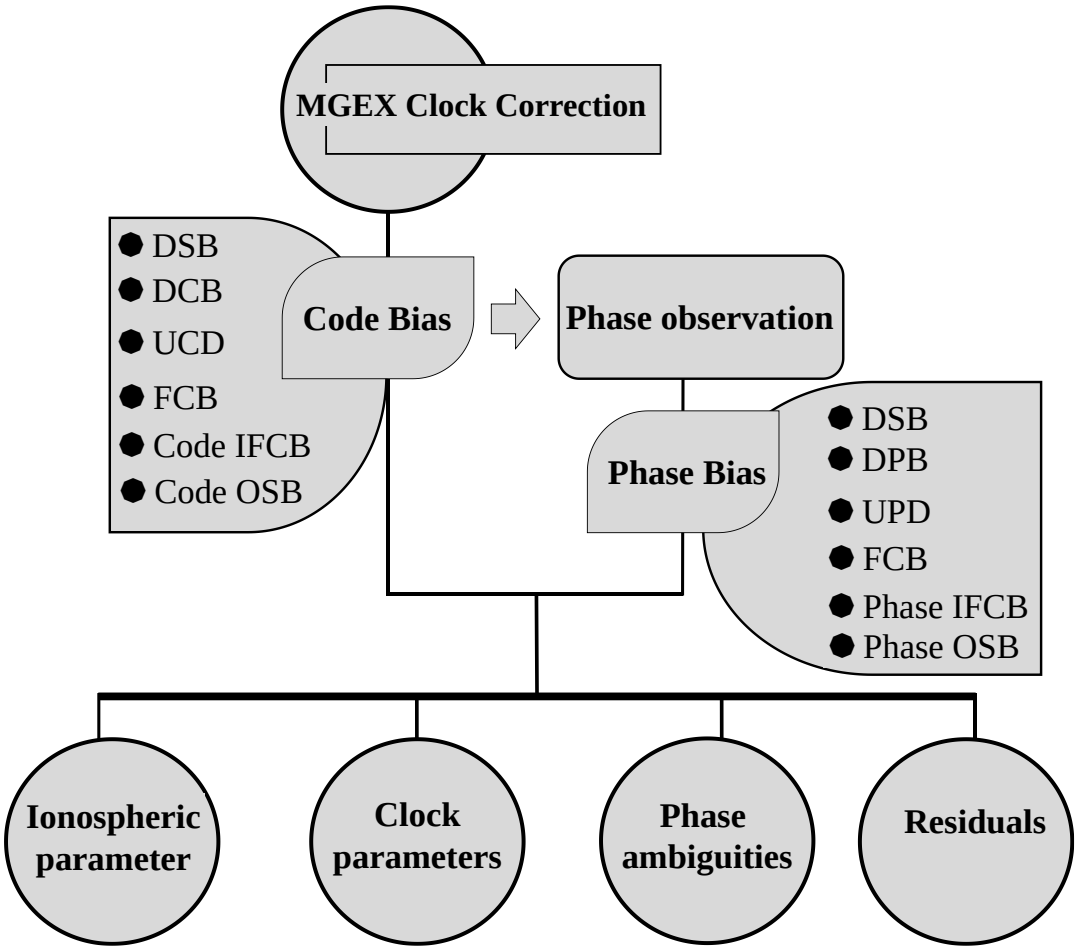

Figure 2.1: Classification of biases in GNSS observations.

The modernised BDS multi-frequency signals, coupled with the three kinds of satellites in MEO, IGSO, and GEO orbits, are increasing the research dimension in the GNSS community. With multiple BDS frequencies, a considerable volume of research has

followed in different fields such as multipath, signal-to-noise ratio (SNR), GNSS interferometric reflectometry (GNSS-IR), quality of BDS products, GNSS products, low-cost sensors, artificial intelligence (AI), and precise time transfer. Even though the research work targets distinctive aspects of BDS, all have a central focus on the overall PNT accuracy. Figure 2.2 provides an overview of the current BDS research as of December 2022.

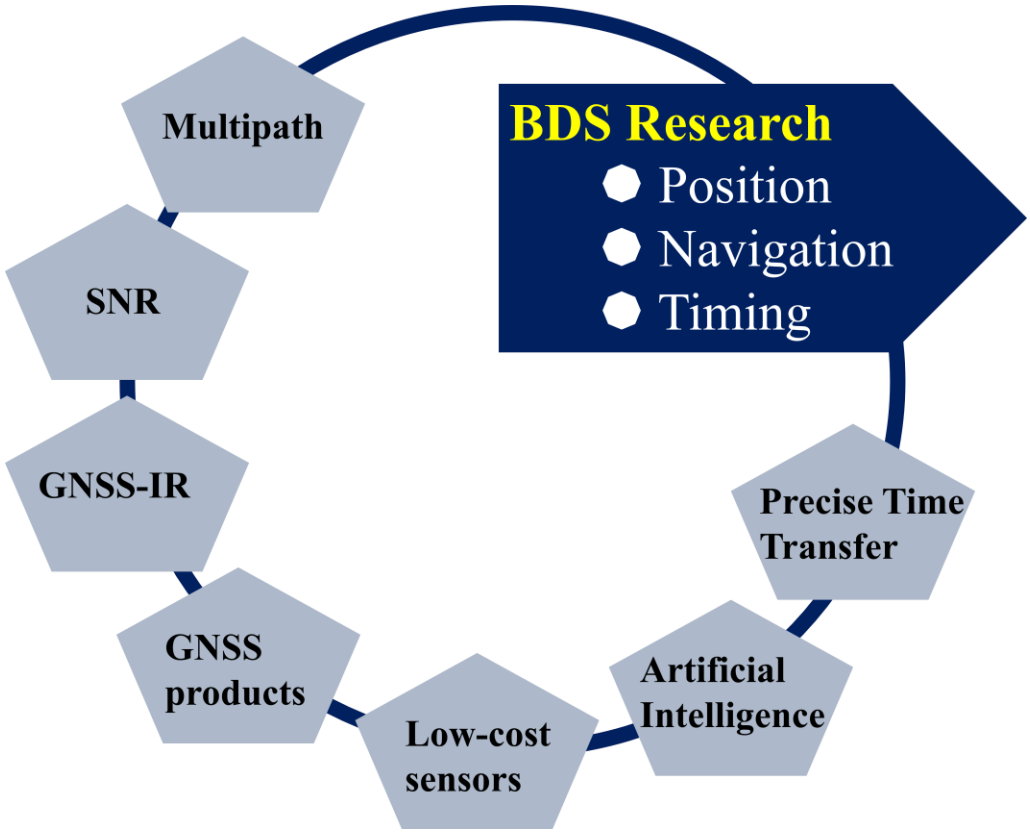

Figure 2.2: Overview of BDS research impact.

It is obvious that the positioning solution can benefit from BDS combined signals. While the positioning accuracy can leverage on BDS multiple frequencies, hardware biases tend to be a setback on the positioning performance. Thus, in order to achieve accurate positioning results, all positioning errors and biases should be accounted for (Gleason and

Gebre-Egziabher, 2009) in high-precision positioning such as PPP (Torre and Caporali, 2015).

Furthermore, as opposed to the conventional dual-frequency PPP model (Zumberge et al., 1997), in BDS triple-frequency combination, there exist IFCB between B1I/B2I and B1I/B3I IF phase observables. The IFCB are primarily caused by the inconsistency in the frequency-variant hardware delays within the satellite (Montenbruck et al., 2013). When the clock solutions provided are equivalent to the IF combinations incorporated in satellite clock estimation, hardware biases cancel out. This cancellation is feasible for only code and phase IF dual-frequency linear combinations. However, the biases may not be neglected when triple-frequency satellite observations are used, and they come from different sources. The IFCB may originate from temperature (Montenbruck et al., 2012), satellite phase delay, or poor clock modelling (Wanninger and Beer, 2015).

Current studies indicate that the IFCB between B1/B2 and B1/B3 IF satellite clocks can have peak-to-peak amplitude reaching up to 0.04 m (Zhao et al., 2016). As demonstrated by Montenbruck et al. (2012), the IFCB have a cyclic variation in the period of the signal with respect to the earth-spacecraft-sun geometry. Specifically, the periodic fluctuations depend on the altitude of the sun with respect to the orbital plane of the satellite.

The BDS hardware delays have been studied targeting both the receiver and satellite. Since the onset of BDS global PNT services, a combined BDS-2/BDS-3 PPP experiment has been carried out to determine the receiver time delay bias (Jiao et al., 2019). BDS receiver phase biases have been estimated using heterogeneous GNSS receivers with MEO and IGSO triple-frequency signals (Li et al., 2018) and both triple- and dual-frequency signals broadcast by BDS MEO, IGSO, and GEO satellites (Gu et al., 2015; Guo et al., 2016). Moreover, the lack of meticulous consideration of IFCB in BDS B1I/B3I PPP resulted in millimetric accuracy as compared to the conventional B1I/B2I PPP solution (Zhao et al., 2017). Generally, the existence of IFCB between B1I/B2I and B1I/B3I makes it unsuitable

to utilise a set of BDS satellite clock products for data processing across all frequency signals.

2.3 Existing Methods for Estimating BDS Hardware Biases

Techniques have been reported in the literature with proper accounts on the treatment of hardware biases in both floating and ambiguity-fixed solutions. For both scenarios, the overall hardware bias handling schemes are generally similar for all signals based on code division multiple access (CDMA) such as GPS, Galileo, and BDS (Geng et al., 2010; El-Mowafy et al., 2016) and on frequency division multiple access FDMA (Geng and Bock, 2016; Liu et al., 2017). Out of the methods for estimating UPD and UCD, the solid ones can be generalised as threefold: the geometry-free/ionosphere-free (GF/IF) strategies (Fan et al., 2019), the epoch-wise differenced (EWD) technique (Ye et al., 2018), and satellite clock estimation (Guo and Geng, 2018).

Montenbruck et al. (2012) noticed the incompatibility in multipath among code and phase observations based on L1, L2 and L5 for the Block IIF-1 (SVN62) satellite. Eventually, the IFCBs were estimated using the difference among a set of IF linear phase observables Φ_f ($f = 1, 2, 3$) between L1/L2 and L1/L5, that is

$$\left.\begin{aligned}\Delta\Phi_f &= \Phi_{\Delta 12} - \Phi_{\Delta 15} \\ &= \left(\frac{f_1^2}{f_1^2 - f_2^2} - \frac{f_1^2}{f_1^2 - f_5^2}\right).\Phi_1 - \left(\frac{f_2^2}{f_1^2 - f_2^2}\right).\Phi_2 + \left(\frac{f_5^2}{f_1^2 - f_5^2}\right).\Phi_5\end{aligned}\right\} \quad (2.1)$$

Equation (2.1) can directly estimate IFCB between L1/L2 and L1/L5 in a general clock estimation procedure alongside ambiguity parameters as

$$\Delta\Phi_f = IFCB_{i,15}^{k} + (N_{IF} + \delta_{i,j}^{k}) \tag{2.2}$$

where $IFCB_{i,15}^{k}$ denotes the IFCB between L1/L2 and L1/L5; i and k denotes the receiver and satellite, respectively; N_{IF} denotes the IF carrier phase ambiguity that has absorbed time-invariant phase biases of the satellite and receiver (Geng et al., 2010), the parameter N_{IF} in Equation (2.2) contains IF combinations of $N_{IF,12}$ and $N_{IF,15}$, which are for Φ_1 and Φ_2, and Φ_1 and Φ_5, respectively; $\delta_{i,j}^{k}$ denotes the linear combination of satellite (δ_j^k) and receiver ($\delta_{i,j}$) hardware biases such that $\delta_j^k = \delta^k + \delta_{i,j}$. The estimated IFCB were observed to vary with the earth-spacecraft-sun geometry. Taking advantage of the periodicities in the signal, a harmonic function was applied to characterise the time-dependent variations between triple-frequency observables. The harmonic functions are computed from the following formulation as in Montenbruck et al. (2012):

$$\left.\begin{aligned} f(t) = a + \sum_{i=1}^{n} [C_i.cos(i\,\omega) + S_i.sin(i\,\omega)] \\ t = 0 \sim 24h \end{aligned}\right\} \tag{2.3}$$

where a denotes a constant part of the IFCB; n denotes the degree of the harmonic function. The order of the harmonic function depends on the characteristics of the observable for a particular GNSS. For example, Montenbruck et al. (2012) used a 4th order function to model the clock variations in Block IIF-1 GPS satellites. In a related study, Pan et al. (2017) applied a 6th order in an empirical study to model the clock biases in real-time PPP scenario By comparing the two orders of functions, the higher order outperformed the lower order, especially during the eclipsing phase; ω denotes the angle between the earth, satellite, and sun referenced from the point of least earth-satellite-sun angle; C_i and S_i denote the

coefficients for cosine and sine, respectively. Figure 2.3 illustrates the GNSS satellite orientation. The figure shows the angles that describe the alignment of the Sun, earth, satellite, and orbital plane. The X, Y, and Z vectors represent the axes satellite-fixed coordinate system. As indicated in Montenbruck et al. (2015), this type of satellite attitude is called nominal yaw-steering mode. Further details about this figure are given in Chapter 5.

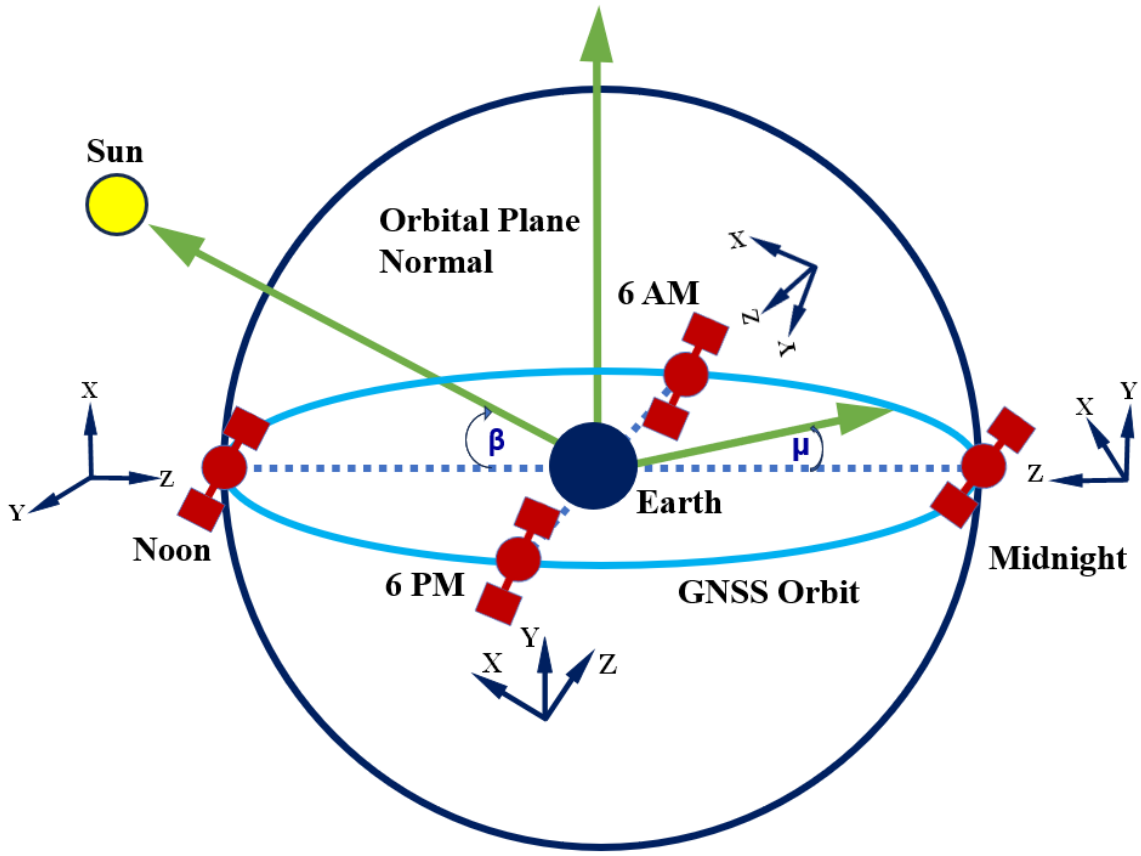

Figure 2.3: GNSS satellite orientation.

The estimated IFCB using Equation (2.2) can be improved using the harmonic function, Equation (2.3). However, frequent updating is required in order to maintain better accuracy. To test the validity of Equations (2.1), (2.2), and (2.3) an eight-month dataset was used by Montenbruck et al. (2012) which may not be enough to fully demonstrate long-term IFCB characteristics. Other researchers have also tested the harmonic function in a quest of estimating the satellite-specific UPD (e.g., Li et al., 2016).

With BDS triple-frequency measurements, the IFCB are also evident when IF code and phase observations involving B1I/B2I and B1I/B3I signals are employed in satellite clock estimation. Using the sinusoidal angle between the sun, satellite, and the earth to predict the satellite IFCB, the first two research works reported an IFCB modelling precision of about 2 cm for BDS-2 GEO satellites. Besides that, the efforts dedicated to determining BDS-2 satellite IFCB are also reported in Montenbruck et al. (2013) and Zhao et al. (2016), of which both agree on the time-dependent satellite IFCB variation of about 40 mm. On the other hand, a marginal variation in BDS-3 satellite IFCB is registered in Pan et al. (2017).

It is worth mentioning that for different GNSS signals, some carrier frequencies do not show significant variations in the estimated biases, for example, those of Galileo In-Orbit Validation Element (GIOVE, Schönemann et al., 2011). On the contrary, periodic variations reaching up to a few decimetres were unveiled in the modernised GPS L5 and the legacy L1/L2 signals (Montenbruck et al., 2012).

Despite that Equation (2.2) can directly estimate IFCB, the estimation of the ambiguity parameters makes the overall processing computationally challenging. To improve the efficiency of the approach, two techniques based on epoch-wise-differenced (EWD) and satellite and epoch-differenced (SED) observations were proposed, which can eliminate the ambiguities and efficiently estimate the IFCB (Li et al., 2013). However, the elimination of ambiguities is possible when there are no cycle slips in the computation process. For clarity, the EWD and SED techniques can be described as

$$IFCB^k(t) = \sum_{j=t_0+1}^{t} \nabla IFCB^k(j) + IFCB^k(t_0) \tag{2.4}$$

where $\nabla IFCB^k(j)$ denotes the EWD IFCB at epoch j; $IFCB^k(t_0)$ is the IFCB at reference epoch t_0 and it essentially denotes the time-independent phase bias; j denotes the sum of epochs between the reference epoch (t_0) and t. Therefore, to deduce the IFCB, the overall IFCB estimation is achieved by initialising a pivot satellite to zero (Li et al., 2012). Hence, the IFCB is determined as the accumulated value from the reference satellite. Coupled with the harmonic function, Equation (2.3), the former technique has also been used in estimating and modelling IFCB for both GPS and BDS constellations (Li et al., 2018). In these research work, one-week short-term predictions of IFCB were carried out for both GPS and BDS satellites where a prediction accuracy of at least 1.2 cm was achieved in each constellation. The Equation (2.4) incorporates the EWD and SED approaches. The EWD is based on time, while the SED differences the observations made by the satellites in addition to the differencing of the observations of adjacent epochs. This is performed to remove ambiguities and receiver clock effects. The techniques have an advantage in that they reduce the computation burden imposed by such parameters, because the number of estimated parameters is reduced.

To further improve the robustness of the EWD estimation method, Ge et al. (2012) formulated the mixed differenced (MD) approach which combines the EWD and the undifferenced (UD) techniques. The advantage of this method is that it can be used to estimate the EWD clocks and initial clock biases (ICB) using differenced phases and undifferenced observations, respectively. Besides that, the MD approach is the first attempt to reduce the effect of ICB on range measurements, thereby retaining efficient computational capability. This makes the MD technique ideal for real-time clock estimation alongside the EWD phase and UD range. Moreover, the comparison of clocks estimated from the MD, UD, and EWD techniques agree well except for a minor difference

with the UD method of about 0.20 ns (Ge et al., 2012). The major distinction among the three techniques occurred when satellites are in the eclipse phase. This was attributed to inaccurate satellite altitude models during eclipse time, especially in the EWD technique.

All the techniques highlighted above employed phase data in the estimation of IFCB, thereby making the estimable to be independent of hardware delays emanating from code observations. It is obvious that such phase-based IFCB in conjunction with dual-frequency satellite clocks will eventually introduce systematic biases into code residuals when incorporated in triple-frequency using IF observations (Hauschild and Montenbruck, 2009). To avoid such biases, Li et al. (2016) integrated both code and phase observations in the estimation of IFCB. Similar studies where code and phase observations are combined to estimate phase hardware biases are also reported in other literature (Senior et al., 2008). In the same vein, Guo and Geng (2018) estimated the hardware biases assimilated in the GPS L5 together with the L1/L2 clock using the UD phase. In their research work, the possibility of converting the UD L5 clocks to L1/L5 by combining L1/L2 and L5 clock solutions was examined. Specifically, the study theoretically demonstrated the possibility of directly computing the IF L1/L5 clock biases using a scale factor. In a simple case

$$\left.\begin{aligned} IFCB^{k}_{IF,15} &= IFCB^{k}_{UC,5}.\left(\frac{1}{\tau_2}\right) \\ \tau_2 &= \frac{-f_5^2}{f_1^2 - f_5^2} \end{aligned}\right\} \tag{2.5}$$

where $IFCB^{k}_{IF,15}$ denotes the IFCB between the L1/L2 and L1/L5 clocks; $IFCB^{k}_{UC,5}$ denotes the IFCB between the L5 and L1/L2 clocks, and $(\frac{1}{\tau_2})$ denotes the scaling factor.

2.4 Theoretical Comparison of the Hardware Bias Estimation Methods

The EWD, satellite clock-based approach, and the GF/IF methods are widely used for estimating IFCB in GNSS data processing. For instance, the triple-frequency PPP models are used for UPD estimation with respect to any of the three techniques. The only exception is that the UD techniques perform better in practice than the conventional IF approaches in the estimation of IFCB. Some results on the difference in performance between these two techniques are presented in Guo and Geng (2018). On the contrary, the EWD method is preferred for its processing efficiency, for example in Zhang et al. (2011). Furthermore, the improved version of the EWD model is the mixed-differenced (MD) technique which is simply an amalgamation of the EWD and the UD approaches (Ge et al., 2012). Moreover, as noted by Ye et al. (2018), it is worth indicating that the IFCB emanating from MD and the UD model are equal in terms of the magnitude of the estimated biases. Thus, the IFCB can optionally be estimated using either the MD or the UD techniques. Table 2.1 compares the different methods for estimating hardware biases.

Table 2.1: Overview of techniques for estimating hardware biases.

Technique	**Measurement Approach**	**Estimable**	**Remarks**	
Two IF linear carrier-phase combinations	▪ Differencing IF observations (e.g.: B1I/B2I and B1I/B3I) to estimate phase biases	▪ Direct estimation of biases ▪ Estimation of ambiguity terms	▪ Suitable for clock analysis; ▪ Computational burden due to the estimation of ambiguity parameters	(Montenbruck et al., 2013; Zhang et al., 2017)
ED technique using phase observations	▪ Differencing IF observations to estimate phase biases ▪ Difference out ambiguities	▪ Efficient estimation of biases	▪ Independent of hardware biases within code observations ▪ Systematic biases within code residuals	(Li et al., 2013; Zhang et al., 2019)

			on B1I/B3I IF observation	
ED technique using both code and phase measurements	▪ Differencing IF observations to estimate phase biases ▪ Difference out ambiguities	▪ Efficient estimation of code biases ▪ Efficient estimation of phase biases	▪ Use code observations to argument the estimation of biases	(Li et al., 2016; Ye et al., 2018)
SED technique using phase observations	▪ Differencing IF observations to estimate phase biases ▪ Difference out ambiguities	▪ Efficient estimation of biases	▪ Independent of hardware biases within code observations ▪ Systematic biases within code residuals on B1I/B3I IF observation	(Li et al., 2012; Li et al., 2013)
UD technique	▪ Differencing satellite clock estimates (e.g.: B1I/B2I and B1I/B3I) ▪ UD IFCB estimated between B1I/B2I and B3I ▪ B3I is converted to B1I/B3I using the DCB	▪ IFCB are estimated based on triple-frequencies	▪ Ignores time-dependent hardware biases in processing ▪ Hardware biases on the third signal are absorbed by the residuals	(Guo and Geng, 2018)
MD technique	▪ Combines the UD and ED techniques ▪ Differencing satellite clock estimates (e.g.: B1I/B2I and B1I/B3I) ▪ Difference out ambiguities	▪ Estimation of epoch differenced clocks using differenced phases ▪ Estimation of ICB using undifferenced observations ▪ Estimation of epoch differenced Zenith Tropospheric Delays (ZTD) using differenced phases	▪ Receiver clocks are eliminated by between-satellite-single-differencing (BSSD) ▪ Receiver initial biases are eliminated by BSSD.	(Zhang et al., 2007; Ye et al., 2018)

Apart from computational efficiency, the first major difference between the IF/GF and EWD methods is that the former estimates phase biases together with ambiguity parameters. The second difference lies in that the EWD technique is more computationally efficient than the IF/GF due to the elimination of ambiguity terms. On the other hand, both the IF/GF and EWD techniques are outweighed by the MD technique in terms of computation time. Nonetheless, the EWD and IF/GF approaches do not estimate ionospheric delay parameters in the estimation process which is not the case with the UD technique.

In addition to the different methods for estimating hardware biases in Table 2.1, the working terminology of the hardware bias estimation approaches is summarised in Figure 2.4. From this figure, the major difference between the PPP and PPP-RTK (real-time kinematic) methods lies in the treatment of biases with respect to other parameters. As for the IF-PPP technique, the biases are lumped with other parameters, whereas in PPP-RTK techniques the biases are not lumped with other parameters. In network-based PPP, the hardware biases, FCB, and Hatch–Melbourne–Wu¨bbena (HMW) biases are estimated in the network solution and then made available to the single-user for various applications.

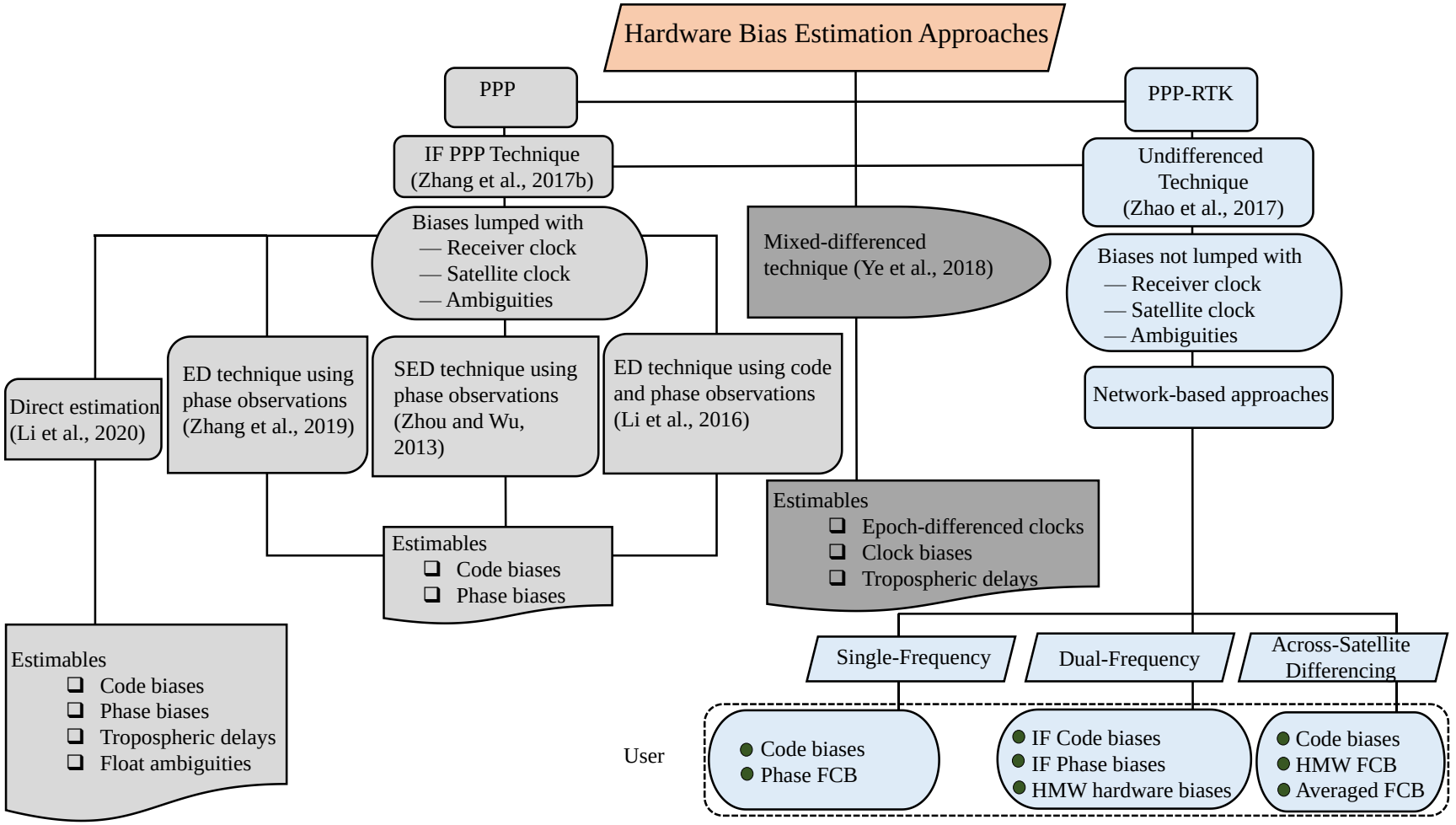

Figure 2.4: Summary of hardware bias estimation methods.

2.5 Remarks on the Existing Methods for Treating Biases

From the review above, the IFCB can be estimated with the IF/GF, EWD, UD, or MD techniques. The IFCB can be computed directly using the GF/IF observations. Regardless of the method used, the hardware bias lumped with other parameters will always have an effect on that parameter. For instance, the biases lumped with the clock will affect the estimated clock solution. Similarly, those that lump with the ionosphere or the ambiguity parameters will affect such parameters, too.

The characteristics of the original parameters change when they combine with the biases. While this is true, it is also worth noting that different types of biases have different properties. For instance, the phase biases are frequency-dependent whereas the code biases are not. Despite this difference, both biases are affected by atmospheric conditions. Moreover, they also vary with time, and they depend on the satellite and receiver. Currently, the estimation methods reported in literature are silent on the treatment of biases using multi-frequency signals such as quad- or five frequencies. Hence, the underlying influence of such biases on the positioning performance needs to be established using the BDS modernised satellites and multi-frequency signals.

Since phase observations are noisier than code measurements, a proper weighting scheme is required to properly model the observations from multiple satellites. While exploiting on observations from multiple satellites, the potential pitfall underlying the earth-spacecraft-sun geometry needs to be re-visited for the BDS constellation which comprises satellites in different orbits. One justification for conducting such an evaluation is to enable accurate modelling of BDS satellites during eclipse periods. This is so because the receiver and satellite biases lumped with the ambiguity parameters impede ambiguity resolution in high-precision GNSS.

Combining observations from two different GNSS such as BDS-2 and BDS-3 requires proper treatment of the ISB. Different researchers treat the ISB differently in different combinations of satellite systems. Currently, a number of agencies generate precise

products necessary for GNSS data processing. However, there is limited research work that relates the quality of such products to the BDS-2 and BDS-3 ISB and its impact on the solution. Therefore, the influence of the ISB needs to be revisited in terms of parameterisation and experimental validation in a multi-GNSS scenario such as BDS-2 and BDS-3 constellations. In addition to the deficit in the estimation method, the root cause of the ISB also needs to be established.

2.6 Inter-System Biases in Multi-GNSS Constellations

In multi-GNSS data processing, the knowledge of ISB becomes crucial, especially when an optimal solution is required. The knowledge of the ISB becomes necessary when estimating the receiver clock in GNSS data processing. During the clock estimation involving observations from multiple global or regional navigation satellite systems, two approaches are commonly used in combined data processing. The first approach estimates one receiver clock for all the GNSS involved in a multi-scenario, and an ISB between GPS (G) and any other system such as Galileo (E), BDS-2 (C), BDS-3 (B), and GLONASS (R). The other technique estimates the receiver clock for each individual constellation. The schematic drawing below (Figure 2.4) demonstrates the estimated parameters when the first (Method A) and second approaches (Method B) are used.

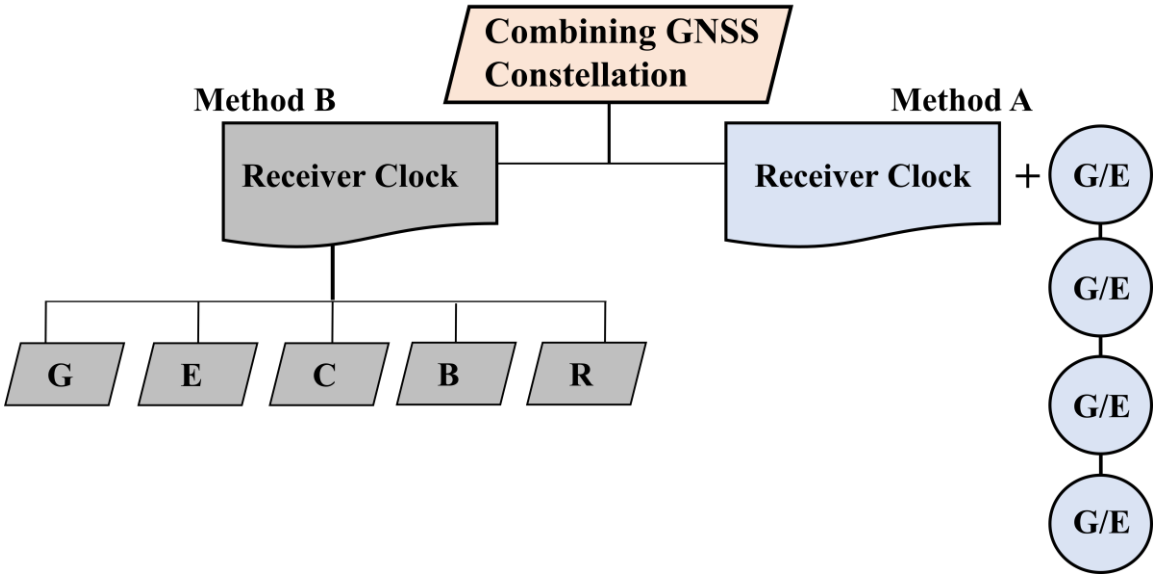

Figure 2.5: Treatment of ISB with respect to receiver clock estimation.

When processing GNSS data of different constellations, necessary strategies need to be followed for treating the receiver clock offset and ISB parameters. At present, three working stochastic models for handling ISB in multi-GNSS PPP data processing can generally be classified as random walk, white noise, and random constant (piece-wise constant). Random walk computes the last value in the estimation process with a linearly escalating variance (σ^2) in time. It is thus essential for scenarios that require minor variations in time. In the white noise model, the ISB parameters are conceived uncorrelated and independent in different epochs (Karaim et al., 2018). As such, the model is useful in situations where it is irrelevant to know parameter changes in advance (Liu et al., 2019). Lastly, the random constant is a particular case of a random walk stochastic model. What differentiates random walk and random constant models is that the latter has a zero value of process noise ($\sigma_{\omega_{ISB}}$) as expressed below:

$$\begin{cases} ISB^{S}_{i,rw}(e) = ISB^{S}_{i,rw}(e-1) + \omega_{ISB}, \qquad \omega_{ISB} \sim N\left(0, \sigma^2_{\omega_{ISB}}\right) \\ ISB^{S}_{i,wn}(e) \sim N(0, \sigma^2) \\ ISB^{S}_{i,rc}(e) \sim N(e-1) \end{cases} \tag{2.6}$$

where e denotes the current epoch, and $(e-1)$ denotes the previous epoch; the subscripts rw, wn, and rc denote random walk, white noise, and random constant, respectively.

For different GNSS, the receiver introduces code and phase ISB equivalent to differences between system clock offsets. In GNSS data processing, different authors model the ISB differently using any of the three modelling schemes. For example, Lou et al. (2016) introduced independent receiver clocks per each GNSS and then estimated clock offsets as white noise. The study further estimated receiver UCD as a random walk. Cai and Gao (2013) treated the ISB as piece-wise linear parameters, whereas Chen et al. (2015) neglected ISB in GNSS data processing.

For BDS signals, ISB have been demonstrated for signals broadcasted by GEO satellites in relation to those of IGSO and MEO satellites in Nadarajah et al. (2015). In order to enhance interoperability between BDS-2 and BDS-3, it is also crucial that intra-system biases be estimated. However, it is necessary to note that the treatment of ISB in PPP is different from that of differential positioning. Various aspects of ISB in both PPP and RTK have been intensively researched (Montenbruck et al., 2011; Tegedor et al., 2014; Torre and Caporali, 2015; Mi et al., 2020). Figure 2.6 provides an overview of ISB in GNSS data processing.

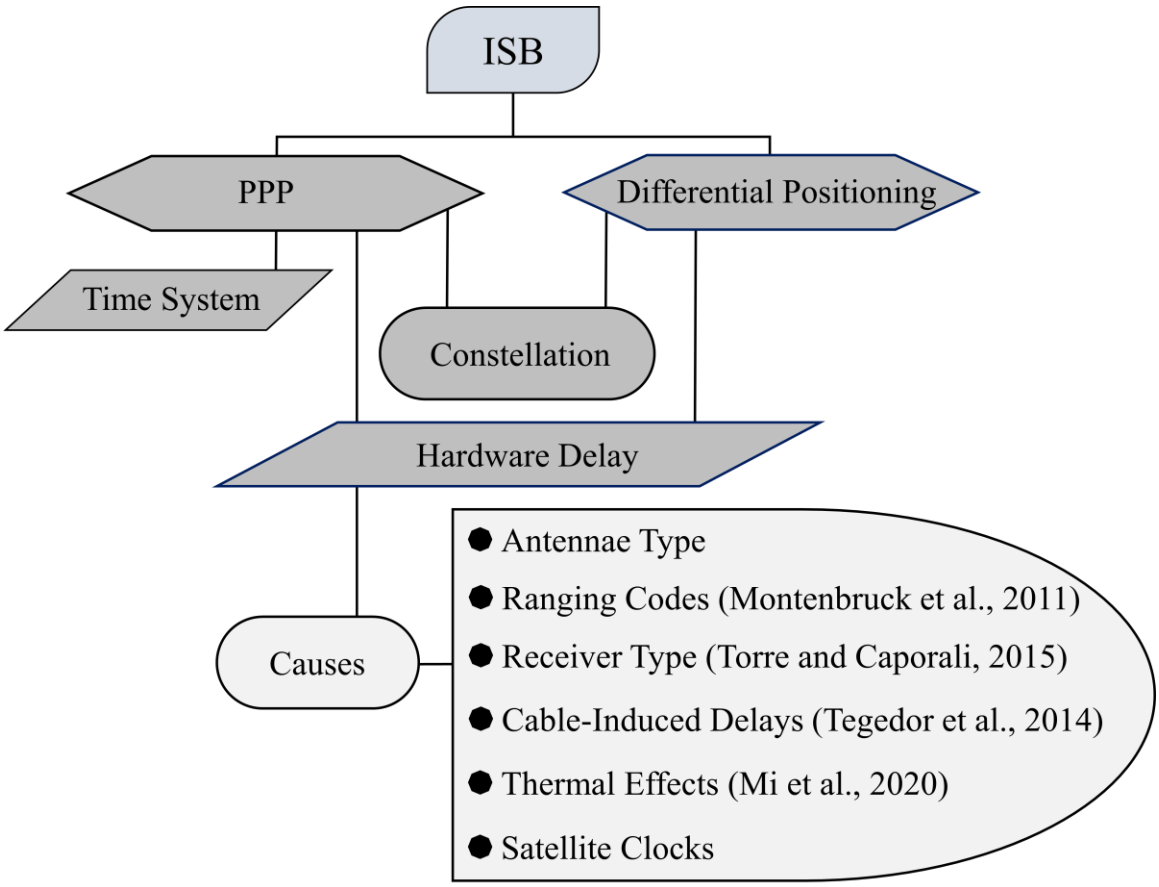

Figure 2.6: Overview of ISB in GNSS.

2.7 Chapter Summary

Different approaches for treating hardware biases have been extensively reviewed. Generally, it is shown that the current methods for treating IFCB are usually based on triple-frequency observations. With the GNSS modernisation and the full deployment of the BDS-3 constellation, the biases need further research. Since BDS-2 and BDS-3 constellations are two different satellite systems, then the combination of observations from these is also necessary. Therefore, in the course of treating the biases such as IFCB, the ISBs are also investigated including the parameterisation of unmodelled hardware biases in the receiver and satellite using weighting approaches suitable for handling satellites in three distinct orbits. In addition, the satellite orientation is considered in the modelling of GNSS observation errors and biases. Therefore, the specific

techniques implemented in this thesis and their numerical verifications are presented in Chapter 3, Chapter 4, and Chapter 5.

Chapter 3: Intersystem Biases in BDS Constellations

3.1 Introduction

The treatment of ISB is an important step in integrated GNSS pseudorange and carrier phase processing. In the context of this study, the ISB between BDS-2 and BDS-3 constellations is explored using the PPP functional model. The mathematical model that accounts for the ISB in combined GNSS data processing is developed, taking into consideration the characteristics of precise satellite orbit and clock products. To support this, a validation method is proposed which is currently not clarified in the existing literature.

3.2 ISB in BDS-2 and BDS-3 Integrated Data Processing

The ISBs are one of the biases that negatively affect the BDS-2 and BDS-3 fused PPP solution. ISB exist between signals of different GNSS constellations even for interoperable and compatible signals. Signal interoperability and compatibility is crucial in promoting multiple GNSS data processing. To enhance PNT services within Asia and worldwide, the BDS-2 and BDS-3 integrated positioning become a standard positioning to boot the overall number of visible satellites. These two generations of satellites are equipped with unique hardware broadcasting multiple frequencies to the user. The user also employs different types of receivers which may not track similar codes of frequencies. Worse still, for each specific receiver, a time delay bias is apparently obvious between BDS-2 and BDS-3 integrated processing.

The integration of BDS-2 and BDS-3 constellations in PPP improves the positioning performance, availability, and reliability. To promote combined BDS-2 and BDS-3 PNT services, this study investigates the possible influence of the bias between the two satellite systems on positioning performance. ISB is usually considered in multi-GNSS processing comprising satellites of different navigation systems. Since BDS-2 and

BDS-3 satellite systems belong to the same GNSS, then this type of bias is termed, intra-system bias, in this thesis.

In either single or combined PPP, the positioning performance and reliability of both float and fixed PPP solutions are mainly based on the quality of the multi-GNSS precise clock and orbit products. The availability and reliability of GNSS signals depend on the visibility of satellites with accurate orbits. Poor orbit quality can lead to signal outages or reduced satellite visibility. A better user position is achieved using the most accurate satellite orbits, clocks, and bias products. For example, the quality of the orbits and clocks is a function of the constellation, type of satellite and generation, orbital plane, satellite orientation, and the elevation of the Sun above the orbital plane. Thus, it is worthwhile to mention that the attitude quaternions and signal bias products also affect the PPP positioning performance, especially in ambiguity resolution. For this reason, the quaternions and signal biases may not be mandatory in GNSS data processing. Further details can be found in Loyer et al. (2021). Currently, the IGS and other institutions release multi-GNSS products required for PPP. The models about these MGEX products proposed in this thesis are presented in Chapters 4 and 5.

The precise orbits and clocks are mandatory in PPP and for this reason, MGEX products from different analysis centres (ACs) are accounted for in the evaluation of ISB in this study. Note that the key aspect enabling the best PPP performance lies in the quality of the MGEX products. Some research works on the precision and accuracy of multi-GNSS clock and orbit products have already been conducted. For example, Kazmierski et al. (2018) assessed the quality of multi-constellation clock and orbit products, and tested their precision using PPP experiments. In a similar study, Choy et al. (2017) and Kazmierski et al. (2020) evaluated the quality and availability of orbit and clock products from different ACs. The latter work uncovered the factors that affect GNSS orbit and clock corrections including satellite block, satellite type, onboard clocks, orbital characteristics, and the elevation of the sun above the orbital plane.

Despite the evaluation of the MGEX products, the analyses do not cover all MGEX products supporting the two constellations of BDS-2 and BDS-3. Further to this, the existing literature has not addressed the impact of various BDS precise orbit and clock products on ISB. Therefore, the quality of the MGEX products is thoroughly evaluated, followed by a comprehensive investigation of the ISB on the PPP accuracy using the combined processing of BDS-2 and BDS-3 observations. Hence, following the deployment of the modernised BDS-3 constellation, BDS-2 satellites are now being used to argument the BDS-3 constellation in rendering PNT services. This thesis takes advantage of both BDS-2 and BDS-3 constellations to study the ISB. Section 3.3 derives the PPP functional model for the estimation of ISB. After deducing the mathematical model, the next section presents the experimental description that also includes the dataset selection and processing criteria.

3.3 PPP Functional Model

The fundamental observable governing BDS code and phase observations can be expressed as in Leick et al. (2015)

$$\begin{cases} \Phi_{fi}^{k} = \rho_{i}^{k} + c \cdot \left(\Delta t_i + \delta_{fi,\Phi} + \Delta\delta_{fi,\Phi}\right) - c \cdot \left(\Delta t^{k} + \delta_{f,\Phi}^{k} + \Delta\delta_{f,\Phi}^{k}\right) + T_{i}^{k} \\ \qquad -\mu_{f} \cdot I_{i,f_1}^{k} + \lambda_{f} N_{fi}^{k} + \epsilon_{fi}^{k} \\ P_{fi}^{k} = \rho_{i}^{k} + c \cdot \left(\Delta t_i + \delta_{fi,P} + \Delta\delta_{fi,P}\right) - c \cdot \left(\Delta t^{k} + \delta_{f,P}^{k} + \Delta\delta_{f,P}^{k}\right) + T_{i}^{k} \\ \qquad +\mu_{f} \cdot I_{i,f_1}^{k} + \varepsilon_{fi}^{k} \end{cases} \tag{3.1}$$

with

$$\begin{cases} \mu_{j} = \dfrac{f_1^2}{f_j^2} \\ \lambda_{f} = \dfrac{c}{f_1 - f_2} \end{cases}$$

where Φ_{fi}^{k} denotes the phase observations between receiver i^{th} and k^{th} satellite for BDS frequency signals, as shown in Table 1.2, whereasP_{fi}^{k} denotes the corresponding

code observations BDS frequencies; ρ_i^k denotes the geometric distance between the receiver and satellite; c denotes the speed of light in vacuum; Δt_i and Δt^k denote the receiver and satellite clock offset, respectively; f denotes BDS carrier frequencies (refer to Table 1.2); $\delta_{fi,\Phi}$ denotes the time-invariant component of the receiver hardware biases for carrier-phase; $\delta_{f,\Phi}^k$ denotes the satellite time-invariant hardware biases for carrier-phase; likewise, $\delta_{fi,P}$ and $\zeta_{f,P}^k$ denote the pseudorange time-invariant parts of hardware delays for the receiver and satellite, respectively; on the other hand, $\Delta\delta_{fi,\Phi}$ and $\Delta\delta_{f,\Phi}^k$ denote the carrier-phase time-variant components of the hardware delays for the receiver and satellite, respectively; $\Delta\delta_{fi,P}$ and $\Delta\delta_{f,P}^k$ denote the pseudorange time-variant components of the hardware delays for the receiver and satellite, respectively; T_i^k denotes the line-of-sight (LOS) tropospheric delay; and I_{i,f_1}^k denotes LOS ionospheric delay; μ_j denotes the frequency-dependent IF amplification factor. ; λ_f denotes the carrier wavelength. Thus, λ_f denotes the wavelength of frequency $f_1 - f_2$; N_{fi}^k denotes the carrier phase integer ambiguity on frequency; the ϵ_{fi}^k and ε_{fi}^k denote the corresponding random measurement noise in phase and code observations, respectively. It should be noted that the antenna phase center variation (PCV) and phase center offsets (PCO) are applied to all phase and code observables in advance to remove the effect of frequency on ρ_i^k. Not listed in Equation (3.1) are the physical influences on BDS observations, including the relativistic and earth rotation effects, earth tide, and ocean loading tide effects.

The impact of the atmosphere on GNSS signals is divided into two parts, namely, the ionosphere and the troposphere. For phase and code observables, the effect of the troposphere is similar, with the phase advancing as it propagates through the ionosphere, while the code is delayed. Equation (3.1) includes the errors of the ionosphere for both phase and code observables. The ionosphere introduces the frequency-dependent delay to radio signals passing through it. This delay is proportional to $\frac{1}{f^2}$, where f represents frequency. In other words, the higher frequency signals experience less delay than lower frequency signals. Examples of BDS signals are presented in Table 1.2. The ratio $\frac{f_1^2}{f_j^2}$ is utilised as a scale factor in the ionospheric delay models to account for the frequency dependence of the ionospheric effects. It helps to normalise the delay with

respect to the frequency. The mathematical relationship describing the code and phase observations through the ionosphere can be expressed as:

$$\begin{cases} I_{j,\Phi} \equiv \dfrac{c}{f} I_{f,\Phi} = \lambda_f I_{f,\Phi} \\ I_{j,P} \equiv \dfrac{f_1^2}{f_j^2} I_{1,P} = \mu_j I_{j,P} \\ I_{f,P} = -I_{f,\Phi} \end{cases} \tag{3.2}$$

In Equation (3.2), the Φ represents denotes the phase scaled in the units of meters. From this equation, the ionospheric effect on the code and scaled phase have the same magnitude but opposite signs.

Equation (3.1) becomes IF when the effect of the first-order ionospheric delay is eliminated. This is achieved by differencing the product of the dual-frequency observations and their squares. Certain conditions must be met for this approach to be effective. For example, the geometric range should be kept constant by dividing the aforementioned products by the difference between the two squares of the frequencies. Thus, the IF combinations for phase and code can be formulated as

$$\begin{cases} \Phi_{i,IF}^k = \alpha \Phi_{f1}^k - \beta \Phi_{f2}^k \\ P_{i,IF}^k = \alpha P_{f1}^k - \beta P_{f2}^k \end{cases} \tag{3.3}$$

with

$$\begin{cases} \alpha = \dfrac{f_1^2}{f_1^2 - f_2^2} \\ \beta = \dfrac{f_2^2}{f_1^2 - f_2^2} \\ \beta_* = \alpha_* - 1 \end{cases}$$

α and β denote IF frequency combination factors; the symbol (*) denotes that the scalar can also be applied for other BDS frequency combinations.

3.4 PPP Model to Estimate the ISB

Before the ISB formulation, it is important to treat the LOS errors which delay or advance the GNSS signal. The ionospheric delay can be eliminated by formulating the ionosphere-free linear combinations using the code and phase observables. On the other hand, the tropospheric delay is modelled using *a priori* models and the resulting formula can be written as

$$\begin{cases} \Phi_{fi}^{k} = \rho_{i}^{k} + c \cdot \left(\Delta t_i + \delta_{fi,\Phi} + \Delta\delta_{fi,\Phi}\right) - c \cdot \left(\Delta t^{k} + \delta_{f,\Phi}^{k} + \Delta\delta_{f,\Phi}^{k}\right) + \\ \qquad MF \cdot ZWD_{i}^{k} + \lambda_f N_{fi}^{k} + \epsilon_{fi}^{k} \\ P_{fi}^{k} = \rho_{i}^{k} + c \cdot \left(\Delta t_i + \delta_{fi,P} + \Delta\delta_{fi,P}\right) - c \cdot \left(\Delta t^{k} + \delta_{f,P}^{k} + \Delta\delta_{f,P}^{k}\right) + \\ \qquad MF \cdot ZWD_{i}^{k} + \varepsilon_{fi}^{k} \end{cases} \tag{3.4}$$

where MF denotes the elevation-dependent wet mapping function, and ZWD_i^k denotes the zenith wet delay (ZWD).

In the combined BDS-2 and BDS-3 PPP, the IGS clock offsets and satellite ephemeris are used (Kouba, 2009; Montenbruck et al., 2017). In the precise clock estimation procedure, the receiver clock offset, satellite clock offset, ZWD, and ambiguity are taken as unknown estimables. Except for the ZWD, the other three terms are linearly dependent. As a result, the satellite and receiver hardware biases are lumped with the estimated parameters (Odijk et al., 2016). For instance, the receiver code hardware biases combine with the receiver clock offset, whereas the carrier-phase hardware biases combine with the ambiguity parameter. If not assimilated by the estimated parameters, the hardware delays appear in the residuals (Geng et al., 2010).

Considering that the BDS-2 constellation provides PNT services to The People's Republic of China and other Asia-Pacific regions whereas the BDS-3 constellation renders global services, the clock offset for the latter is selected as a reference, and an ISB is introduced in the former observation equation. Therefore, in order to investigate the influence of the bias between BDS-2 and BDS-3 on positioning performance, it is proposed in this thesis to reparameterise Equation (3.4) in terms of the BDS navigation systems and ISB as

$$\begin{cases} \Phi_{IF,i}^{B,k} = \rho_i^{B,k} + c\cdot\left(\Delta\hat{t}_i^{B,k} - \Delta\hat{t}_i^{B,k}\right) + MF\cdot ZWD_i^{B,k} + \lambda_f\cdot\widehat{N}_{IF,i}^{B,k} + \epsilon_{fi}^{B,k} \\ \Phi_{IF,i}^{C,k} = \rho_i^{C,k} + c\cdot\left(\Delta\hat{t}_i^{B,k} - \Delta\hat{t}_i^{C,k}\right) + \Delta\xi_i + MF\cdot ZWD_i^{C,k} + \lambda_f\cdot\widehat{N}_{IF,i}^{C,k} + \epsilon_{fi}^{C,k} \\ \mathrm{P}_{IF,i}^{B,k} = \rho_i^{B,k} + c\cdot\left(\Delta\hat{t}_i^{B,k} - \Delta\hat{t}_i^{B,k}\right) + MF\cdot ZWD_i^{B,k} + \varepsilon_{fi}^{B,k} \\ \mathrm{P}_{IF,i}^{C,k} = \rho_i^{C,k} + c\cdot\left(\Delta\hat{t}_i^{B,k} - \Delta\hat{t}_i^{C,k}\right) + \Delta\xi_i + MF\cdot ZWD_i^{C,k} + \varepsilon_{fi}^{C,k} \end{cases} \quad (3.5)$$

with

$$\left.\begin{aligned} \Delta\hat{t}_i^{B} &= c\cdot\Delta t_i + \delta_{IF,i}^{B} + \Delta\delta_{IF,i}^{B} \\ \Delta\hat{t}_i^{B,k} &= c\cdot\Delta t^{B,k} + \delta_{IF}^{B,k} + \Delta\delta_{IF}^{B,k} \\ \Delta\hat{t}_i^{C,k} &= c\cdot\Delta t^{C,k} + \delta_{IF}^{C,k} + \Delta\delta_{IF}^{C,k} \\ \Delta\xi_i &= \alpha_{1,2}\left(\delta_{i,1}^{C} - \delta_{i,1}^{B}\right) + \beta_{1,2}\left(\delta_{i,2}^{C} - \delta_{i,2}^{B}\right) \\ \widehat{N}_{IF,i}^{B,k} &= \frac{1}{\lambda_{IF}}\left[N_{IF,i}^{B,k} + \left(\delta_{fi,\Phi} + \Delta\delta_{fi,\Phi}\right) - \left(\delta_{f,\Phi}^{B,k} + \Delta\delta_{f,\Phi}^{B,k}\right)\right] - \left(\delta_{fi,P} + \Delta\delta_{fi,P}\right) \\ &\quad -\left(\delta_{f,P}^{B,k} + \Delta\delta_{f,P}^{B,k}\right) \\ \widehat{N}_{IF,i}^{C,k} &= \frac{1}{\lambda_{IF}}\left[N_{IF,i}^{C,k} + \left(\delta_{fi,\Phi} + \Delta\delta_{fi,\Phi}\right) - \left(\delta_{f,\Phi}^{C,k} + \Delta\delta_{f,\Phi}^{C,k}\right)\right] - \left(\delta_{fi,P} + \Delta\delta_{fi,P}\right) \\ &\quad -\left(\delta_{f,P}^{C,k} + \Delta\delta_{f,P}^{C,k}\right) \end{aligned}\right\}$$

where the superscripts C and B denote the Chinese Compass (BDS-2) and BDS-3 navigation systems, respectively; $\Delta\hat{t}_i$ and $\Delta\hat{t}^{*,*}$ denote the receiver and satellite clocks that have lumped with hardware biases, respectively (of which the first and second star ''*'' denotes the constellation and PRN, respectively), the λ_{IF} denotes the ionosphere-free (IF) wavelength corresponding to a particular BDS frequency, $\Delta\xi_i$ denotes the ISB parameter; and $\widehat{N}_{IF,i}^{*,k}$ denotes the float ambiguity term for BDS-2 ($\widehat{N}_{IF,i}^{B,k}$) and BDS-3 ($\widehat{N}_{IF,i}^{C,k}$) constellations. The satellite and receiver clock terms in Equation (3.1) cannot be

separated from each other due to rank deficiency (Bock et al., 2009). To resolve the rank deficiency, a clock constraint should be applied by introducing a reference datum bias for each constellation (Steigenberger and Montenbruck, 2020).

Currently, IGS through distinct ACs generates MGEX precise clock products that support different GNSS systems including BDS-2 and BDS-3 constellations. Different constellations in the MGEX precise products are defined with the same clock datum, which when applied can be compensated by the receiver clock at the user end. To evaluate the influence of the MGEX precise products on the ISB, the datum constraint is set for BDS-2 and BDS-3 in this work. Therefore, after applying the MGEX precise products, $\Delta\check{\xi}_i$ in Equation (3.5) can be re-written as

$$\Delta\check{\xi}_i = \alpha_{1,2}\left(\delta_{i,1}^{C} - \delta_{i,1}^{B}\right) + \beta_{1,2}\left(\delta_{i,2}^{C} - \delta_{i,2}^{B}\right) + \Delta D_{\tau}^{C,B} \tag{3.6}$$

with

$$\Delta D_{\tau}^{C,B} = D_{\tau}^{C} - D_{\tau}^{B}$$

where $\Delta\check{\xi}_i$ denotes the resulting ISB after applying a particular MGEX precise product; D_τ denote the clock reference datum and the MGEX precise product, such that $\Delta D_{\tau}^{C,B}$ is the difference between the BDS-2 (D_{τ}^{C}) and BDS-3 (D_{τ}^{B}) clock datums in the precise products.

3.5 Experimental Validation

To assess the proposed model, experimental validation was undertaken. The following subsections describe the dataset selection and software implementation.

3.5.1 BDS Datasets

The validation takes advantage of the redundant number of BDS-2 and BDS-3 satellites. This is due to an increased number of MGEX stations with BDS tracking capability. For example, Figure 3.1 illustrates the visible number of BDS satellites on DOY 018, 2021, where it can be seen that at least 16 BDS satellites can be observed globally. Note that the number of satellites was plotted at an elevation angle of $\geqslant 5°$, and the variation in colour indicates the satellite visibility. Thus, for this experiment, observations in January 2021 (DOY 001 to 031) from thirty-one (31) worldwide MGEX stations equipped with different types of receivers were used. The geographical distribution of the selected stations is illustrated in Figure 3.2 in which the colour codes denote the different receiver types. These receivers were selected randomly as long as they had both BDS-2 and BDS-3 observations during the study period.

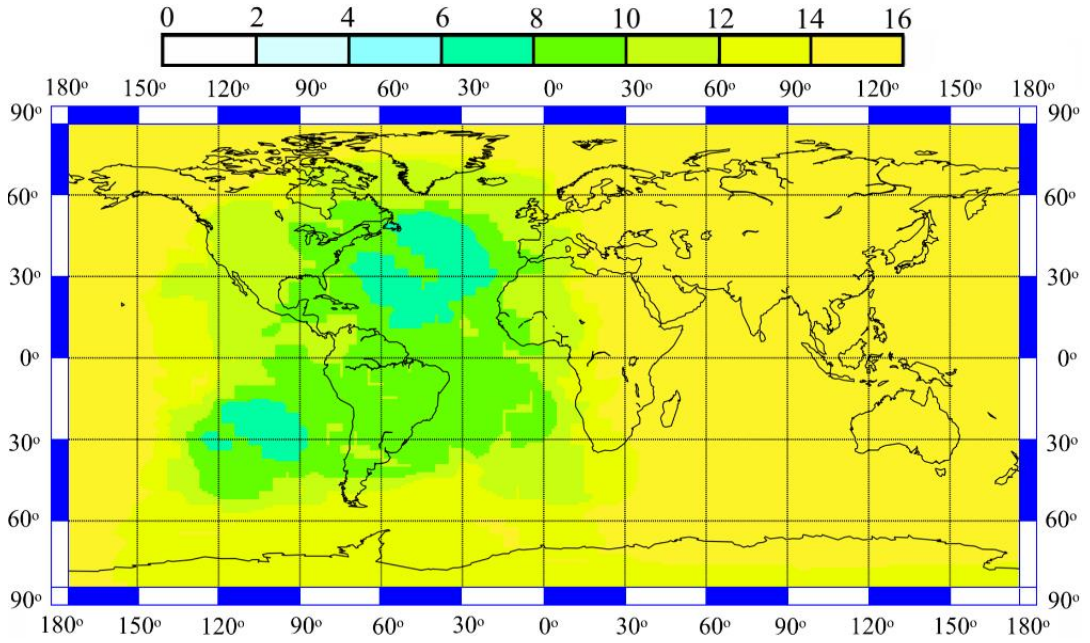

Figure 3.1: BDS-2 and BDS-3 visible number of satellites on DOY 018, 2021.

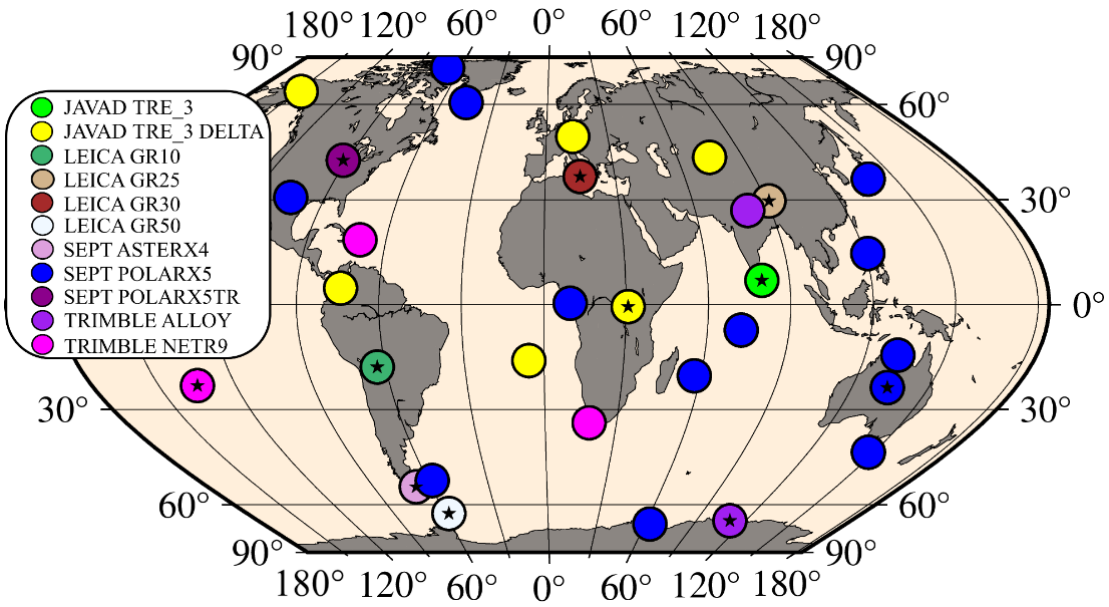

Figure 3.2: Distribution of the BDS tracking stations.

All 31 stations were used to investigate the effects of the ISB on the combined BDS-2/BDS-3 PPP using different multi-GNSS orbit and clock products. Table 3.1

summarises the receiver types for the selected stations. To ensure that all receivers are considered in the evaluation, one receiver was selected for each type (11 receivers in total) and are marked with stars in Figure 3.2.

Table 3.1: Summary of receiver and antenna types.

Manufacture	Receiver Type	Station	Number
JAVAD	JAVAD TRE_3	SGOC	1
	JAVAD TRE_3 DELTA	BOGT, GCGO, MBAR, POL2, STHL, WTZZ	6
LEICA	LEICA GR10	SCRZ	1
	LEICA GR25	LHAZ	1
	LEICA GR30	NOT1	1
	LEICA GR50	OHI3	1
SEPTENTRIO	SEPT ASTERX4	RIO2	1
	SEPT POLARX5TR	NLIB	1
	SEPT POLARX5	ALIC, DGAR, FALK, HOB2, KAT1, MAW1, MDO1, NKLG, PTGG, QAQ1, THU2, USUD, VACS	13
TRIMBLE	TRIMBLE ALLOY	CAS1, LCK4	2
	TRIMBLE NETR9	GAMB, JCTW, RDSD	3
		Total :	31

To undertake BDS-2 and BDS-3 combined processing, MGEX products supporting both constellations are necessary. As of January 2021, there are eight (8) main ACs that generate orbit and clock products at different intervals (Table 3.2). As can be seen in Table 3.2, four ACs generate products covering the full range of GNSS including GPS (G), GLONASS (R), Galileo (E), BDS (C), and Quasi-Zenith Satellite System (QZSS, J). To generate such products, the availability of BDS-2/BDS-3 observations is vital. In this case, ground stations with the tracking capability of both navigation systems are indispensable. For example, the Center for Orbit Determination in Europe (CODE) and Technische Universität München (TUM, given in German, and in English it means Technical University of Munich) are limited to generating BDS-2 precise products, due to the reduced number of BDS-3 tracking stations. On the contrary, the Deutsches GeoForschungsZentrum (GFZ, in German, meaning German Research Centre for Geosciences), Wuhan University (WU), Information and Analysis Center (IAC),

Centre National d'Etudes Spatiales (CNES, given in French meaning the National Centre for Space Studies)/Collecte Localisation Satellites (CLS), and Shanghai Observatory (SHAO) are the only ACs providing precise products for both BDS-2 and BDS-3 satellites. As summarised in Table 3.2, the short and long file names are interchangeably used to identify the precise products. For instance, the precise products generated by SHAO are either called SHA or SHA0MGXRAP. It is worth mentioning that the long-file names have been in use since GPS week 2038 (NASA, 2021). In each long-file name, the last three characters represent the solution type. For example, FIN and RAP denote the final and rapid MGEX products, respectively.

Table 3.2: Summary of MGEX precise products as of January 2021.

Provider	Identity	Interval [sec]		Constellation	Supported BDS Constellation
		Clock	Orbit		
CODE	COM, COD0MGXFIN	30	900	GRECJ	BDS-2
GFZ	GBM, GFZ0MGXRAP	30	900	GRECJ	BDS-2 + BDS-3
WU	WUM, WUM0MGXFIN	300	900	GRECJ	BDS-2 + BDS-3
IAC	IAC, IAC0MGXFIN	300	300	GRECJ	BDS-2 + BDS-3
CNES/CLS	CNT	5	300	GREC	BDS-2 + BDS-3
	GRM, GRG0MGXFIN	30	900	GRE	-
SHAO	SHA, SHA0MGXRAP	300	300	GREC	BDS-2 + BDS-3
JAXA	QZF, JAX0MGXFIN	30	300	GRJ	-
TUM	TUM, TUM0MGXRAP	300	300	GCJ	BDS-2

All the products shown in Table 3.2 can be found on the IGS website (NASA, 2021b) except the CNT precise products which can be found at the PPP Wizard project site (CNES, 2020). The CNES/CLS generates CNT and GRM precise products which support GREC and GRE constellations, respectively. As for CNT, the PPP Wizard project site releases real-time and post-processed products necessary for different scientific applications including PPP software testing. The CNT products support BDS-2 and BDS-3 constellations just like the GBM, WUM, IAC, and SHA products. For such a reason, these five products were used to validate the ISB model in this study. Before PPP validation, the quality of these products was evaluated because the ISB may

be unstable over time due to varying precise clock computation approaches applied in different ACs.

3.5.2 Quality Evaluation of BDS-2 and BDS-3 Orbits and Clocks

The BDS-2 and BDS-3 orbit evaluation was performed using BKG Ntrip Client (BNC) software (Weber and Mervart, 2007). BNC is an open-source GNSS software primarily designed for real-time applications. In addition to this usage, the package is also equipped with post-processing functionality including PPP, GNSS data manipulation, and quality assessment. In the context of this research, BNC was used because of its capability to evaluate GNSS precise products. In this software, the standard product 3 (SP3) comparison module was used to convert the coordinate differences between a pair of SP3 into radial, along-track, and cross-track components. To compute the orbits and clocks, a reference product for SP3 comparison is mandatory. For example, Deng et al. (2016) and Montenbruck et al. (2018) used GBM products as a precise reference to investigate the combined effect of multi-GNSS products. The computation was based on GBM products owing to an increased number of observations from both BDS-2 and BDS-3 constellations. The justification for this choice is, that BNC software requires that a particular satellite be available from one of the precise products. Hence, if there are no BDS observations in the other products, they may be found in the GMB products to initiate SP3 comparison.

3.5.2.1 BDS-2 and BDS-3 Orbit Experimental Results

By using the BDS-2 and BDS-3 constellations, the four MGEX products were evaluated in radial, along-track, and cross-track components using observations for the month of January in 2021. Figure 3.3 and Figure 3.4 depict the one-month Root Mean Square Error (RMSE) values for the WUM, CNT, SHA, and IAC estimated with respect to GBM products as:

$$RMSE = \sqrt{\frac{1}{n}\sum_{p=1}^{n}\Delta_p^2} \tag{3.7}$$

where Δ_p denotes the orbital difference, and n denotes the number of measurements. For C01 – C05, all the orbit RMSE values are larger. In particular, PRN C01 – C05 exhibit RMSE values above one metre apart from those derived from WUM products in the along-track. The orbit RMSE values are larger than the rest because of poor orbits. It is worth mentioning that the orbit products are prepared from observations made by ground stations of GNSS receivers. Regarding BDS, the orbit precision is relatively poor due to unfavourable observation geometry. The IGSO and GEO satellites have an orbital height of 35,786 km whereas the MEO satellites have an orbital height of 21, 528 km. Further details about the characteristics of BDS space constellation and altitude can be found in the Interface Control Document (ICD) (CNSO, 2017). Such orbital heights have an impact on the generated orbit products for GNSS data processing applications. For instance, the high altitude of GEO satellites and the limited number of stations that can track such satellites contribute to poor observation geometry.

As for C06 – C16 (Figure 3.4), the RMSE are all less than a meter in all three components. In the case of BDS-3 constellation, C19 – C37 (Figure 3.5) agree within 0.03 to 0.17 m using the selected MGEX products. This form of agreement can be attributed to the fact that majority of the MGEX stations can track these BDS-3 satellites. On the other hand, C38 – C60 (Figure 3.6) register larger RMSE values pegged within 0.50 to 0.84 m, and this poor performance is attributed to missing observations in the products for the calculation of the solutions.

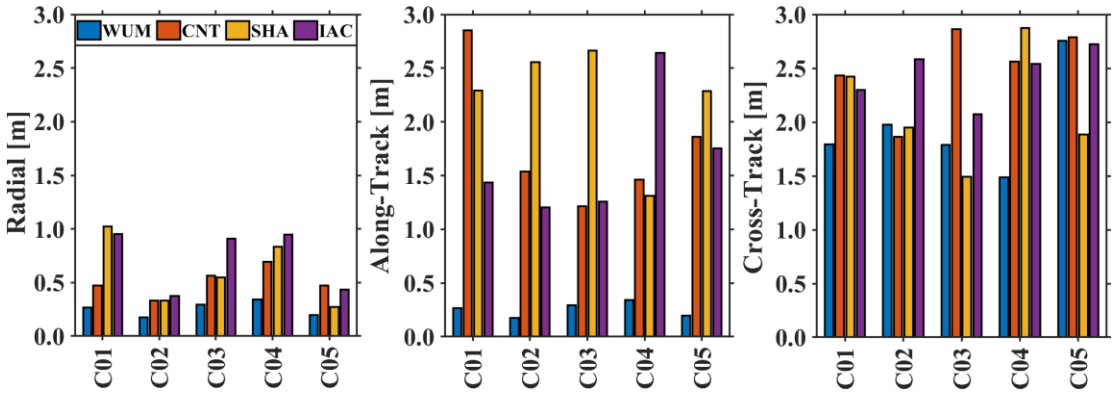

Figure 3.3: Orbit performance for C01-C05 satellites.

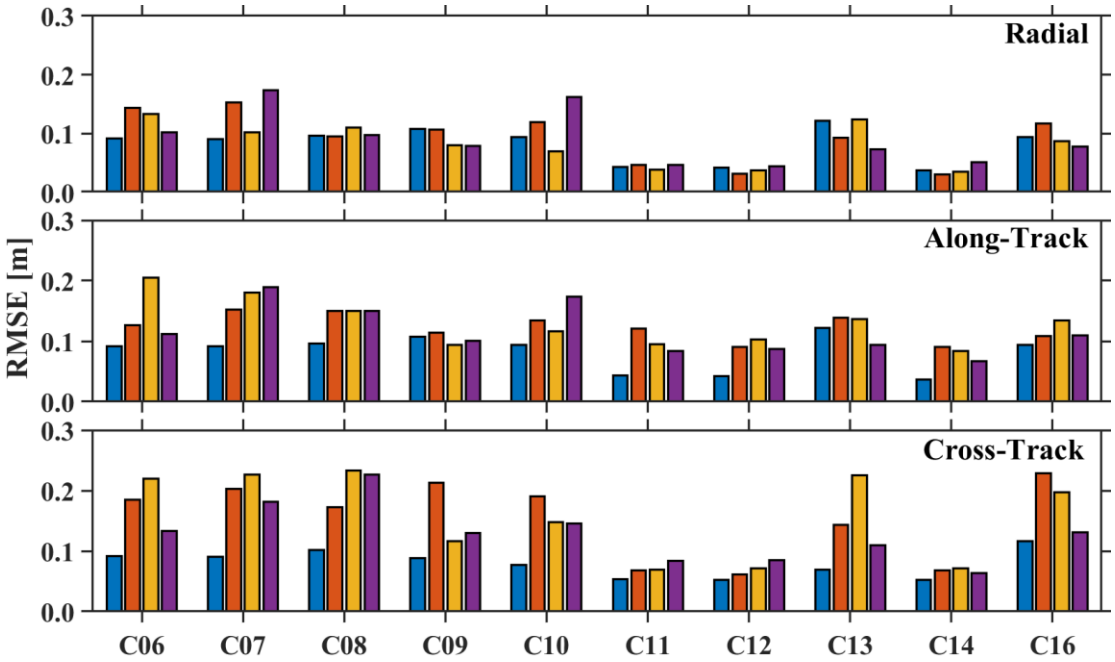

Figure 3.4: Orbit performance for C06-C16 satellites.

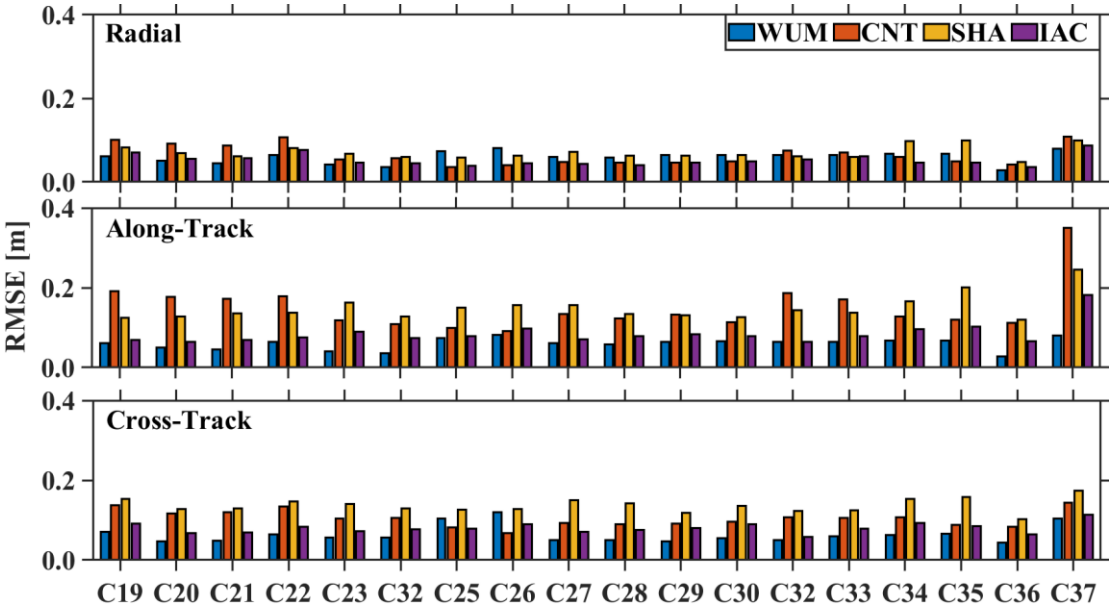

Figure 3.5: Orbit performance for C19-C37 satellites.

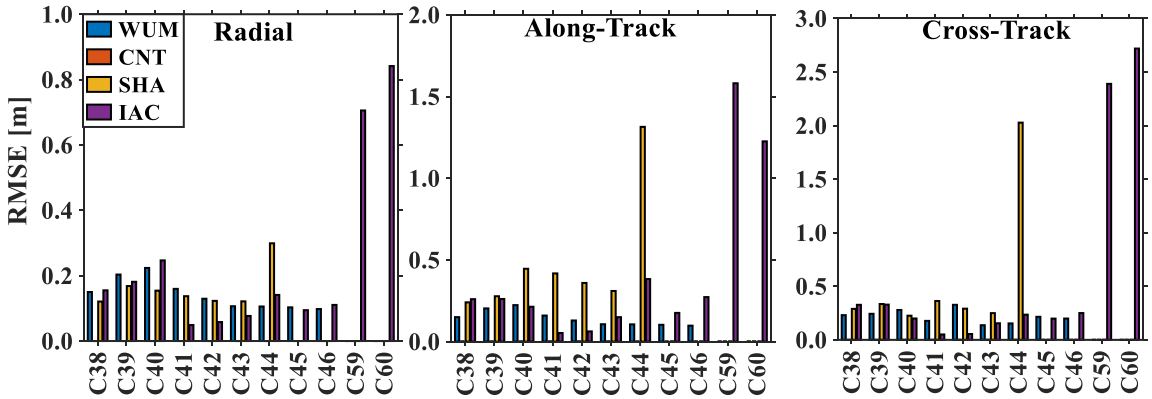

Figure 3.6: Orbit performance for C38-C60 satellites.

The numerical statistics for BDS-2 and BDS-3 are depicted in Table 3.3. In the case of BDS-2 satellites, the orbit differences for WUM outweigh the rest with 0.138 m, 0.139 m, and 0.706 m in the radial, along-track and cross-track components, respectively. For BDS-3 satellites, the CNT products register better performance in the radial and cross-track components with RMSE values of 0.065 m and 0.104 m, respectively, while WUM products show smaller RMSE values in the along-track component. In addition to evaluating orbital differences per satellite, the overall performance per MGEX products was also examined (Figure 3.8).

Table 3.3: BDS-2 and BDS-3 orbit and clock RMSE statistics (unit: m).

	BDS-2				BDS-3			
	WUM	CNT	SHA	IAC	WUM	CNT	SHA	IAC
Radial	0.138	0.232	0.255	0.302	0.086	0.065	0.096	0.124
Along-Track	0.139	0.677	0.828	0.631	0.087	0.15	0.242	0.212
Cross-Track	0.706	0.936	0.813	0.901	0.115	0.104	0.25	0.288
Clock	0.102	0.184	0.183	0.184	0.077	0.104	0.103	0.095

3.5.2.2 BDS-2 and BDS-3 Clocks Test Results

To thoroughly evaluate the quality of BDS-2 and BDS-3 clock products, the products were evaluated for each individual satellite and the evaluated clock solutions are illustrated in Figure 3.7. As can be evidenced in the upper panel, the RMSE values for C01 – C06 satellites are worse than those of C06 – C16 reaching up to 50 cm for SHA products. Moreover, the RMSE values for C06 – C16 range between 5 and 21 cm with C09 at the maximum. On the other hand, the BDS-3 clock RMSE values are less than 40 cm for all MGEX products. For instance, the RMSE values for C19 – C36 satellites are spread between 3 and 13 cm, while those of PRNs C37 – C60 are in the range of 5 – 36 cm. This clearly shows a better consistency in the former chunk of satellites (C19 – C36) than in the latter. This is attributed to more observations for those satellites due to more BDS-3 tracking stations that can observe such satellites. Conversely, the newly deployed satellites (C37 – C60) register poor clock performance due to a limited number of ground stations necessary for precise clock estimation.

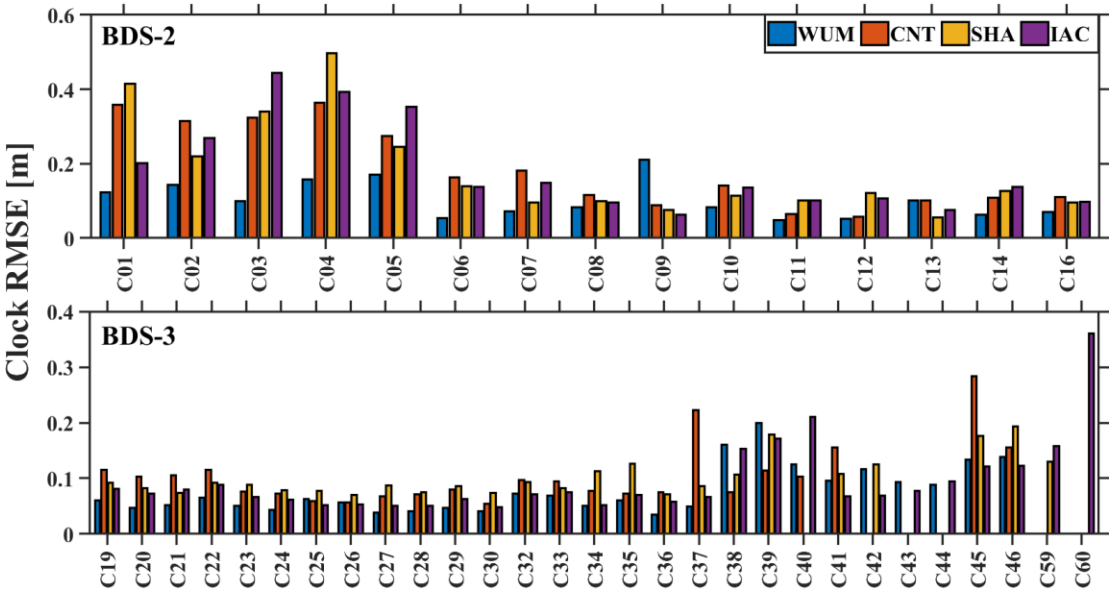

Figure 3.7: BDS-2 and BDS-3 clock RMSE with respect to GBM product.

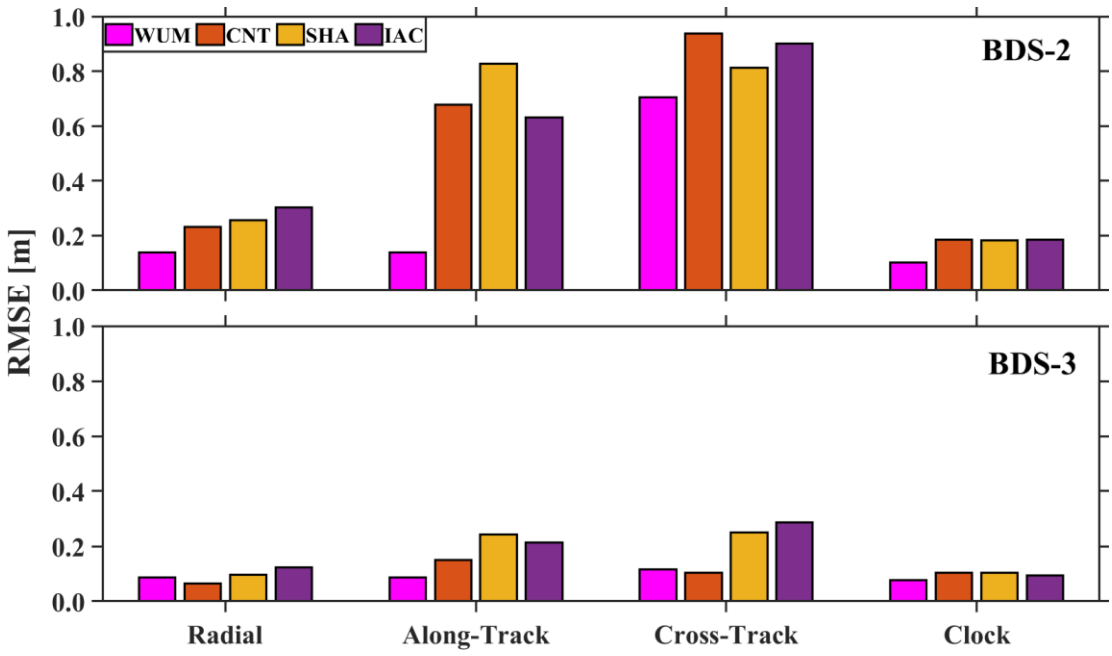

Figure 3.8: BDS orbit and clock RMSE with reference to GBM product.

Apart from evaluating clock performance per satellite, the clock solutions were also evaluated per MGEX precise product in order to assess the overall performance per

MGEX product. The clock differences for each MGEX product and their numerical statistics are presented in Figure 3.8 and Table 3.3, respectively. Using WUM products, the clock differences perform the best for both BDS-2 and BDS-3 satellites. Furthermore, the CNT, SHA, and IAC MGEX products exhibit similar clock differences for both BDS-2 as compared to those of BDS-3 satellites.

3.5.2.3 Combined Effect of BDS-2 and BDS-3 Orbits and Clocks

The assessment of orbit and clock products can be carried out through various methods, with a direct comparison of SP3 products to benchmark products being the most straightforward approach, as outlined in Sections 3.5.2.1 and 3.5.2.2. These comparisons yield statistics such as mean, RMSE, and standard deviations (STDs). While these metrics are valuable for evaluating precise products, they do not directly provide information on position accuracy.

To address this limitation, the Signal-In-Space Range Error (SISRE) is commonly employed. SISRE serves as a quality indicator for broadcast ephemeris. It quantifies errors in satellite ephemerides that impact user position computation, relying solely on the accuracy of the orbit and clock products used in the navigation solution. The SISRE is computed for each satellite, considering radial, along-track, cross-track, and clock errors, which involve the difference between the satellite position and the broadcasted clock solution. It is crucial to note that the antenna offset vectors used for calculating clock correction errors must align with those employed in the orbit and clock product being assessed.

Besides evaluating the BDS orbit and clock products separately, their combined effect was also investigated using SISRE. The calculated radial, along-track, and cross-track components generated in BNC software were used to compute the SISRE statistics based on the model proposed by Montenbruck et al. (2018), which can be presented as follows:

$$\begin{cases} \mathrm{SISRE}_{\mathrm{IGSO/GEO}} = \sqrt{(0.99R - \Delta cdt)^2 + \frac{1}{126}(A^2 + C^2)} \\ \mathrm{SISRE}_{\mathrm{MEO}} = \sqrt{(0.98R - \Delta cdt)^2 + \frac{1}{54}(A^2 + C^2)} \end{cases} \quad (3.5)$$

where R, A, and C denote the orbit residuals in the radial, along-track, and cross-track components, respectively, Δcdt denotes the clock difference, $\mathrm{SISRE}_{\mathrm{IGSO/GEO}}$ denotes the SISRE for IGSO and GEO satellites, $\mathrm{SISRE}_{\mathrm{MEO}}$ denotes the SISRE for MEO satellites, the four coefficients 0.99, 1/126, 0.98, and 1/54 are the weights expressed with respect to BDS orbit height. CSNO (2022) provides further details about these SISRE coefficients. Using Equation (3.5), the SISRE for IGSO/GEO and MEO satellites were computed for WUM, CNT, SHA, and IAC precise products using the one-month datasets in January 2021 (DOY 001 – 031, 2021). Figure 3.9 shows the average SISRE for WUM, SHA, CNT, and IAC products.

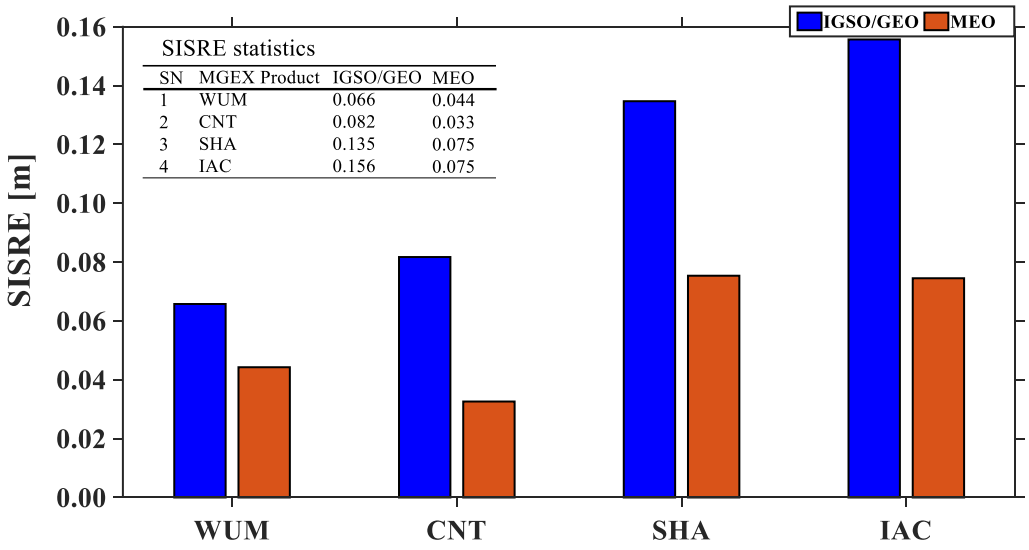

Figure 3.9: SISRE for BDS constellations from DOY 001-031 in 2021.

From Figure 3.9 and the superimposed statistics, it can be observed that IGSO/GEO satellites have the highest SISRE value reaching up to about 16 cm (for IAC). The blue

and red bins indicate the SISRE values for IGSO/GEO and MEO constellations, respectively. In contrast, the combined quality of IGSO/GEO satellites for WUM exhibits the smallest SISRE value at 7 cm. In the case of MEO satellites, the CNT product generally achieves the best SISRE value (about 3 cm). The IGSO/GEO combined reduced performance may be attributed to limited observations for PRNs C38, C39, C40, and C56 for IGSO satellites, and PRNs C59 – C61 for the GEO constellation.

3.5.3 PPP Experiments

The B1I and B3I signals were used to test the proposed method because they support both BDS-2 and BDS-3 constellations. The orbit and clock errors were corrected using the MGEX products from different ACs in order to assess their influence on the ISB. Besides the orbit and clock biases, multipath effects were also considered. Therefore, to account for noise and multipath errors at lower elevation angles, the elevation mask of 10° was employed.

Additionally, phase and code observations exhibit distinct characteristics regarding the impact of cycle slips. The carrier phase includes an unknown number of ambiguities that change each time the receiver locks onto the signal following a cycle slip. In contrast, the code measurement is unambiguous. While the code measurements are unambiguous, they tend to be noisy, exhibiting noise at the meter level. On the other hand, carrier measurements are more precise, with noise at a few millimetres, but they are ambiguous, as unknown biases can extend to thousands of kilometres. Given this difference in precision, the STDs for the phase and code were weighted as 3 mm and 300 mm, respectively, in the processing filter.

To validate the impact of different precise products and ISB on PPP, two processing schemes were established. The first processing method considers the ISB whereas the second one ignores the ISB in the model. Since BDS satellites fall into three different

types of orbits, a weighting strategy was employed to account for that. In this case, a weight of 4 was assigned to GEO satellites due to poor quality of their orbits and clock products (Pan et al., 2017). On the other hand, a weight of 1 was given to the IGSO and MEO satellites. The former and latter weighting schemes were assigned based on

$$\begin{cases} w = 1, & E > 30^{\circ} \\ w = 4 \cdot \mathrm{Sin}\,(E)^2, & E < 30^{\circ} \end{cases} \tag{3.6}$$

where w and E denote the weight and elevation angle, respectively. The MEO and IGSO satellites are affected by satellite-induced biases, and because of that such biases were also corrected according to Wanninger and Beer (2015). In the case of zenith hydrostatic delay (ZHD), the Global Pressure and Temperature (GPT, Boehm et al., 2007) and Saastamoinen model (Saastamoinen, 1972) were applied, whereas the ZWD was estimated as random walk noise using an empirical spectral density value of $10^{-8}\ \mathrm{m}^2 \cdot \mathrm{s}^{-1}$ (Li and Zhang, 2014), and mapped using the Global Mapping Function (GMF, Boehm et al., 2006). The PPP correction models described in this section are summarised in Table 3.4. The models applied in this section can be found in the given references and in most GNSS textbooks, and for that reason, they are not derived in this thesis.

In the case of positioning, performance was evaluated with respect to the station positions in the Solution Independent Exchange (SINEX). The benchmark station coordinates in the SINEX files are expressed in three components, namely, North, East, and Up. In this thesis, coordinates in the Earth-Centred Earth-Fixed (ECEF) reference system were estimated and the corresponding 3D coordinates were obtained using the following mathematical relation

$$\left.\begin{aligned} \mathrm{North} &= \Delta X(-\mathrm{Cos}\ \lambda \cdot \mathrm{Sin}\ \varphi) + \Delta Y(-\mathrm{Sin}\ \varphi \cdot \mathrm{Cos}\ \varphi) + \Delta Z(\mathrm{Cos}\ \lambda) \\ \mathrm{East} &= \Delta X(-\mathrm{Sin}\ \varphi) + \Delta Y(\mathrm{Cos}\ \lambda) \\ \mathrm{Up} &= \Delta X(\mathrm{Cos}\ \lambda \cdot \mathrm{Cos}\ \varphi) + \Delta Y(\mathrm{Sin}\ \varphi \cdot \mathrm{Cos}\ \varphi) + \Delta Z(\mathrm{Sin}\ \varphi) \end{aligned}\right\} \tag{3.7}$$

where ΔX, ΔY, and ΔZ denote the positioning biases in the ECEF reference system (Figure 3.10a), φ and λ denote the geodetic latitude and longitude of the MGEX station, respectively.

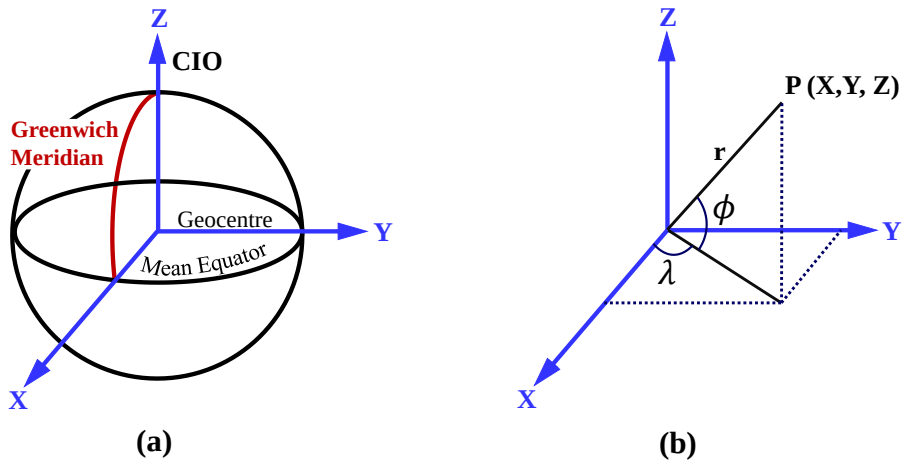

Figure 3.10: Geocentric earth-fixed coordinate systems.

Describing the location of the geodetic station on Earth's surface is conveniently achieved using the ECEF coordinate system (Figure 3.10a). This system employs a right-handed Cartesian framework (X, Y, Z) with its origin coinciding with the Earth's center of mass (CoM). The Z-axis aligns with the mean rotational axis of the Earth, and the X-axis points to the mean Greenwich meridian, forming a right-handed system. The Y-axis completes this orientation.

The Z-axis specifically points to the Conventional International Origin (CIO), which represents the mean pole of the Earth's rotation by international convention. The XY-plane is termed the mean equatorial plane, and the XZ-plane is referred to as the mean zero meridian. The ECEF coordinate system is also recognised as the Conventional Terrestrial System (CTS). The use of the mean rotational axis and mean zero meridian is essential because the true rotational axis of the Earth constantly changes direction in relation to the Earth's body.

Alternatively, the ECEF coordinate system can be expressed in a spherical coordinate system using r, φ, and λ (Figure 3.10b). Here, r denotes the radius of the point (X, Y, Z). The λ value is measured eastward from the zero meridian. The ECEF system provides the necessary information for satellite attitude modeling, as discussed in Chapter 5.

Table 3.4: PPP processing strategy.

Parameter	Strategy
Program	Least Squares
Tracking datasets	BDS globally distributed stations (Figure 3.2)
	IF phase and code measurements
Sampling	30 seconds
Constellation	BDS-2 and BDS-3 (IGSO, MEO, and GEO satellites)
Signal combination	B1I + B3I
MGEX products	GFZ0MGXRAP; WUM0MGXFIN; IACOMGXFIN;
	CNT; SHA0MGXRAP
Cut-off angle	10 °
Weighting	Phase =3 mm; Code = 300 mm;
ISB	W/ or w/o
PCO and PCV	Corrected with igs14.atx (Schmid *et al.*, 2005)
Sagnac effect	Corrected (Petit and Luzum, 2010)
Phase wind-up	Corrected (Wu *et al.*, 1992)
Relativistic effect	Applied with respect to the International
	Earth Rotation Service (IERS) convention 2010 (Kouba, no date)
Tidal displacement	Applied (Petit and Luzum, 2010)
ZWD	Saastamoinen model (Saastamoinen, 1973), estimated every hour using
	the GMF (Bohm *et al.*, 2006)
Ambiguity	Floating solution

3.5.3.1 PPP Test Results

The positioning experiments were undertaken to evaluate the influence of considering ISB parameters in the BDS-2 and BDS-3 integrated processing. To achieve this, PPP tests were run in static mode using two processing schemes: without ISB and with ISB. The PPP tests were conducted using five different MGEX precise products, and the positioning results are depicted in Figure 3.11 using boxplots. The lower and top edges depict the 25th and 75th percentile, respectively, while the central mark and the circle denote the median and mean, respectively. Thus, the left and right boxplots illustrate the results for the two processing criteria namely, without and with ISB, respectively. The numerical statistics are summarised in Table 3.5. When the ISB parameter is considered in the processing model, the results in both Figures 3.11 and Table 3.5 indicate that the positioning solution computed with GBM products improves the best by 61%, 42%, and 21% in the North, East, and Up components, respectively.

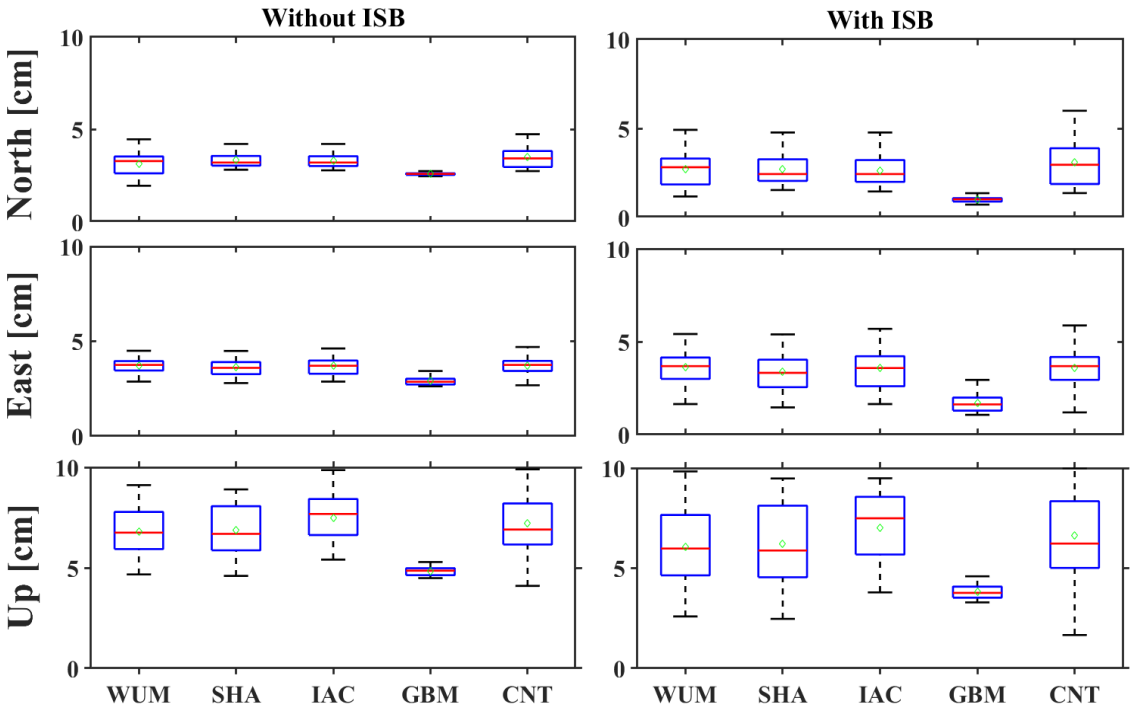

Figure 3.11: BDS combined positioning performance using different MGEX products.

Table 3.5: Positioning performance using different MGEX products (unit: cm).

	Without ISB					With ISB					Remarks
	WUM	SHA	IAC	GBM	CNT	WUM	SHA	IAC	GBM	CNT	
North	3.1	3.2	3.2	2.6	3.5	2.5	2.4	2.5	0.9	3.1	JAVAD
	3.5	3.6	3.6	2.6	3.5	3.1	3.4	3.4	1.1	3.1	LEICA
	3.1	3.4	3.3	2.6	3.4	2.8	2.7	2.5	1.1	3.1	SEPT
	2.8	3.3	3.3	2.6	3.5	2.4	2.7	2.7	1.0	3.2	TRIMBLE
East	3.9	3.8	3.8	2.9	4.0	3.9	3.8	3.8	1.6	4.2	JAVAD
	3.6	3.4	3.7	2.8	3.6	3.4	2.9	3.5	1.6	3.4	LEICA
	3.6	3.6	3.6	2.9	3.6	3.4	3.2	3.4	1.7	3.2	SEPT
	3.9	3.6	3.8	3.0	3.9	3.9	3.4	3.7	1.9	3.9	TRIMBLE
Up	6.6	6.4	6.8	4.5	7.5	5.8	5.4	5.9	3.6	6.8	JAVAD
	6.7	6.2	7.3	5.0	6.4	5.9	5.1	6.9	4.1	5.4	LEICA
	6.8	7.5	7.9	4.8	7.2	6.0	7.1	7.6	3.9	6.8	SEPT
	7.4	6.3	7.6	4.8	7.4	7.0	5.3	7.4	3.8	7.0	TRIMBLE

In addition to the position evaluation, the convergence time was also performed, and the results are shown in Figure 3.12 and Table 3.6. The convergence period is defined as achieving a three-dimensional positioning error less than the predefined threshold at the current epoch and the subsequent twenty epochs. When the positioning biases for all twenty epochs fall within the threshold, the position is considered to have converged. In this thesis, the threshold is set at 10 cm.

As can be seen from Figure 3.12 and Table 3.6, the convergence time is generally shorter when the ISB is considered in the processing model for all the MGEX products. In particular, including the ISB in the processing model, the convergence time using SHA products requires a maximum of about 49 minutes to achieve a 10 cm-level positioning accuracy in the North component. To achieve the same level of accuracy in the North direction, it only takes 11 minutes when using IAC products. Nevertheless, the maximum time it can take to achieve the 10 cm accuracy in the East and Up directions is about 56 minutes and 50 minutes with SHA and IAC products, respectively. It is worth highlighting that better performance in the convergence period is true when the ISB is involved in the processing model. Generally, GBM products perform the best among all the products in terms of convergence time when the ISB is considered.

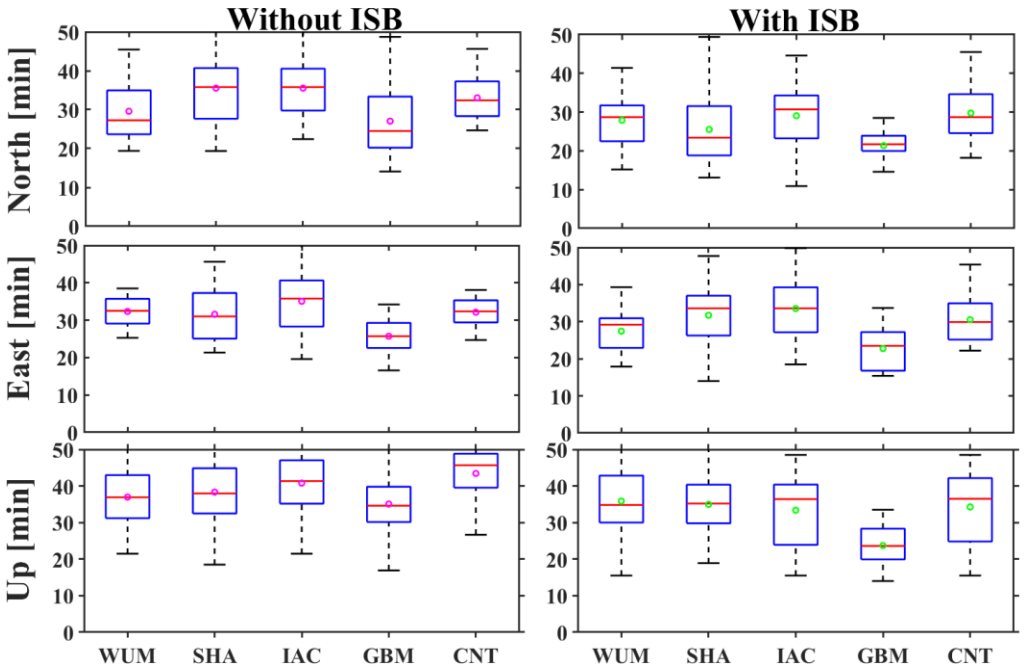

Figure 3.12: PPP convergence time using different MGEX products.

Table 3.6: PPP convergence time using different MGEX products (unit: min).

	Without ISB					With ISB					Remarks
	WUM	SHA	IAC	GBM	CNT	WUM	SHA	IAC	GBM	CNT	
North	45.4	51.5	50.2	48.7	45.6	41.4	49.4	44.6	28.5	45.5	Max
	27.3	35.8	35.8	24.5	32.4	28.7	23.4	30.7	21.7	28.7	Median
	29.6	35.5	35.5	27.0	33.0	27.9	25.5	29.1	21.4	29.7	Mean
	19.4	19.4	22.4	14.1	24.7	15.2	13.1	10.9	14.6	18.2	Min
East	38.5	45.6	51.4	34.2	38.1	39.3	47.7	49.8	33.7	45.4	Max
	32.5	31.0	35.8	25.7	32.4	29.2	33.6	33.6	23.5	29.9	Median
	32.3	31.6	35.1	25.7	32.1	27.4	31.7	33.5	22.8	30.5	Mean
	25.3	21.3	19.6	16.6	24.7	17.9	14.0	18.5	15.4	22.2	Min
Up	56.9	55.8	57.4	54.1	50.4	54.2	55.6	48.5	33.5	48.5	Max
	36.9	37.9	41.3	34.6	45.7	34.8	35.2	36.4	23.6	36.5	Median
	37.0	38.3	40.8	35.1	43.4	35.9	35.0	33.4	23.7	34.3	Mean
	21.5	18.5	21.5	16.9	26.7	15.5	18.9	15.5	14.0	15.5	Min

To thoroughly evaluate the ISB between BDS-2 and BDS-3, different receiver and antenna types were used in consideration of the characteristic property of ISB. The ISB depend on the receiver and antenna types. Besides that, the ISB also largely depend on

the GNSS clock products, because the specified time in the clock products is needed to define the system time scales for individual satellite systems. Since the MGEX products implement different time scales for the different navigation systems, the ISB influences at the user level will be different. The ISB instability may be attributed to the inconsistencies in the ISB handling schemes on the server-side in distinct ACs during the precise orbit determination and clock estimation process. The ISBs are usually estimated as constant parameters on the user side, and this could be convenient if the same handling scheme is used at the server. While the ISB may be considered constant within a day, it should be noted that this characteristic is valid for receivers of the same type. Thus, to establish the influence of the ISB on the integrated BDS-2 and BDS-3 processing, the improvement in Figure 3.13 and Table 3.7 are accounted for.

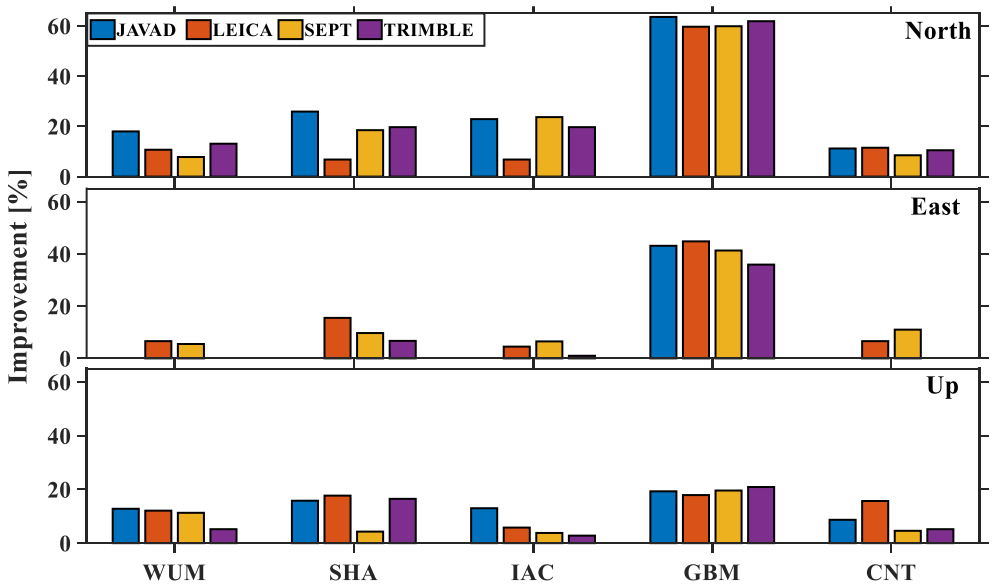

Figure 3.13: Improvement in positioning performance among different receiver types.

Table 3.7: Improvement in positioning performance and convergence time (%).

	Positioning Performance					Convergence Time				
	WUM	SHA	IAC	GBM	CNT	WUM	SHA	IAC	GBM	CNT
North	13.2	18.5	20.3	60.9	11.6	5.7	28.2	18.2	21.0	10.0
East	2.8	6.9	3.3	41.7	3.3	15.1	-	4.4	11.4	5.0
Up	10.8	9.9	6.0	21.0	8.0	3.0	8.7	18.2	32.3	21.1

3.5.3.2 ISB Validation Using Residuals

To further demonstrate the effect of the ISB on BDS data processing, the phase and code residuals were used. These are part of the output in Section 3.5.2 and a single station was selected for illustration purposes. For this example, the residuals for the SGOC station estimated using GBM products were used. Figures 3.14 and 3.15 show the phase and code residuals at SGOC with respect to elevation angle without and with ISB, respectively, on DOY 001 in 2021.

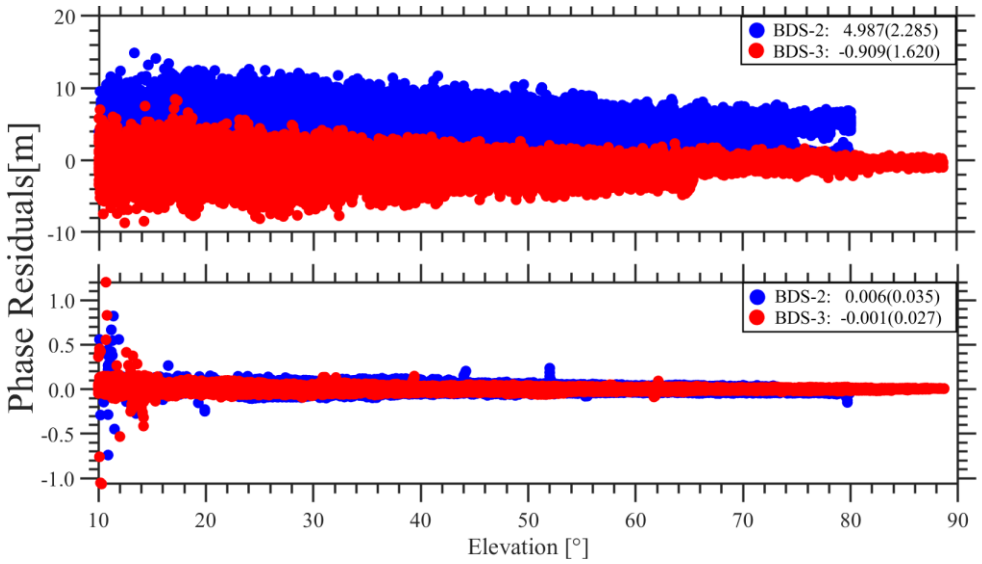

Figure 3.14: BDS residuals using GBM products without ISB at SGOC station.

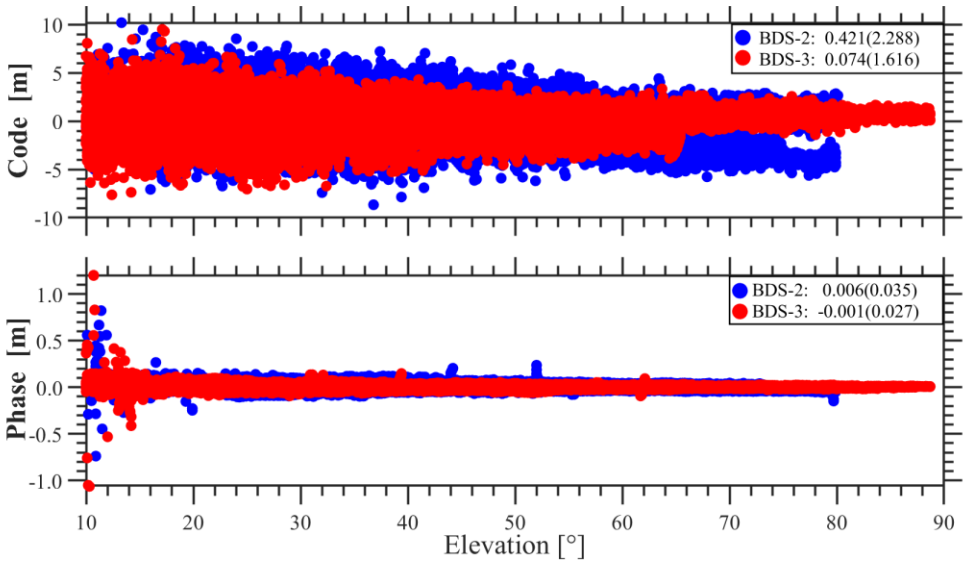

Figure 3.15: BDS residuals using GBM products with ISB at SGOC station.

The BDS-2 code residuals estimated without ISB have a mean of about 4.987 m and a STD of about 2.285 m, whereas those estimated with ISB have a mean of about 0.421 m and a STD of about 2.288 m. This shows a significant drop in code residuals for BDS-2. A similar trend can be noticed in the BDS-3 code residuals, in which the averaged code residuals drop from -0.909 m (without ISB) to 0.074 m (with ISB). It is worth mentioning that averaged code residuals estimated with ISB for both BDS-2 and BDS-3 are 12 times smaller than those estimated without the ISB parameter. Thus, considering the ISB in the PPP processing model significantly reduces the code residual errors. Based on this observation, it can be discerned that when the ISB parameter is ignored in the code observable, it will be absorbed by the combined code residuals for BDS-2 and BDS-3. On the contrary, the improvement in the residual errors is not reflected in the carrier phase residuals for both BDS-2 and BDS-3, as can be evidenced from Figures 3.14 and 3.15.

Further to the residuals discussed above, another experimental test was conducted to calculate residuals with and without the ISB parameter. Using the stations presented in Figure 3.2, two weeks of observations (from DOY 001-014, 2021) were processed, and the STDs are depicted in Figure 3.16. The blue and red bars indicate the overall residuals for BDS, estimated with and without the ISB. The upper and lower panels illustrate the code (Figure 3.16a) and phase (Figure 3.16b) residuals, respectively. The

numeric values enclosed in the parentheses represent the mean STDs for the two processing schemes. As can be seen, the residuals processed with the ISB parameter have slightly lower STDs than those estimated without the ISB parameter for both code and phase measurements. Generally, the phase residuals exhibit marginal differences between the two schemes.

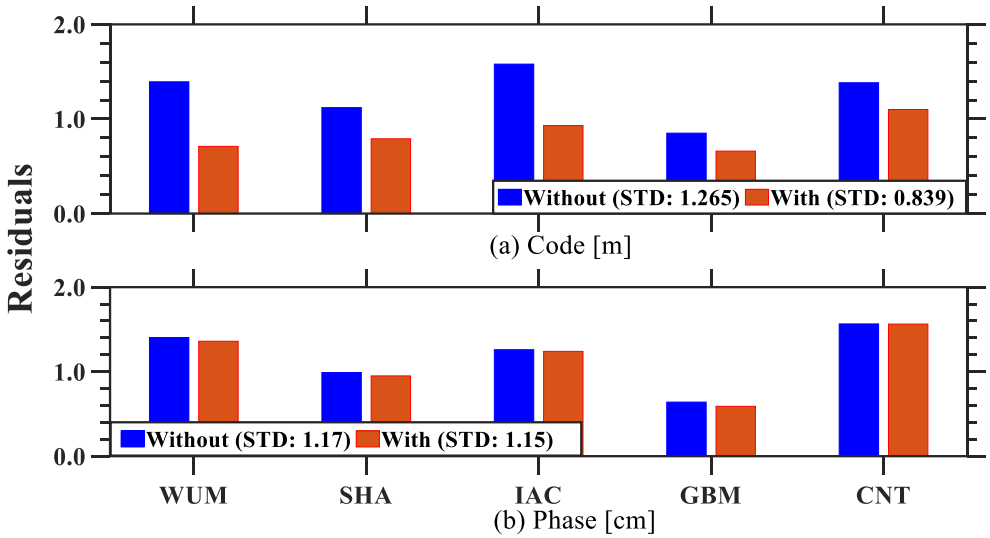

Figure 3.16: BDS code and phase residuals estimated with and without ISB.

Another experimental case is given in Figure 3.17 in which code residuals estimated at four stations are compared. As can be seen, the BDS-2 and BDS-3 code residuals almost overlap at each station. There is a marginal difference between the estimated code residuals for BDS-2 and BDS-3 at the ALIC station. Similarly, the estimated code residuals exhibited smaller standard deviations (STDs) at the FALK station for both BDS-2 and BDS-3. Moreover, for BDS-3, both PTGG and DGAR have an STD of about 1.2 m. In the case of BDS-2, the code residuals are estimated with STDs of about 1.5 and 1.3 cm at DGAR and PTGG, respectively. In general, BDS-3 demonstrates slightly better precision at FALK, DGAR, and PTGG than BDS-2.

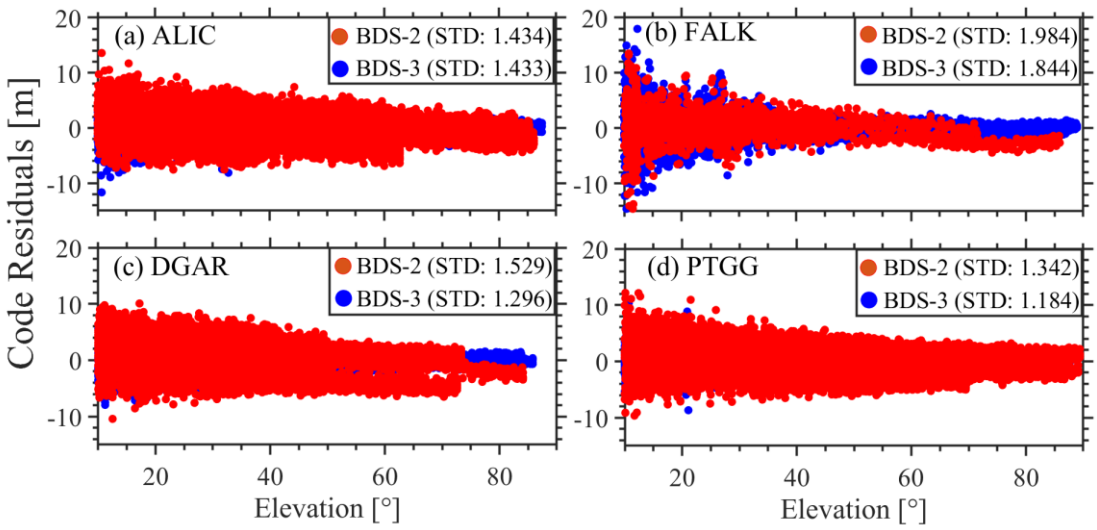

Figure 3.17: BDS residuals using CNT products with ISB.

3.6 Chapter Summary

The handling of ISB is necessary especially when different satellite systems are involved in the data processing. In this Chapter, the PPP functional model is parameterised to account for BDS-2 and BDS-3 interoperable signals and the ISB. A strategy for improving BDS-2 and BDS-3 combined data processing is suggested, in which MGEX products generated by different analysis centers are employed. The quality of the MGEX products is evaluated before PPP validation. The numerical results indicate that the GBM products achieve the best performance in positioning and convergence time. Furthermore, the effects of the ISB is demonstrated to be more significant on code than phase observations.

Chapter 4: Handling of BDS Hardware Biases

4.1 Introduction

In multi-GNSS data processing, a proper handling of hardware biases is necessary to achieving meaningful PNT solutions. As reviewed in Chapter 2, the common approach for estimating hardware biases has been limited in the number of signals involved in the models. This chapter firstly investigates the equivalence between the dual- and triple-frequency models for estimating the hardware biases, followed by extending the model to quad-frequency or even more signals using BDS constellation. Moreover, a possible data processing scheme is suggested to further improve the estimation strategy.

4.2 Time-Invariant and Time-Variant Biases

The receiver and satellite biases are split into two parts, namely, the time-invariant (independent) and time-variant (dependent) biases. In Equation (4.1), $\delta_{\Phi,i}$ and $\Delta\delta_{\Phi,i}$ are the time-invariant and time-variant receiver phase biases; whereas δ_{Φ}^{k} and $\Delta\delta_{\Phi}^{k}$ are the time-invariant and time-variant satellite phase biases. Similarly, $\delta_{P,i}$ and $\Delta\delta_{P,i}$ are the time-invariant and time-variant receiver code biases; whereas δ_{P}^{k} and $\Delta\delta_{P}^{k}$ are the time-invariant and time-variant satellite code biases. Mathematically, the satellite ($\hat{\delta}_{fi,\Phi}^{k}$ and $\hat{\delta}_{fi,P}^{k}$) and receiver ($\hat{\delta}_{fi,\Phi}$ and $\hat{\delta}_{fi,P}$) biases can be expressed as

$$\begin{cases} \hat{\delta}_{fi,\Phi} = \delta_{fi,\Phi} + \Delta\delta_{fi,\Phi} \\ \hat{\delta}_{fi,\Phi}^{k} = \delta_{f,\Phi}^{k} + \Delta\delta_{f,\Phi}^{k} \\ \hat{\delta}_{fi,P} = \delta_{fi,P} + \Delta\delta_{fi,P} \\ \hat{\delta}_{fi,P}^{k} = \delta_{f,P}^{k} + \Delta\delta_{f,P}^{k} \end{cases} \tag{4.1}$$

where $\hat{\delta}^{k}_{fi,\Phi}$ and $\hat{\delta}^{k}_{fi,P}$ denote the phase and code biases for the satellite, respectively, and $\hat{\delta}_{fi,\Phi}$ and $\hat{\delta}_{fi,P}$ denote the phase and code biases for the receiver, respectively.

The code biases are also termed as the code OSB, whereas the phase biases are also called the phase OSB. The treatment of such biases is an important aspect of GNSS data processing, and they are calibrated using DPB and DCB. As aforementioned, the DPB and DCB are also known as the phase OSB and code OSB, respectively. Another way of treating such biases is to lump them with other parameters in the estimation process. For example, in PCE, the time-dependent code, and phase delays are absorbed by the time-dependent components of the IF combination. In general, the treatment of variant and invariant biases may take the form illustrated in Figure 4.1 below.

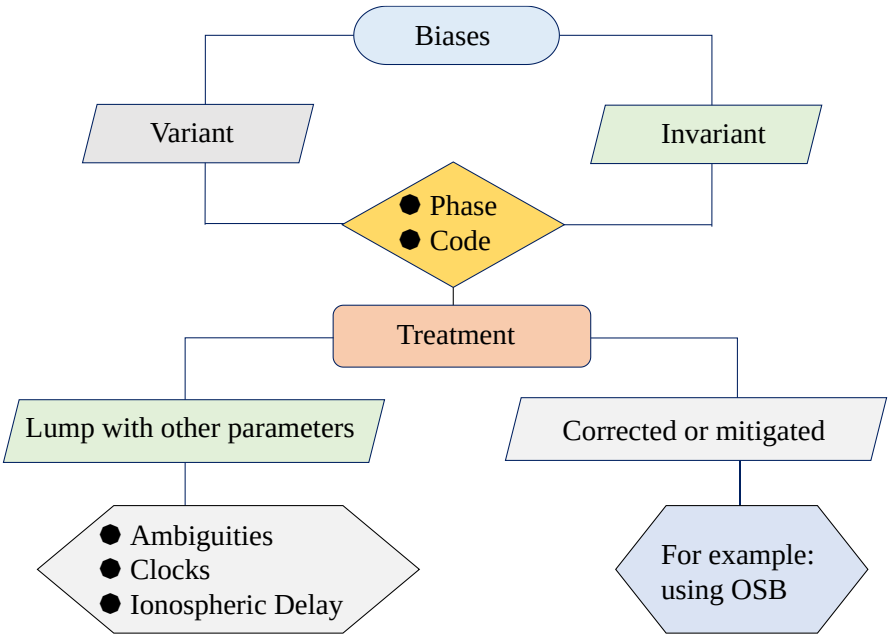

Figure 4.1: Treatment of variant and invariant biases.

4.3 Theoretical Fundamentals of Hardware Bias Estimation

For satellites operating on the CDMA, the receiver UPD are common to all satellites of the same type. Likewise, for GLONASS which operates on frequency division multiple access (FDMA), the UPD are common per frequency number. A priori knowledge of hardware biases is more salient, especially in PPP-ambiguity with resolution (PPP-AR), in precise clock estimation (PCE), and in any other high-precision positioning. An example of the treatment of UPD is demonstrated in Equation (4.2) where the time-dependent and time-independent phase biases are lumped with other parameters in the estimation model. It is repeated here for convenience as

$$\begin{cases} \Phi_{fi}^{k} = \rho_{i}^{k} + c \cdot \left(\Delta t_i + \delta_{fi,\Phi} + \Delta\delta_{fi,\Phi}\right) - c \cdot \left(\Delta t^{k} + \delta_{f,\Phi}^{k} + \Delta\delta_{f,\Phi}^{k}\right) + \\ \qquad MF \cdot ZWD_{i}^{k} + \lambda_f N_{fi}^{k} + \epsilon_{fi}^{k} \\ P_{fi}^{k} = \rho_{i}^{k} + c \cdot \left(\Delta t_i + \delta_{fi,P} + \Delta\delta_{fi,P}\right) - c \cdot \left(\Delta t^{k} + \delta_{f,P}^{k} + \Delta\delta_{f,P}^{k}\right) + \\ \qquad MF \cdot ZWD_{i}^{k} + \varepsilon_{fi}^{k} \end{cases} \tag{4.2}$$

The scenario demonstrated in Equation (4.2) presents one way of treating biases in GNSS data processing whereby the time-independent and time-dependent biases lump with the receiver and satellite clocks. In addition to that approach, the biases may also lump with the ambiguity parameters as indicated in Equation (3.3) in Chapter 3. In such a case, the ambiguity terms lose the integer property, and this may result in a decrease in the accuracy and reliability of positioning performance. Hence, acquiring the ambiguity-fixed solution becomes a crucial issue for PPP performance.

The bias handling scheme in Equation (4.2) is a form of parameterisation without which it may be difficult to estimate the biases due to linear dependency. Contrary to PPP, in PPP-RTK the phase biases do not lump with other parameters (Figure 2.1). Thus, proper parameterisation becomes appropriate to make the biases estimable. One merit of PPP-RTK lies in its capacity to resolve ambiguities (Teunissen and Khodabandeh, 2015a). The other strength lies in its capability to transmit the satellite UPD and UCD to users. As presented in Chapter 2, there are different approaches for achieving ambiguity resolution. Apart from the use of UPD and UCD in PPP, the following may also be

used: integer phase clocks, integer recovery clocks (IRC), decoupled satellite clock, and the FCB. As the name suggests, the UPD and UCD estimate the delay without prior calibration. The integer phase clock determines the integer number of cycles based on the phase measurements. On the other hand, the IRC implements a tracking loop to recover integer cycles. In the case of the decoupled satellite clock, the clock bias and drift of each satellite are estimated independently to reduce inter-satellite clock bias errors. Unlike the approaches above, the FCB measures the difference between the received carrier phase and the expected carrier phase in order to achieve high precision. Therefore, the users may apply such biases in PPP to resolve ambiguity.

4.4 OSB in GNSS Data Processing

The evolution of multi-frequency constellations has led to a significant expansion in the number of satellites capable of transmitting three or more frequencies. These advancements have propelled the GNSS field forward, enabling greater precision and accuracy in satellite-based positioning and navigation applications.

Despite such advances in the GNSS community, it becomes hard with multi-frequency signals to ensure compatibility and interoperability between the server side and the PPP user (Geng et al., 2022). Thus, to ensure compatibility between different hardware delay products, it is imperative to establish consistent mathematical models on both the network and user sides. According to Villiger et al. (2019), the OSB recorded in the SINEX format can provide users with observable-specific satellite code and phase bias corrections for each frequency, which can be directly applied to raw observations without consideration of the mathematical models used by the network side. This does not only assist in improving the positioning performance, but it also simplifies the multi-frequency PPP with ambiguity resolution.

Currently, the IGS have been providing the OSB products generated by different ACs since January 2022. Since BDS has two different constellations, Table 4.1 summarises the OSB products that support BDS frequency signals. From this table, all the ACs

generate products with an update rate of one-day except CNES, which releases two different products at five-seconds and thirty-seconds for real-time and post-processing applications, respectively. Further details about the characteristics of such products can be found in Laurichesse and Blot (2016), for example. While the AC continue to update their products due to the increase in the number of stations with BDS tracking capability, still most products do not support all the BDS signals. For instance, most of them support the B1I and B3I signals. It is only CNES which generates products that support the most signals including the BDS-3 five frequency signals (B1C, B1I, B2I, B2a and B3I).

Table 4.1: The OSB products for BDS constellation.

AC	Frequency	Update Rate	Constellation
WUM	B1I/B3I	1 Day	BDS-2
	B1I/B3I		BDS-3
CNES	B1I/B3I	5 seconds	BDS-2
	B1I/B3I		BDS-3
	B1I/B2I/B3I	30 seconds	BDS-2
	B1C/B1I/B2I/B2a/B3I		BDS-3
GFZ	B1I/B3I	1 Day	BDS-2
	B1I/B3I		BDS-3

Besides that only limited signals for BDS are currently supported in the OSB products, the PCO at each individual signal for BDS-3 is also different from that of the other GNSS constellations. Therefore, it is crucial to consider the PCO in the estimation of OSB for BDS constellation including its impact on PPP performance. In the domain of estimating OSB, different techniques have been reported in the literature with proper accounts on the treatment of hardware biases in both floating and ambiguity-fixed solutions. For both scenarios, the overall hardware bias handling schemes are generally similar for all signals based on code CDMA such as in El-Mowafy et al. (2016), and on frequency division multiple access FDMA, for example in Liu et al. (2017).

As described in Chapter 2, out of the methods for estimating biases, the solid ones may be generalized as threefold: the EWD technique, the GF/IF strategies, and satellite clock estimation. For efficient estimation of the OSB, the EWD method reduces the computational burden through eliminating the ambiguities by differencing them between successive epochs (Fan et al., 2019). Based on the GF/IF approach, the OSB parameterisation has been implemented to simplify the handling of both pseudorange and carrier phase biases (Villiger et al., 2019), in which BDS-2, Galileo, GPS, and GLONASS OSB were analysed for validation. Further studies have been recently undertaken to estimate OSB using similar multi-GNSS that not only include BDS-2 but also BDS-3 constellation, for example in Su and Jin (2021).

As pointed out by Villiger et al. (2019), the OSB corrections may not be sophisticated in terms of implementation, as they are easily utilised in real-time GNSS applications. On the other hand, their applicability in post-processing scenarios may not be straightforward, as they involve a parameterisation that requires a proper specification of signals in the normal equations. An instance of such parameterisation was demonstrated by Geng et al. (2019), in which a modified method for generating daily OSB products using integer clocks and phase delays was proposed. In their modified model, comparable positioning performance was achieved in different PPP scenarios using both the integer clock model and the OSB products. Despite such implementation, the computation of the OSB for BDS is based on the dual-frequency observations (Table 4.1) than a quad or more signals.

Thus, this work takes advantage of multi-frequency signals to parameterise the code and phase OSB using BDS-3 signals. Instead of estimating the OSB using only the dual-frequency approach, it is proposed to accommodate the estimation of the OSB using the multi-frequency signals (involving three or more signals). Since BDS constellations can allow quad- and even five-frequency precise positioning independently, this thesis benefits from those multiple frequencies by undertaking quad-frequency validations for this satellite system. Moreover, the estimated OSB may be systematically affected by heterogeneous receivers tracking multiple observations from different GNSS. Thus, prior knowledge of the existence of errors and biases in different positioning algorithms is crucial, as the errors and biases may not have identical characteristics. This may be true for signals belonging to both different and the same constellations.

4.4.1 Estimation of Dual-Frequency OSB

Currently, geodetic receivers have the capability to track quad- or more frequency GNSS signals (further details are presented in Section 4.5.1). In the case of dual-frequency combinations, the PPP technique permits the precise determination, and in some cases elimination, of the ionospheric path delay. Consequently, combining multiple frequencies to produce wide-lane (WL) observables proves highly valuable in isolating carrier-cycle integer ambiguities. The Melbourne–Wu¨bbena (MW) combination serves to eliminate the impact of ionospheric delay, geometric distance from the satellite to the receiver, satellite clock, and receiver clock. The resulting data is primarily influenced by factors such as multipath effects, observation noise, and OSBs.

Typically, the generation of dual-frequency OSBs involves a three-step process. Initially, the MW combination is utilised to generate the WL biases. Next, the IF phase observations are employed to obtain narrow-lane (NL) biases. Lastly, the OSB for each signal can be generated from the estimated WL and NL biases. The mathematical relation for the transformation of OSB applied in PPP is presented in Teunissen and Khodabandeh (2015b) and Banville et al. (2020). From their studies, the estimation of OSB in a dual-frequency scenario can be summarised as shown in Figure 4.2 below.

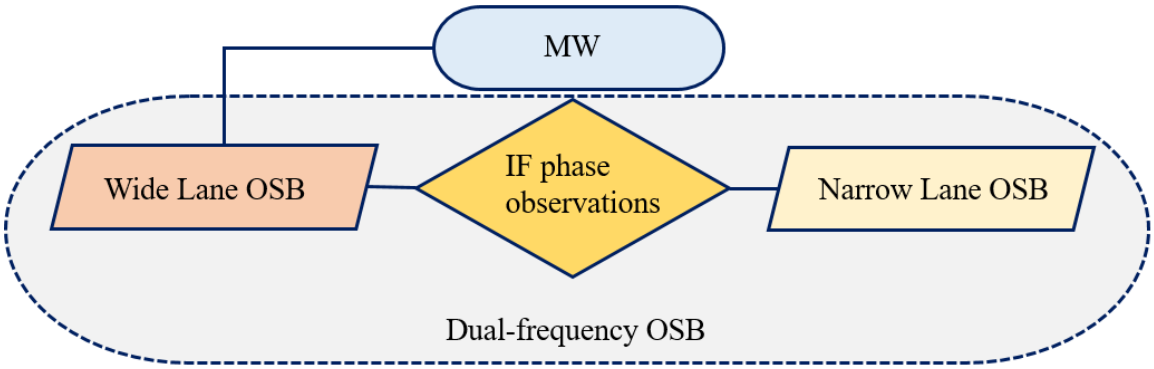

Figure 4.2: Estimation of dual-frequency OSB.

On the network side, the MW algorithm is used to compute the WL OSB. For a given receiver and satellite for a particular constellation, the dual-frequency MW combination can be expressed as follows:

$$\Phi_{i,MW}^{k} = \Phi_{i,f}^{k} + P_{i,f}^{k} \tag{4.3}$$

with

$$\begin{cases} \Phi_{i,f}^{k} = \left[\dfrac{f_1^k}{(f_1^k - f_2^k)}\right]\Phi_{i,1}^{k} + \left[\dfrac{-f_2^k}{(f_1^k - f_2^k)}\right]\Phi_{i,2}^{k} \\ P_{i,f}^{k} = \left[\dfrac{-f_1^k}{(f_1^k + f_2^k)}\right]P_{i,1}^{k} + \left[\dfrac{-f_2^k}{(f_1^k + f_2^k)}\right]P_{i,2}^{k} \end{cases}$$

In Equation (4.3), the $\frac{f_1^k}{(f_1^k - f_2^k)}$ and $\frac{-f_2^k}{(f_1^k - f_2^k)}$ denote the WL combination factors; $\frac{-f_1^k}{(f_1^k + f_2^k)}$ and $\frac{-f_2^k}{(f_1^k + f_2^k)}$ denote the NL combination factors; the subscripts 1 and 2 denote the frequency signals such as B1I and B3I for BDS constellation, respectively.

In order to compute the OSB for both the receiver and the satellite, Equation (4.2) is substituted into Equation (4.3) to obtain

$$\Phi_i^k = \frac{c}{\left(f_1^k - f_2^k\right)}\left(N_{i,1}^k - N_{i,2}^k\right) + \hat{\delta}^k + \hat{\delta}_i + \Delta\widehat{PCO}_{i,WL}^k + \Delta\widehat{PCO}_{i,NL}^k \tag{4.4}$$

with

$$\begin{cases} \hat{\delta}^k = \alpha_{WL}^k \delta_{1,\Phi}^k + \beta_{WL}^k \delta_{2,\Phi}^k + \alpha_{NL}^k \delta_{1,P}^k + \beta_{NL}^k \delta_{2,P}^k \\ \hat{\delta}_i = \alpha_{WL} \delta_{i,1,\Phi} + \beta_{WL} \delta_{i,2,\Phi} + \alpha_{NL} \delta_{i,1,P} + \beta_{NL} \delta_{i,2,P} \\ \Delta\widehat{PCO}_{i,WL}^k = \alpha_{WL} \Delta PCO_{i,1}^k + \beta_{WL} \Delta PCO_{i,2}^k \\ \Delta\widehat{PCO}_{i,NL}^k = \alpha_{NL} \Delta PCO_{i,1}^k + \beta_{NL} \Delta PCO_{i,2}^k \end{cases}$$

In Equation (4.4), $\frac{c}{\left(f_1^k - f_2^k\right)}$ and $N_{i,f}^k\ (f)$ denote the wavelength and WL ambiguity, respectively; $\hat{\delta}^k$ and $\hat{\delta}_i$ denote the WL biases for the satellite and receiver, respectively. Note that this combines the phase and code biases for both the satellite and receiver; $\Delta\widehat{PCO}_i^k$ denotes the PCO corrections. Thus, if

$$PCO_1 \equiv PCO_2 = \Delta\widehat{PCO}_i^k = 0 \tag{4.5}$$

meaning that PCO will cancel out when the corrections at the two frequencies are equal. Therefore, the estimated OSB for the two signal frequencies should hold as presented in (4.4) above, that is

$$\hat{\delta}^k = \alpha_{WL}^k \delta_{i,1,\Phi}^k + \beta_{WL}^k \delta_{i,2,\Phi}^k + \alpha_{NL}^k \delta_{i,1,P}^k + \beta_{NL}^k \delta_{i,2,P}^k \tag{4.6}$$

where $\delta_{i,1,\Phi}^k$ and $\delta_{i,1,P}^k$ denote the phase and code OSB for the first frequency; $\delta_{i,2,\Phi}^k$ and $\delta_{i,2,P}^k$ denote the phase and code OSB for the second frequency. For the sake of the BDS-3 constellation, this could be any dual-frequency signals such as B1I and B3I. Different signal combinations can be formulated from the BDS frequency signals (summarised in Table 1.2, Chapter 1). By applying $\lambda_f = \frac{c}{f_1 - f_2}$ scaled by 10^6 Hz, the

wavelengths for different combinations can be deduced in units of meters. Table 4.2 summarises the MW combinations and their corresponding wavelengths.

Table 4.2: MW combinations for BDS signals.

SN	Signal Combination	Wavelength (m)
1	B1I-B1C	20.92
2	B3I-B2a	3.30
3	B1I-B3I	1.03
4	B1C-B2b	0.82
5	B1I-B2a+b	0.81
6	B1I-B2	0.85
7	B2-B3I	7.61
8	B2a-B2b	19.56

4.4.2 Estimation of Multi-Frequency OSB

Depending on the number of frequencies used in the model, the biases can either be eliminated or estimated. For example, when the users apply the same kind of observations as those released by the clock solution providers, the biases will cancel out. On the contrary, the biases cannot be ignored in a multi-frequency scenario involving three or more signal frequencies. In such a situation, the biases at the third frequency may be estimated or corrected.

In the case of OSB using three or more signals, the mathematical model is derived in this thesis. Firstly, the triple-frequency IF is introduced by taking the linear combination of three GNSS signals as

$$\Phi_{r,IF3}^{k} = \frac{f_1}{(f_1 - f_j)} \frac{c}{(f_1^k - f_2^k)} \left(\frac{\Phi_{i,1}^{k}}{\lambda_1} - \frac{\Phi_{i,2}^{k}}{\lambda_2} \right) + \frac{-f_j}{(f_1 - f_j)} \frac{c}{(f_2 - f_j)} \left(\frac{\Phi_{i,2}^{k}}{\lambda_2} - \frac{\Phi_{r,j}^{k}}{\lambda_j} \right) \tag{4.7}$$

where the $\Phi^k_{r,IF3}$ denotes the triple-frequency IF phase combination; the subscripts 1, 2, and j denote the triple-frequency signals; $\frac{c}{(f_2-f_j)}$ denotes the wavelength of the extra-wide lane (EWL). This wavelength is called EWL because it is formulated based on the 2 and j ($f \geqslant 3$) which is the multi-frequency scenario as presented in Equation (4.8); $\frac{-f_j}{(f_1-f_j)}$ and $\frac{c}{(f_2-f_j)}$ denote coefficient of the EWL ambiguity and can be computed directly. As illustrated in Figure 4.2, the ambiguity parameter absorbs the time-variant biases during this ED estimation. In a multi-frequency GNSS data processing scenario, the linearised $\Phi^k_{i,f}$ involving three or more frequency signals can be expressed as

$$\begin{cases} \Phi^k_{i,1} = \rho^k_i + \Delta\hat{t}_i + MF^k_i \cdot ZWD_i - \hat{I}^k_{i,1} + \lambda_1 \widehat{N}^k_{i,1} + \epsilon^k_{i,1} \\ \Phi^k_{i,2} = \rho^k_i + \Delta\hat{t}_i + MF^k_i \cdot ZWD_i - \mu_2 \cdot \hat{I}^k_{i,1} + \lambda_2 \widehat{N}^k_{i,2} + \epsilon^k_{i,2} \\ \Phi^k_{i,j} = \rho^k_i + \Delta\hat{t}_i + MF^k_i \cdot ZWD_i - \mu_j \cdot \hat{I}^k_{i,1} + \lambda_j \widehat{N}^k_{i,j} + \Delta\delta^k_j + \epsilon^k_{i,j} \end{cases} \quad (4.8)$$

with

$$\Delta\hat{t}_i = c\left(\Delta t_i + \hat{\delta}_{fi,\Phi}\right) - c\left(\Delta t^k + \hat{\delta}^k_{fi,\Phi}\right)$$

As per Equation (4.8), $\Delta\delta^k_j$ denotes the time-dependent phase bias. Generally, the dual-frequency phase combination is necessary for the OSB estimation, for example, $\Phi^k_{i,1}$ and $\Phi^k_{i,2}$. One way of separating the bias from the clock is to apply the IRC, and during this process, a datum for the ambiguity parameter should be established beforehand.

The fundamental concept behind the clock model involves assuming the stability of the WL phase bias within a single day. This model seeks to estimate the WL ambiguity through MW combination, where the fractional part of the WL ambiguity estimation becomes the WL phase bias, and the integer part represents the WL integer ambiguity. Subsequently, the fixed WL ambiguity is incorporated into the IF combination to address the NL ambiguity. Rounding the resolved NL ambiguity absorbs the corresponding NL phase bias into the clock parameters. While the integer clock model

demonstrates high positioning accuracy, its satellite clock product is incompatible with the IGS legacy clock product and DCB product.

According to Teunissen and Khodabandeh (2015), this makes the computed clock terms lump with the phase delays other than the code delays. As a convention by the IGS, the estimation of the biases is based on the specific types of clocks. To recover the biases, the disparity between the IGS legacy clocks and the integer clocks can be expressed as follows

$$\left.\begin{aligned}\Delta\check{t}^{k} &= \alpha_{IF}\check{\delta}^{k}_{1,i} + \beta_{IF}\check{\delta}^{B}_{2,i} \\ &= \alpha_{IF}\check{\delta}^{k}_{1,i} + (\alpha-1)_{IF}\check{\delta}^{B}_{2,i}\end{aligned}\right\} \tag{4.9}$$

where $\Delta\check{t}^{k}$ denotes the deviation between the IGS legacy clock and integer clock; $\check{\delta}^{B}_{1,i}$ and $\check{\delta}^{B}_{2,i}$ denote the transformed OSB for B1I and B3I signal frequencies, respectively. From the approaches presented above, the estimated OSB at each signal is related to the satellite clock product and the AC time offset as

$$\begin{cases}\Delta\hat{t}^{k} - \check{\delta}^{k}_{1} = \Delta t^{k} - \Delta t_{AC} - \delta^{k}_{1} \\ \Delta\hat{t}^{k} - \check{\delta}^{k}_{2} = \Delta t^{k} - \Delta t_{AC} - \delta^{k}_{2} \\ \Delta\hat{t}^{k} - \check{\delta}^{k}_{j} = \Delta t^{k} - \Delta t_{AC} - \hat{\delta}^{k}_{j}\end{cases} \tag{4.10}$$

where $\Delta\hat{t}^{k}$ denotes the computed satellite clock; the Δt_{AC} denotes the time offset for the AC. Therefore, to restore the integer properties of the ambiguity parameters for each frequency signal, Equation (4.10) is substituted into the carrier phase observations Equation (4.8) to obtain the following expression:

$$\begin{cases} \Phi_{i,1}^{k} + \Delta\hat{t}^{k} - \hat{\delta}_{1}^{k} = \rho_{i}^{k} + \Delta\hat{t}_{i}^{k} + MF_{i}^{k} \cdot ZWD_{i} - \hat{I}_{i,1}^{k} + \lambda_{1}\widehat{N}_{i,1}^{k} + \delta_{i,1} + \epsilon_{i,1}^{k} \\ \Phi_{i,2}^{k} + \Delta\hat{t}^{k} - \hat{\delta}_{2}^{k} = \rho_{i}^{k} + \Delta\hat{t}_{i}^{k} + MF_{i}^{k} \cdot ZWD_{i} - \mu_{2}\hat{I}_{i,1}^{k} + \lambda_{2}\widehat{N}_{i,2}^{k} + \delta_{i,2} + \epsilon_{i,2}^{k} \\ \Phi_{i,j}^{k} + \Delta\hat{t}^{k} - \hat{\delta}_{j}^{k} = \rho_{i}^{k} + \Delta\hat{t}_{i}^{k} + MF_{i}^{k} \cdot ZWD_{i} - \mu_{j}\hat{I}_{i,1}^{k} + \lambda_{j}\widehat{N}_{i,j}^{k} + \delta_{i,j} + \epsilon_{i,j}^{k} \end{cases} \quad (4.11)$$

From the derivation above, it can be observed that the integer property for each frequency signal can be recovered using the EW estimation approach. It is also worth noting that, in order to eliminate rank deficiency, the zero mean condition is imposed. Moreover, j in Equation (4.11) means that the model can be extended to quad- or more frequency signals. Therefore, in GNSS data processing, the user can apply the OSB to raw observations together with the reference clocks. For the sake of validation, the following section implements the multi-frequency PPP using OSB.

4.5 PPP Experimental Validation

The validation in this section recognises that geodetic receivers may track multiple observations from different GNSS satellites. Another issue is that the OSB may be systematically affected by heterogeneous receivers tracking such unique observation codes. Consequently, to test the developed model, the tests were carried out using observations from two different constellations. Specifically, observations from BDS-3 and Galileo constellations were used for performance validation because they both transmit quad- or more frequency signals.

4.5.1 Datasets for Model Validation

To evaluate the OSB, 30-second datasets spanning from DOY 121-151 in 2022 at 200 receivers were used. All the selected stations are denoted with a purple colour code in Figure 4.3. Out of the 200 stations, 70 can track quad-frequency signals for both BDS and Galileo constellations (Figure 4.4), and these stations are illustrated in yellow colour (Figure 4.3).

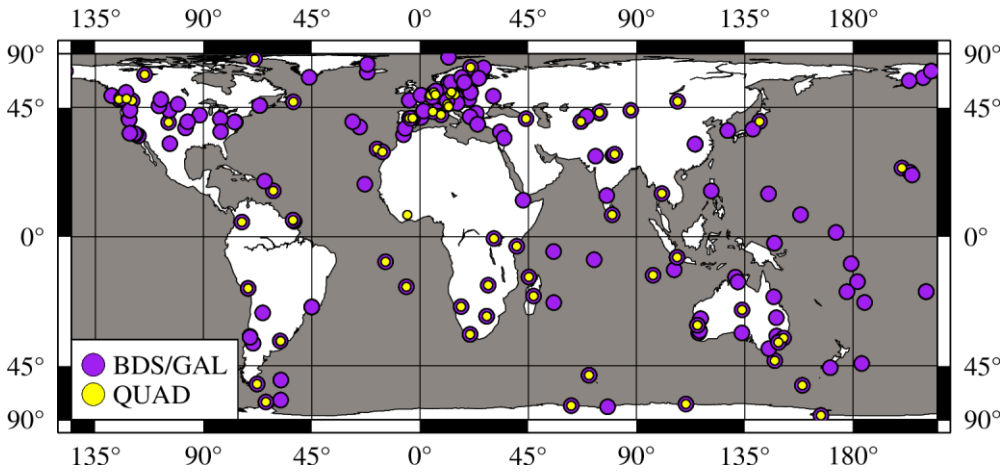

Figure 4.3: Distribution of the selected BDS and Galileo stations.

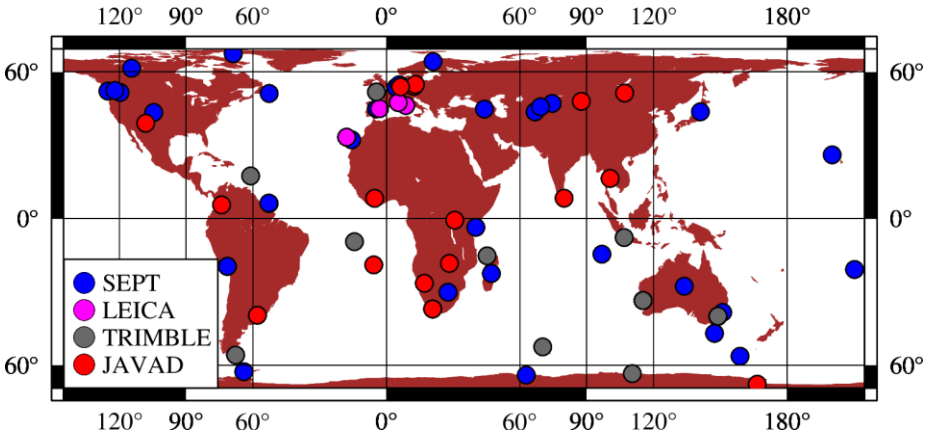

Figure 4.4: BDS and Galileo stations with quad-frequency tracking capability.

To fully characterise the performance, all the selected stations presented in Figure 4.3 were used to undertake the test. On the other hand, the stations supporting quad-frequency signals were used to evaluate the OSB. The reason is that the characteristics of the estimated OSB have not been fully evaluated based on receiver type in the existing literature. Thus, this chapter evaluates the temporal characteristics of the estimated OSB by considering different receiver manufacturers. As a consequence, the stations supporting quad-frequencies are broadly categorised into four groups based on receiver manufacture, namely, SEPT, LEICA, TRIMBLE, and JAVAD. The four

different types of receivers are shown in Figure 4.4, where the blue, magenta, dimgray, and red colour codes denote SEPT, LEICA, TRIMBLE, and JAVAD receivers, respectively.

It is worth mentioning that during the observation span, there are other receiver types that can observe BDS and Galileo signals such as CHC and STONEX receivers. However, they are not considered in this test due to the limited number of stations and lack of the required observations. In the case of receivers that reliably observe quad-frequency signals, their quantities out of the 70 receivers (Figure 4.4) are summarised in Table 4.3.

Table 4.3: Overview of BDS and Galileo stations that support quad-frequency signals.

SN	Manufacture	Number	Remarks
1	SEPT	39	POLARX5 (25), POLARX5TR (11), ASTERX4 (2), and POLARX5E (1)
2	LEICA	4	GR50
3	TRIMBLE	10	ALLOY
4	JAVAD	17	TRE_3 DELTA (7) and TRE_3 (10)
	Total	70	

The SEPT receivers comprises four different types of receivers, namely, POLARX5, POLARX5TR, ASTERX4, and POLARX5E. Another worth noting issue is that, all the LEICA and TRIMBLE receivers are GR50 and ALLOY, respectively, whereas JAVAD consists of two types including TRE_3 DELTA and TRE_3. For SEPT and JAVAD receivers, the numbers of stations are presented in parenthesis in Table 4.3. Since errors may not have identical characteristics, all the different types of receivers were employed in the experiment to extensively classify the magnitude of performance.

4.5.2 OSB Estimation and PPP Tests

Using the datasets described in Section 4.5.1 above, two main processing schemes were used, namely, quad- and the traditional dual-frequency kinematic PPP models. The quad-frequency models were employed to evaluate the OSB for BDS using the B1I/B3I/B1C/B2a signals. For the sake of validation, similar tests were undertaken using Galileo E1/E5a/E5b/E6 signals. Similarly, dual-frequency PPP models for both constellations were conducted using B1I/B3I and E1/E5a signals for BDS and Galileo, respectively. Similar to Chapter 3, the datasets were processed at an elevation cut-off angle of 10° to account for multipath errors.

At present, the satellite PCO corrections for the BDS-3 B2a frequency are unavailable. In the absence of these corrections, the PCO corrections for the B2a frequency are assumed to be identical to those for the B3I frequency. Additionally, since the receiver PCO/PCV values for Galileo and BDS-3 are still unavailable, it is presumed in this thesis that these corrections match those of GPS. Furthermore, the IGS weekly solutions were utilised to deduce the station positioning performance. As presented for the experimental validation in Chapter 3 (Table 3.4), the STDs for the carrier phase and pseudorange were set at 3 mm and 300 mm, respectively.

Moreover, to undertake the PPP experiments, CNES products introduced in Table 3.2 in Chapter 3 were used. These products include the satellite orbits, satellite clocks, and signals biases. Table 4.4 summarises the aforementioned products where the $*$.SP3, $*$.CLK, and $*$.BIA are the suffixes for the orbits, clocks, and signal biases, respectively.

Table 4.4: MGEX products used for PPP test.

SN	Product	Description
1	Orbit	$*$ .SP3
2	Clock	$*$ .CLK
3	Signal bias	$*$ .BIA

As an MGEX product, the CNES supports six satellite systems, including BDS-2, BDS-3, GPS, GLONASS, Galileo, and QZSS, and it provides the clocks and orbits at sampling intervals of 5 and 300 seconds, respectively. As 5independent GNSS with global coverage, Figure 4.5 illustrates the ground tracks for BDS and Galileo generated using CNES orbit product on DOY 151 in 2022.

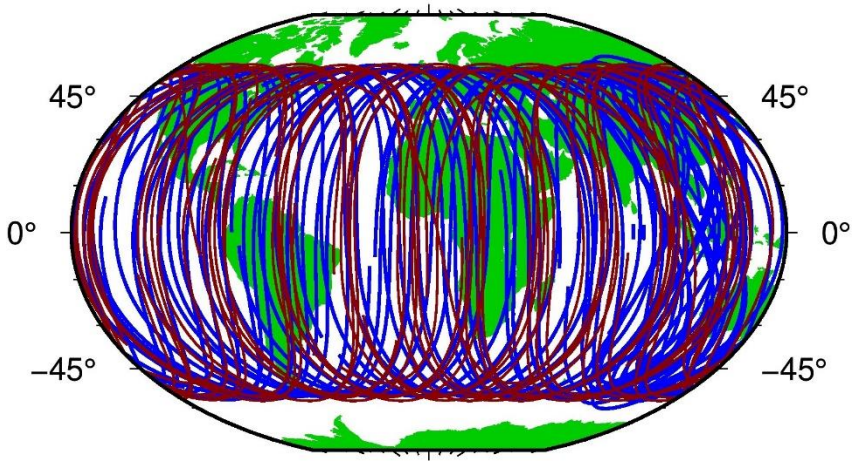

Figure 4.5: Ground tracks for BDS (blue) and Galileo (darkred) on DOY 151 in 2022.

Furthermore, the PCO and PCV errors were corrected using the antenna file igs14.atx. In summary, the other signal propagation errors such as the sagnac effect, phase wind-up, relativistic effects, tropospheric refraction, and slant ionospheric delays were accounted for as demonstrated in Chapter 3 (Section 3.5.3).

Before OSB experimental validation, the signal strengths for BDS and Galileo constellation were evaluated as in Strode and Groves (2016). The SNR ratio for all the available signals for the selected stations was estimated, and their averaged solutions over a period of one month (DOY 121-151, 2022) are compared in Figure 4.6.

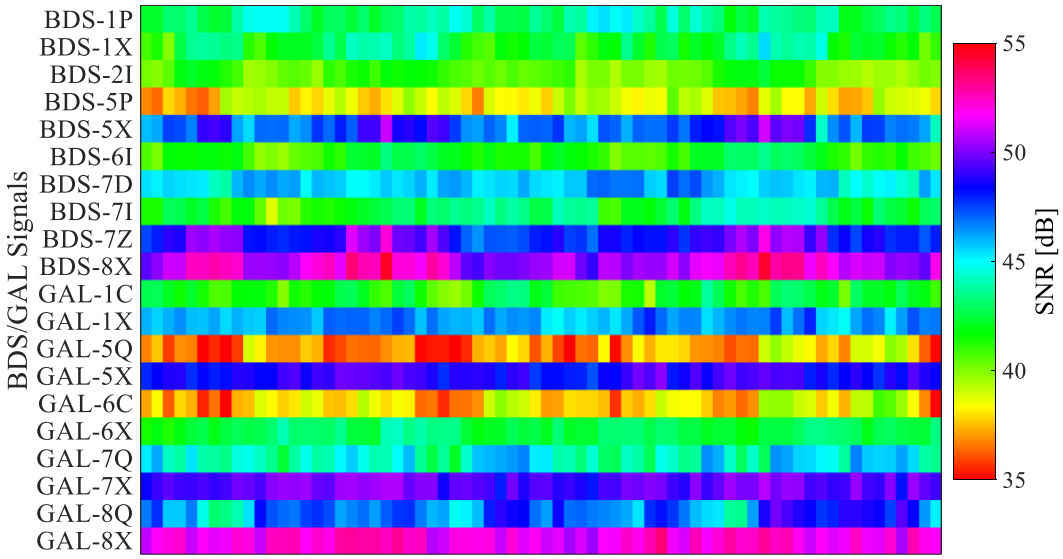

Figure 4.6: BDS and Galileo signal strength comparison for the selected days.

According to Strode and Groves (2016), a GNSS receiver should output a SNR of not less than 42 decibels (dB) in an ideal environment. From Figure 4.6, it can be observed that all the selected signals for the OSB tests are generally larger than the baseline limit of 42 dB for both BDS and Galileo except 5P for BDS, and 5Q and 6C for Galileo. In particular, for BDS the 5X (B2a), 7Z (B2b), and 8X (B2a+b) signals exhibit better signal strength than the other signals. Similarly, the Galileo constellation demonstrates stronger signal strength for 5X (E5a), 7X (E5b), and 8X (E5a+b) signals than the others. It is worth mentioning that, for both constellations, these signals are the modernised ones that are less susceptible to multipath effects and noise.

For example, Figure 4.7 and Figure 4.8 illustrate the SNR skyplots for the available signals at LEIJ station on DOY 121 in 2022 for BDS and Galileo, respectively. Despite that the signals mentioned above exhibit better signal strength, B1I (2*), B3I (6*), B1C (1*), and B2a for BDS-3 and E1 (1*), E5a, E5b, and E6 (6*) for Galileo were used for further analysis in this study because they can be tracked by more globally distributed stations (Figure 4.3).

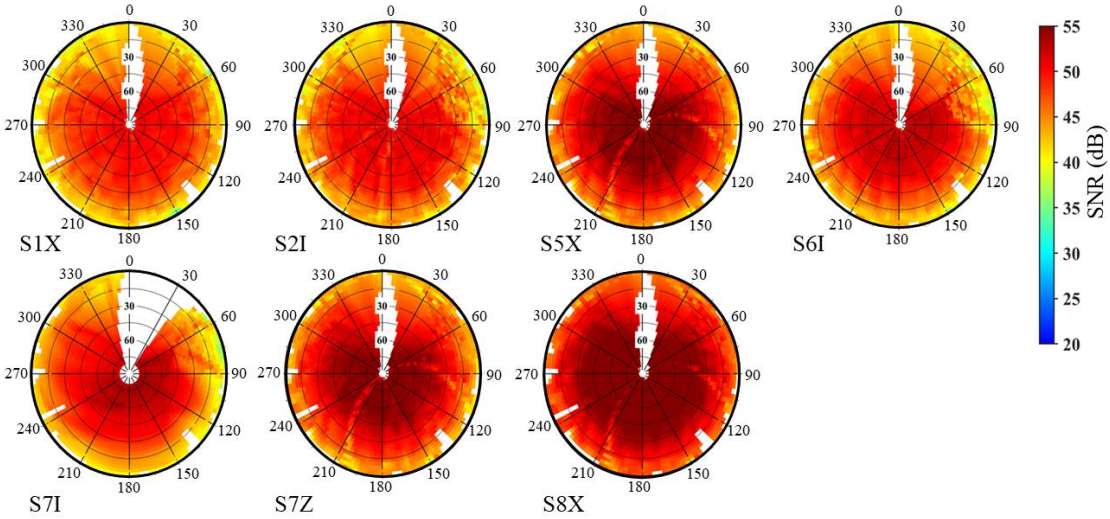

Figure 4.7: BDS SNR skyplots at LEIJ station on DOY 121 in 2022.

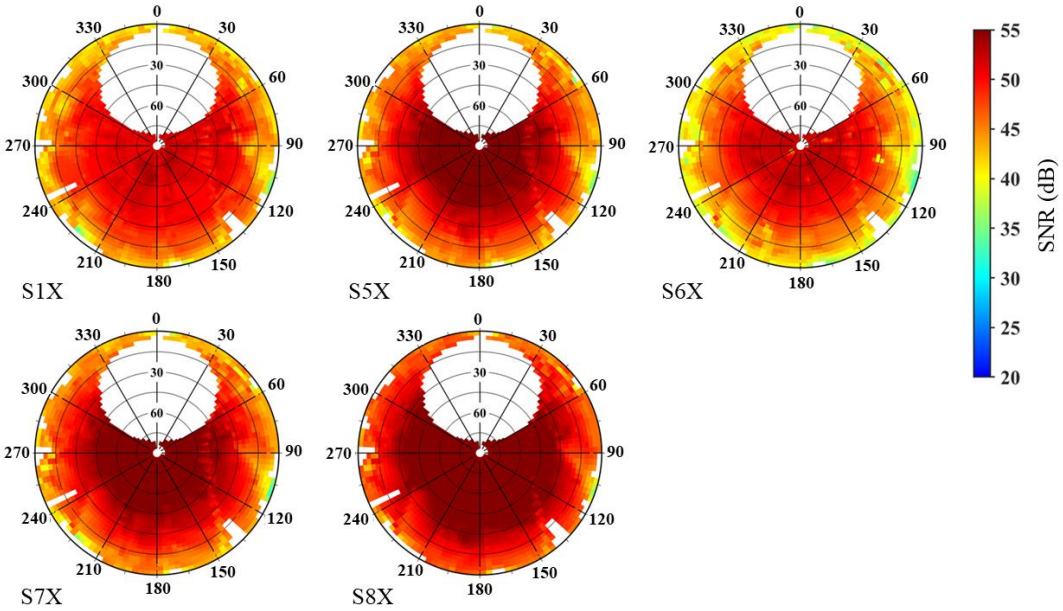

Figure 4.8: Galileo SNR skyplots at LEIJ station on DOY 121 in 2022.

4.5.2.1 Estimated Code OSB

The OSB for all the available BDS-3 signals were estimated for the period of 31 days (DOY 121 to 151, 2022). The evaluation of the code and phase OSB comprised receivers from different manufacturers, namely SEPT, LEICA, JAVAD, and TRIMBLE. Using the aforementioned receivers, the OSB for all the tracked satellites for both BDS-3 and Galileo constellations were estimated. The estimated code OSB for each satellite at these signals were averaged and their STD for the period of one month are depicted in Figure 4.9 and Figure 4.10.

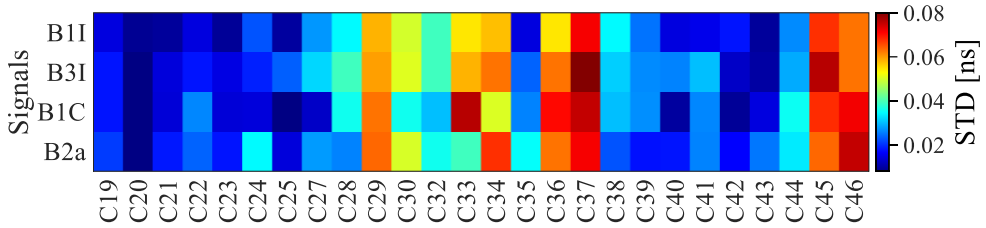

Figure 4.9: BDS-3 code OSB for different satellites.

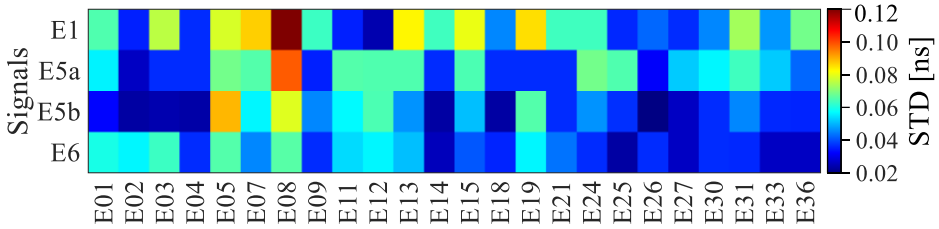

Figure 4.10: Galileo code OSB for different satellites.

Figures 4.9 and Figure 4.10 denote the averaged code OSB values for each satellite for a period of one month for BDS and Galileo, respectively. In both figures, the horizontal and vertical axes denote the PRN codes and signals, respectively. For example, the PRNs for BDS-3 range from C19 to C46 whereas those Galileo range from E01 to E36. In the case of signals, the BDS-3 frequency signals corresponding to the PRN are B1I, B3I, B1C, and B2a. As for Galileo constellation, the frequency signals mapped with respect to PRN are E1, E5a, E5b, and E6. Furthermore, the different colour codes denote the STD for the estimated code OSB for signals broadcast by BDS-3 and Galileo

constellations. Specifically, the different colour codes distinguish between the averaged code OSB for each satellite.

The BDS-3 B1C and B2a are interoperable with those of Galileo E1 and E5a, respectively. By recognising this compatibility, it can be seen from both figures that their estimated code OSB are slightly different, as the code OSB for BDS-3 signals vary between 0.02 and 0.08 ns (Figure 4.9), and those of Galileo signals range from 0.02 to 0.12 ns (Figure 4.10). This difference may be attributed to the disparity in modulation scheme for these signals. For instance, the B1C signal employs the QMBOC modulation technique, whereas the B2a and B2b signals apply the QPSK modulation scheme. In the case of Galileo, all the E5 signals are modulated with the Alternative Binary Offset Carrier (Alt-BOC) approach.

In addition to evaluating the code OSB for each individual satellite, the estimated code OSB were also assessed with respect to different types of geodetic receivers. To characterise the code OSB based on receiver hardware, the code OSB for SEPT, LEICA, JAVAD, and TRIMBLE receivers were estimated and presented in Figure 4.11. The panels labelled (a), (b), (c), and (d) compare the averaged code OSB for SEPT, LEICA, JAVAD, and TRIMBLE, respectively. Different types of receivers manufactured by SEPT are compared in panel (a), namely, POLARX5, POLARX5TR, ASTERX4, and POLARX5E. For the selected stations, results for a single type of receiver are presented for LEICA (GR50) and TRIMBLE (ALLOY) receivers in panels (b) and (d), respectively. In the case of JAVAD, two types of receivers are compared in (c), namely TRE 3 DELTA and TRE 3. As can be seen in (a) and (c), there is no significant difference between individual types of receivers.

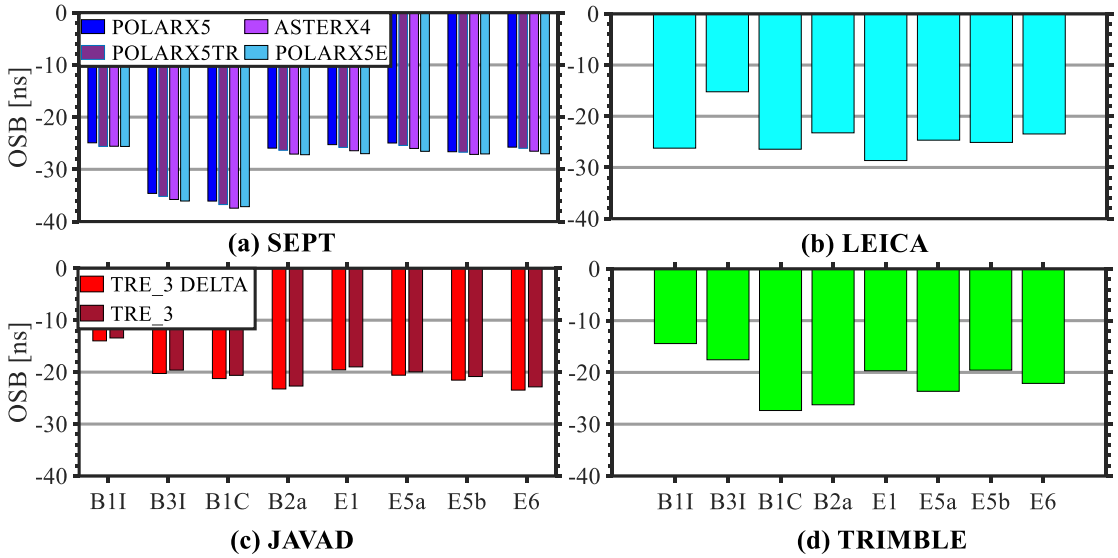

Figure 4.11: BDS and Galileo code OSB for different types of receivers.

An overall comparison of the estimated code OSB indicates that SEPT, LEICA, TRIMBLE, and JAVAD register significant differences. The same type of signal registers varying code OSB in different types of receivers. For example, the estimated code OSB on the B1I signal has a code OSB of about -25 ns in SEPT receivers and about -13 ns in JAVAD receivers. For the selected station, the estimated code OSB for BDS-3 at all the quad signals (B1I/B3I/B1C/B2a) exhibit an apparent variation. In contrast, there is generally no noticeable difference between the code OSB estimated from Galileo (E1/E5a/E5b/E6) quad-frequency signals using SEPT and JAVAD receivers. Overall, Galileo signals exhibit better code OSB than BDS-3 regardless of the type of receiver. Table 4.5 summarises the numerical statistics for the estimated code OSB for each individual type of receiver. As can be seen, in terms of STD, the code OSB at all the frequencies for both BDS-3 and Galileo constellations generally exhibit similar values for all the receivers.

Table 4.5: STD for code OSB for different types of receivers (Unit: ns).

	SEPT	LEICA	TRIMBLE	JAVAD
BDS-3	0.569	0.507	0.516	0.581
Galileo	0.591	0.571	0.648	0.599

4.5.2.2 Estimated Phase OSB

Unlike the code OSB, the phase OSB for each satellite were estimated and the results are shown in Figure 4.12. The top and bottom panels depict the characteristics of the BDS-3 and Galileo phase OSB, respectively. The different colours represent the STD for the phase OSB at distinct signals, and the numbers in parentheses are the mean STD of phase OSB for that particular frequency signal. As can be seen, the difference in the estimated phase OSB for different frequencies is small for both BDS-3 and Galileo constellations.

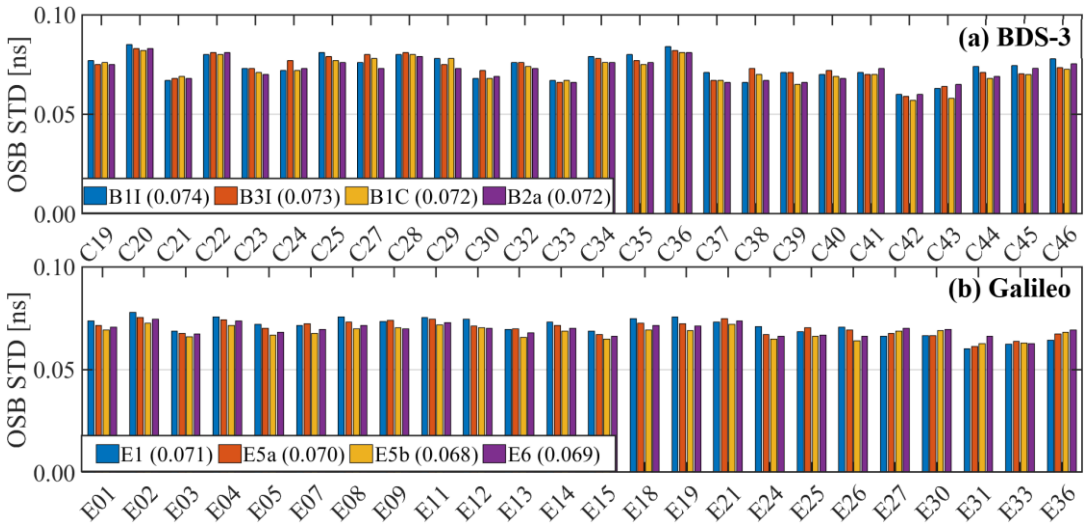

Figure 4.12: The estimated OSB for BDS-3 and Galileo constellations.

For example, the mean STD for B1I signal is 0.074 ns and is 0.073 ns on B3I signal. In the case of Galileo constellation, the mean STD on E1 signal is 0.071 ns and is 0.070 ns on E5a signal. There is generally a comparable stability in the phase OSB estimated at different frequencies for both constellations. Similarly, the mean STD for phase OSB at all the frequencies per type of receiver were estimated and are presented in Table 4.6. As can be noted in this table, the mean STD of phase OSB on each type of receiver are close to each other.

Table 4.6: STD for phase OSB for different types of receivers (Unit: ns).

	SEPT	LEICA	TRIMBLE	JAVAD
BDS-3	0.080	0.079	0.079	0.077
Galileo	0.078	0.077	0.080	0.073

4.5.3 Positioning Performance

The PPP tests were undertaken to verify the impact of the OSBs on position accuracy. By utilising the globally distributed stations for BDS and Galileo (Figure 4.3), the PPP performance in North, East, and Up components was evaluated over a period of one month. For each station, the position coordinates were computed with reference to the IGS weekly solutions. By using the two PPP processing schemes for BDS-3 and Galileo constellation, the positioning performance in North, East, and Up was evaluated in terms of the average, 25-percentile, 50-percentile, and 75-percentile for the period of one month.

Figure 4.13 summarises the positioning performance between BDS-3 and Galileo constellations using the dual-frequency (B1I/B3I and E1/E5a), triple-frequency (B1I/B3I/B1C and E1/E5a/E6), and quad-frequency (B1I/B3I/B1C/B2a and E1/E5a/E5b/E6) processing strategies. The observations for each satellite system were processed in both static (Figure 4.13a) and kinematic (Figure 4.13b) modes, with and without signal bias corrections. The results for the processing window of one month were analysed.

For BDS-3, processing schemes included B-DF, B-TF, and B-QF, where the suffixes denote dual-frequency, triple-frequency, and quad-frequency, respectively. Similar strategies were applied to the Galileo constellation. On the vertical axis of Figure 4.13, BDS-3 is denoted by the symbol ‘B’ (as defined in Chapter 3, Section 3.4) while the

Galileo constellation is represented by the symbol ‘E’. The statistical metrics, such as mean, 25th percentile (25%), 50th percentile (50%), and 75th percentile (75%), were used and are displayed on the x-axis for both panels. The colour-coded evaluation of each processing scheme is depicted in the figure, with the STD represented by the colour bar.

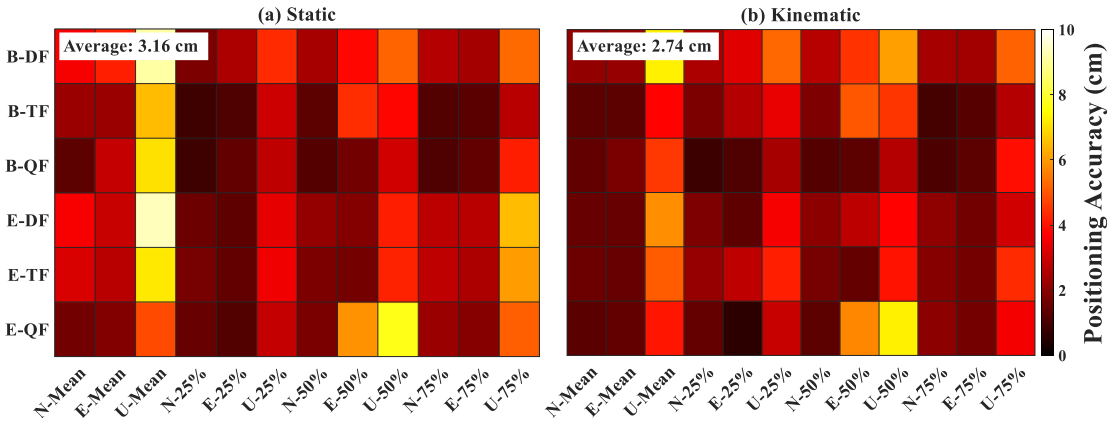

Figure 4.13: Comparison of BDS-3 and Galileo float PPP performance.

Across all strategies, it is evident that the North component consistently outperformed the others in all statistical measures. Generally, the float kinematic PPP demonstrated superior accuracy, achieving up to 2.7 cm, whereas the static mode achieved 3.2 cm.

In contrast to the float solution (Figure 4.13), the application of signal bias products noticeably enhances positioning accuracy in both static and kinematic processing schemes. This improvement is evident in Figure 4.14, where a discernible shift in colour intensity for the cells can be observed compared to Figure 4.13. Consequently, both static (Figure 4.14a) and kinematic (Figure 4.14b) PPP benefit significantly from the inclusion of code and phase bias products during data processing.

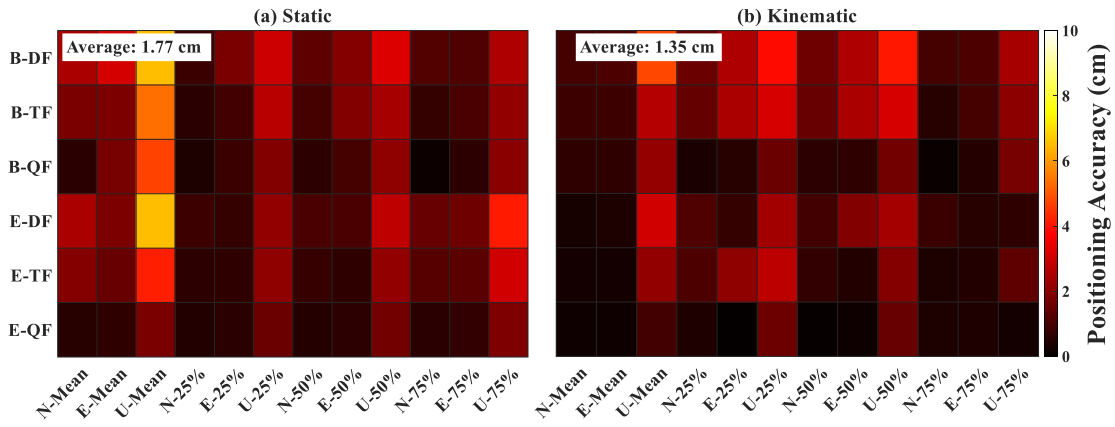

Figure 4.14: Comparison of BDS-3 and Galileo float PPP performance.

Additionally, while the QF PPP scheme outperforms the DF and TF schemes in both float and fixed solutions, its impact is more pronounced in the latter. Notably, the Galileo QF scheme demonstrated superior results compared to the BDS-3 QF scheme (Figure 4.14). Moreover, a comprehensive comparison of static and kinematic PPP across all frequency combinations indicates that the latter achieved considerably better results, averaging about 1.4 cm, compared to the former, which averaged about 1.8 cm.

To further elucidate the influence of signal biases on PPP, the enhancement in the three components (N, E, and U) was computed between the float and fixed solutions. Figure 4.15 depicts the improvement in static and kinematic fixed PPP relative to floating solutions.

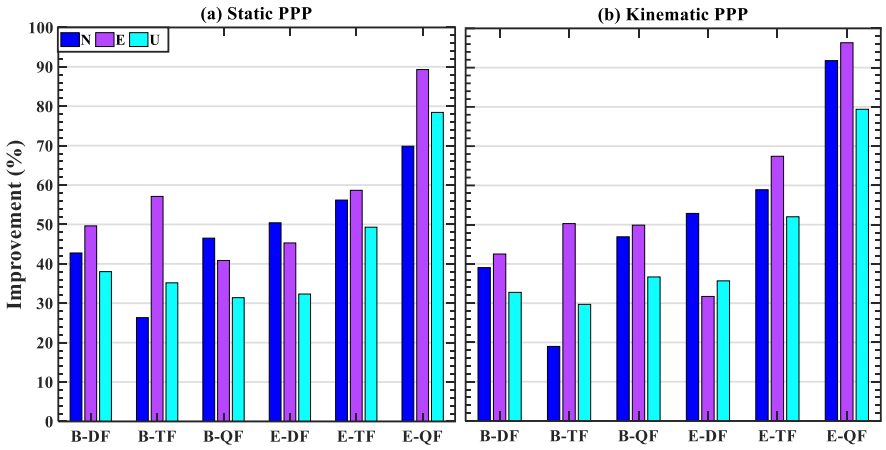

Figure 4.15: Improvement in static and kinematic positioning accuracy.

As discerned from this figure, the East component consistently outperforms the other components across all processing schemes, except in the B-QF and E-DF models in static PPP mode. Similarly, in kinematic PPP mode, the East component shows greater improvement compared to the other components, except for the case of E-DF. Regarding both static and kinematic modes, the performance of the East component typically surpasses that of the other components, in agreement with findings reported in the literature, for example, in Geng and Bock (2016). For both static and kinematic PPP, this form of improvement demonstrates a positive influence on signal bias correction. This means that the systematic errors introduced by satellites and receivers into the observables are mitigated by the bias corrections.

In addition to the comparison of positioning solutions, the fixing rates for NL and WL, as well as the convergence time, were also assessed. Both NL and WL play crucial roles in improving PPP-AR solutions in GNSS data processing. The NL provides high-precision phase measurements when successfully fixed, while WL contributes additional data for resolving carrier phase ambiguities. To evaluate the quality of ambiguity resolution for each constellation, static and kinematic PPP solutions were compared. Figure 4.16 illustrates the fixing rates for different processing schemes, revealing that both NL and WL fixing rates consistently exceed 80% in both static and kinematic modes.

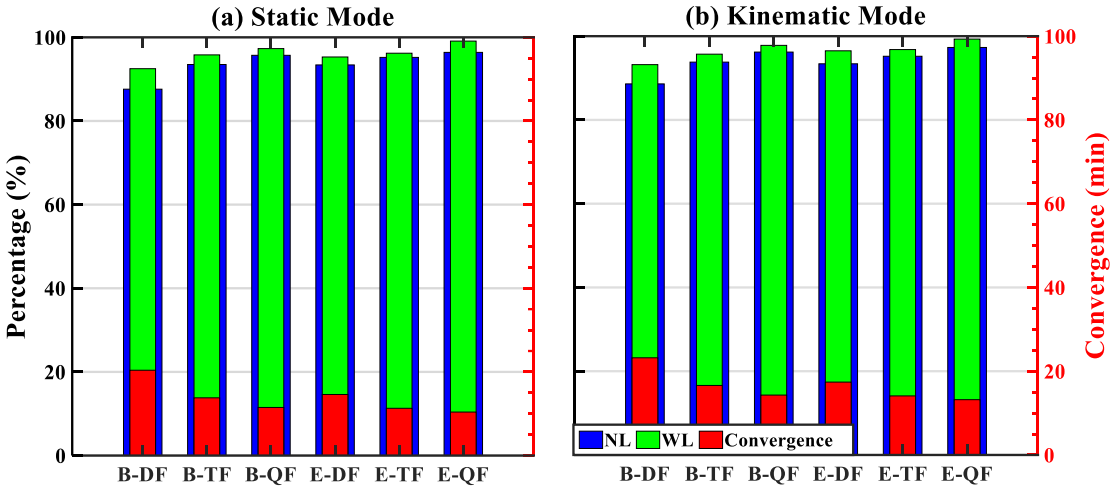

Figure 4.16: PPP-AR fixing rates and convergence time for different PPP schemes.

In both static and kinematic modes, the QF scheme consistently demonstrated superior performance, with Galileo consistently leading the way. In addition to fixing rates, the convergence time was also evaluated and is depicted in Figure 4.16 using red bins. A broad comparison reveals that the QF scheme achieves the best convergence time in the majority of static and kinematic PPP modes. The numerical statistics for convergence time and fixing rates are detailed in Table 5.

Table 4.7: Numerical statistics for fixing rates and convergence time.

	B-DF	B-TF	B-QF	E-DF	E-TF	E-QF	Remark
NL (%)	87.6	93.5	95.7	93.4	95.2	96.4	Static
WL (%)	92.5	95.8	97.3	95.3	96.2	99.1	Static
Convergence (min)	20.4	13.8	11.5	14.6	11.3	10.4	Static
NL (%)	88.6	93.8	96.2	93.4	95.2	97.3	Kinematic
WL (%)	93.2	95.7	97.8	96.5	96.8	99.3	Kinematic
Convergence (min)	23.2	16.6	14.3	17.4	14.1	13.2	Kinematic

Both Figure 4.16 and Table 4.7 highlight that the NL and WL fixing rates for QF PPP-AR in BDS-3 and Galileo are impressive, pegged at 97% and 99% in static mode,

respectively. Regarding convergence time, BDS-3 QF attained 12 and 14 minutes in static and kinematic modes, respectively. On the other hand, Galileo exhibits 10 and 13 minutes in static and kinematic modes, respectively. This indicates that the Galileo QF model required slightly fewer minutes to establish a reliable PPP solution.

Building upon the preceding discussion, enhancements in convergence time were computed and are detailed in Table 4.8 for both static and kinematic modes. In this table, B-TF/DF, B-QF/TF, and B-QF/DF denote the improvements in TF and QF convergence times for BDS in comparison to the DF and TF models. Similarly, E-TF/DF, E-QF/TF, and E-QF/DF indicate the TF and QF convergence time improvements for Galileo relative to the DF and TF models.

Table 4.8: Improvement in convergence time using different PPP schemes.

	B-TF/DF	B-QF/TF	B-QF/DF	E-TF/DF	E-QF/TF	E-QF/DF
Static (%)	48.0	20.2	78.0	29.2	9.1	40.9
Kinematic (%)	39.9	16.3	62.7	23.4	7.1	32.2

In static PPP mode (Table 4.8), BDS-3 exhibits improvements in convergence time of 48%, 20.2%, and 78%, while Galileo improves by 29.2%, 9.1%, and 40.9% across the same schemes. Notably, the improvement in convergence time for the BDS-3 quad-frequency scheme compared to the dual-frequency scheme is slightly higher at 78%. This suggests that the additional signal enhances convergence time for BDS-3 more than Galileo in the QF system.

In kinematic PPP mode, BDS-3 demonstrates improvements in convergence time of 39.9%, 16.3%, and 62.7%, while Galileo improves by 23.4%, 7.1%, and 32.2% across the same schemes. Consistent with the observations in static PPP mode, the BDS-3 QF processing scheme achieves the highest improvement of about 63% compared to the DF model. It is noteworthy to highlight that Galileo already achieves convergence times under 20 minutes across diverse processing filters. These results underscore the effectiveness of different processing schemes in enhancing convergence time.

4.5.4 Phase Residuals

The distinction between measured phase observations and the resolved integer number of cycles plays a pivotal role in categorizing the GNSS positioning solution. In the realm of phase observables, this discrepancy is termed the phase residual, and it is employed to evaluate the impact of OSB products on BDS-3/Galileo PPP-AR in this thesis.

Deploying a PPP test without signal bias corrections introduces systematic errors arising from clock biases. To validate this, the estimated phase residuals from selected stations over a one-month period (DOY 121-151, 2022) were averaged, and the results are depicted in Figure 4.17. The left panel (a) and right panel (b) compare the BDS-3 and Galileo phase residuals for different PRNs estimated without signal bias corrections. The various colour codes represent the averaged phase residuals over 31 days.

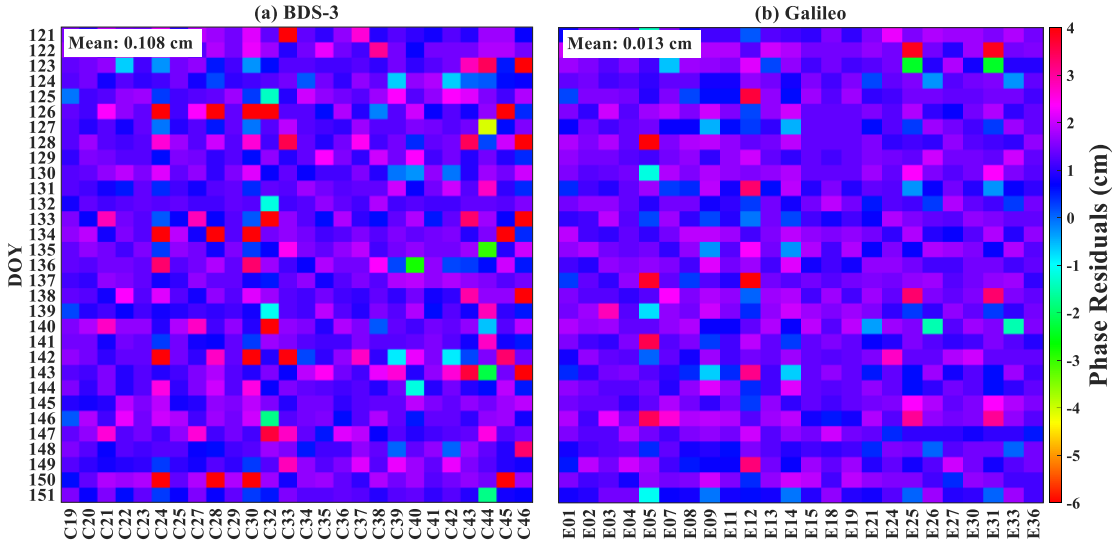

Figure 4.17: Phase residuals for BDS-3 and Galileo without OSB corrections.

As observed in Figure 4.17, the estimated phase residuals range from -6 to 4 cm for both BDS-3 and Galileo satellites. The statistical analysis over all days reveals that Galileo consistently achieved a smaller mean phase residual (approximately 0.031 cm) compared to BDS-3 (approximately 0.108 cm), indicating a relatively lesser impact on

the former. When conducting a similar test with OSB products, both BDS-3 and Galileo constellations demonstrated significant alterations in the estimated carrier phase residuals. Figure 4.18 illustrates the phase residuals for BDS-3 and Galileo with signal bias corrections.

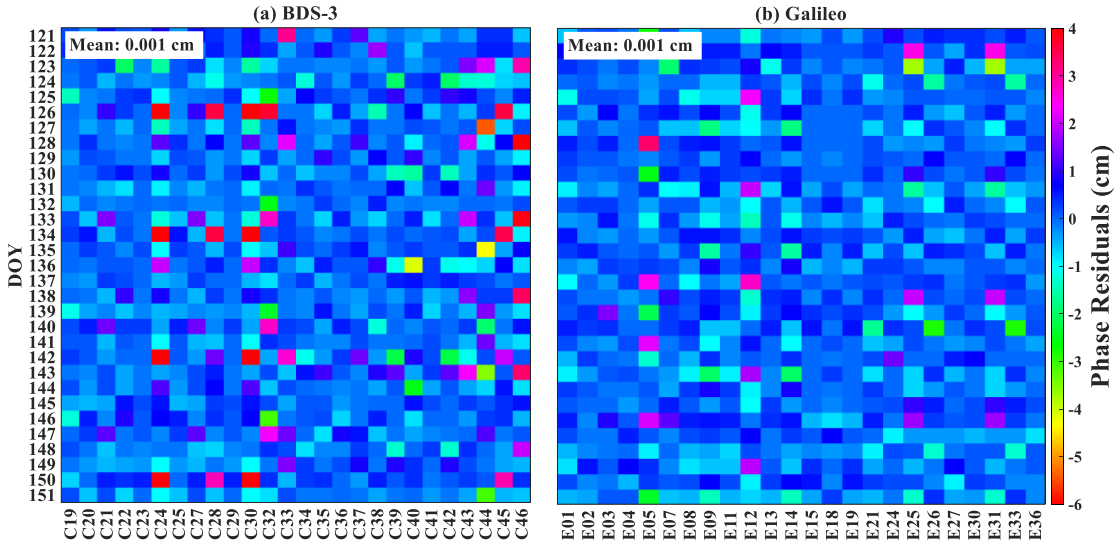

Figure 4.18: Phase residuals for BDS-3 and Galileo without OSB corrections.

This figure indicates a notable positive impact resulting from the application of signal biases in PPP, as the mean phase residuals in both constellations decrease to 0.001 cm (from 0.108 cm and 0.031 cm for BDS-3 and Galileo, respectively). Further statistical analysis reveals that BDS-3 and Galileo exhibited improvements of about 99% and 92%, respectively. This underscores a slightly superior performance in the former compared to the latter.

For illustrative purposes, the YEL2 station is employed to conduct a more in-depth evaluation of the phase residuals. Also known as YEL200CAN, YEL2 is a GNSS station situated at Latitude: 62.481°, Longitude: -114.481° in Yellowknife, Canada. This station is equipped with a SEPT POLARX5TR receiver and LEIAR25.R4 antenna, enabling it to track BDS and Galileo satellites in addition to GPS, GLONASS, and SBAS satellites. For demonstration purposes, the YEL2 station was selected to

compare the BDS-3 and Galileo phase residuals. Figures 4.19 and 4.20 show the phase residuals at the YEL2 station on DOY 140 in 2022 for BDS-3 and Galileo, respectively. In these figures, the horizontal axes represent time, and the vertical axes denote the time series for the estimated residuals for each PRN for BDS-3 and Galileo constellations. The estimated phase residuals are superimposed on the satellite tracks. The different colors represent the estimated phase residuals at different frequencies — B1I and B3I signals for BDS-3 (Figure 4.19) and E1 and E5a signals for Galileo (Figure 4.20).

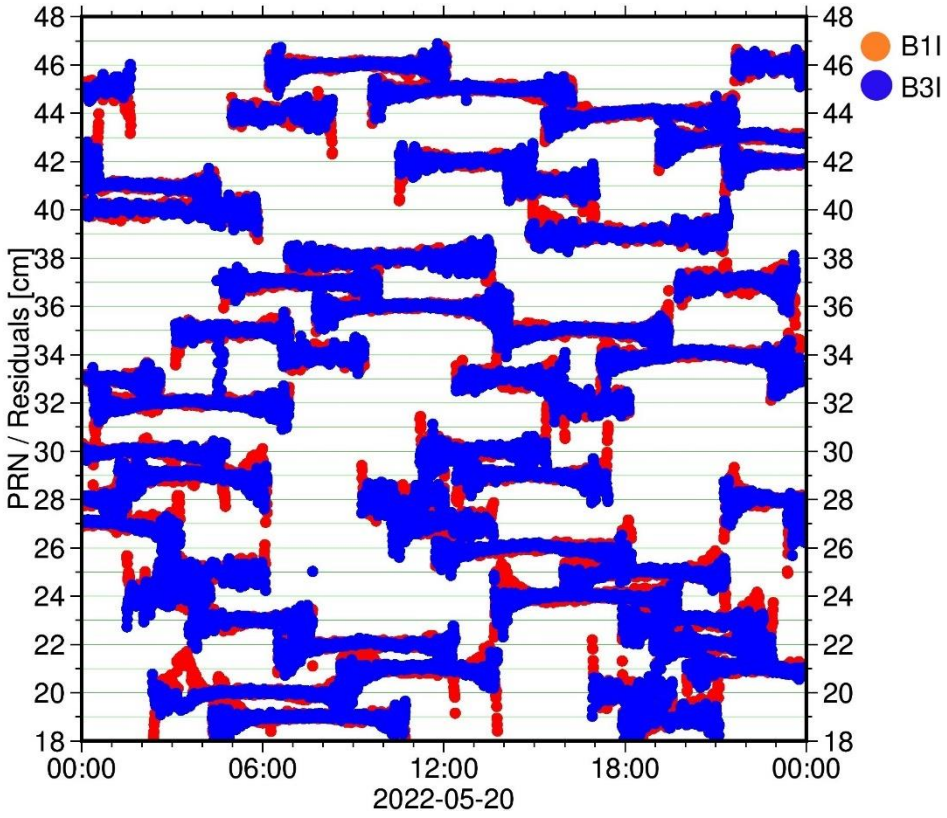

Figure 4.19: BDS-3 phase residual timeseries at YEL2 station on DOY 140, 2022.

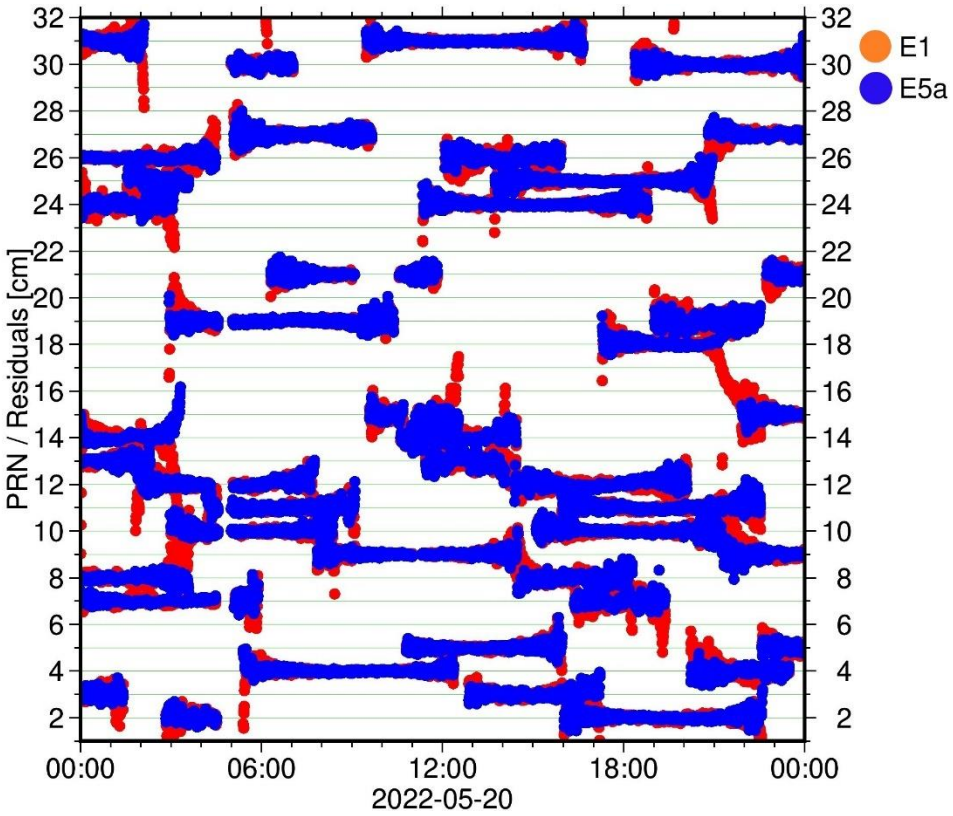

Figure 4.20: Galileo phase residual timeseries at YEL2 station on DOY 140, 2022.

In addition to the time series in Figures 4.19 and 4.20, Figure 4.21 illustrates the phase residuals for the same station on DOY 140 in 2022. This figure is a polar plot of phase residuals as a function of satellite azimuth and elevation angle. Despite differences in signals, BDS-3 and Galileo show comparable phase residuals in the range of -1 to 1 cm.

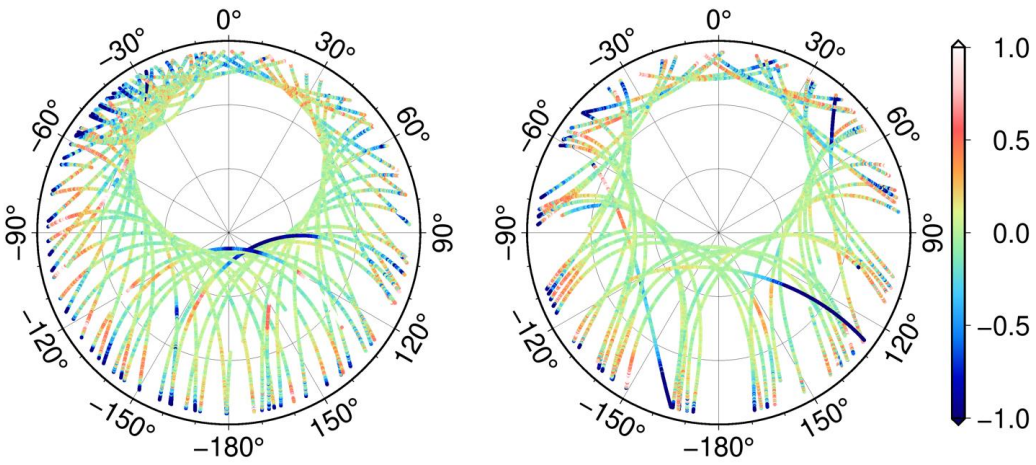

(a) BDS-3 (b) Galileo

Figure 4.21: Phase residuals for YEL2 station on DOY 140 in 2022 (Unit: cm).

4.6 Chapter Summary

This chapter investigated the hardware biases in the BDS constellation using both the legacy and the modernised signals. The traditional approach for estimating the biases is extended to quad-frequency signals. The theoretical equivalence in the mathematical models is investigated and numerical verification is conducted using a validation approach that is not currently clarified in the existing literature. Since Galileo satellites can also transmit multiple signals, similar tests were conducted for further validation. In general, this research unveiled that the modernised signals from both BDS-3 and Galileo are less affected by noise and multipath. The Galileo code OSB has no noticeable variation, while that of BDS-3 quad-frequency signals show significant variation. On the contrary, the phase OSB is similar for both constellations. Furthermore, bias corrections improve positioning in both constellations; however, BDS-3 is limited by the lack of quad-frequency tracking stations. Moreover, quad-frequency outperforms dual-frequency strategies in both constellations. The next chapter focuses on the satellite orientation and how it relates to biases in GNSS data processing.

Chapter 5: BDS Satellite Attitude Modelling in Data Processing

5.1 Introduction

The improper modelling of the orientation of satellites has an undesirable influence on high-precision GNSS. For instance, the biases emanating from that modelling propagate into satellite clocks. Eventually, this adversely limits the fixing of carrier phase ambiguities in GNSS data processing, leading to reduced positioning solutions. Coupled with the advent of OSB and the attitude quaternion, this chapter thoroughly establishes the potential effect of these products on PPP solutions. Specifically, the PPP functional model introduced in Chapter 3 is reparameterised to accommodate the BDS satellite attitude. Moreover, weighting schemes suitable for handling BDS satellites in three different orbits are proposed. Finally, numerical verification is undertaken to support the technique using raw datasets.

5.2 GNSS Satellite Orientation

GNSS satellites are powered by solar panels, and the panel is defined in the X-axis. This axis points to the direction of the sun. The Y-axis is defined parallel to the solar panel itself, whereas the Z-axis, typically the antennae axis, points to the Earth. According to Montenbruck et al. (2015), this kind of satellite orientation is the nominal attitude. An example of such orientation is given in Figure 2.3 (Chapter 2). While the satellite requires solar energy to keep itself in orbit, there is a problem when the angle with respect to the sun becomes close to zero. A couple of issues arise as this angle reduces; namely, the satellite finds it difficult to maneuver based on its own maximum yaw angles, and it loses its orientation to the sun. During this time, attitude errors emanating from the satellite propagate into the signals, which eventually degrades the PPP positioning solution.

Before the user employs the products from a given AC in PNT applications, the AC should make sure that it has applied the correct satellite attitude in the computation of the satellite position itself. To achieve this task, an accurate satellite attitude is necessary. Unfortunately, knowing the true satellite attitude has not been a common task in the GNSS community. Except Galileo and QZSS constellations whose satellite maneuvers are known for efficient application in the satellite positioning (Ishijima et al., 2009), the other navigation systems are yet to release theirs. Several attempts have been made for GPS Block II/IIA, IIR, and IIF have accurate attitude models, however, their models have limited yaw rate. This same issue is also true for the GLONASS modernised (GLONASS-M) satellites. Although these satellites systems have made such efforts to model satellite attitude, they are not discussed in this thesis. Similar to QZSS, the BDS-2 GEO satellites adopt the orbit normal mode (Dai et al., 2015; Montenbruck et al., 2015). On the other hand, according to Dilssner et al. (2018), the BDS-3 MEO and IGSO satellites employ the yaw steering (YS) mode.

The following subsections distinguish the satellite orientations used by BDS constellations.

5.2.1 Satellite Body-Fixed Reference Frame

The GNSS orbit information usually relates to the center-of-mass of the satellite, but the navigation signals are transmitted from an antenna at a different location. To quantify this disparity, a reference frame tied to the mechanical structure of the spacecraft is defined to specify the PCO and the PCV. Montenbruck et al. (2015) established a connection between the satellite body frame and the local orbital frame. Figure 5.1 shows three axes necessary in characterising satellite attitude.

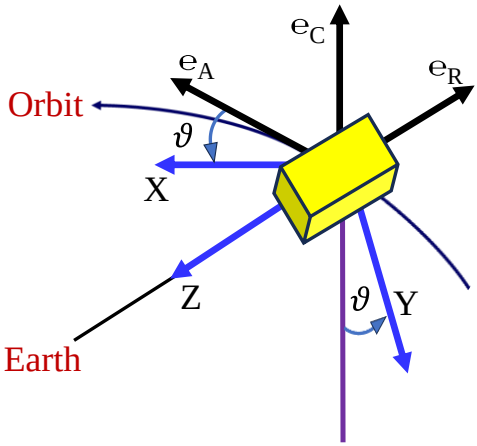

Figure 5.1: Specification of yaw angle.

The X-axis points in the direction of the Sun. This axis remains consistently exposed to the Sun during nominal yaw-steering. The rotation axis of the solar panels runs parallel to the Y-axis. The Z-axis corresponds to the direction of maximum beam intensity.

The local frame is defined by the vectors R, C, and A, representing the radial, cross-track, and along-track directions, respectively. When considering the geocentric position vector of the satellite and the velocity vector of geocentric satellite motion, the expressions for the radial, cross-track, and along-track unit vectors are as follows:

$$\begin{cases} \mathbf{e}_R = \dfrac{r}{|r|} \\ \mathbf{e}_C = \dfrac{rv}{|rv|} \\ \mathbf{e}_A = \mathbf{e}_C \mathbf{e}_R \end{cases} \tag{5.1}$$

where r and v denote the geocentric position vector and velocity vector, respectively. Furthermore, the satellite undergoes rotations, and the relationship between the X-axis and the corresponding rotation angles is expressed as follows:

$$X = R_X(roll) \cdot R_Y(pitch) \cdot R_Z(yaw) \cdot X_{RCA} \quad (5.2)$$

where R_X, R_Y and R_Z denote the rotation in X, Y, and Z, respectively. The rotation angles of roll, pitch, and yaw fascinates the transformation from one reference frame to another. Thus, the expression above (Equation 5.2) illustrates the transformation from the satellite body frame to the local frame.

5.2.2 Nominal Yaw Steering Mode

The typical orientation of a GNSS satellite is determined by fulfilling two criteria: the navigation antenna must face the centre of the Earth, and the solar array surface must face the Sun. To satisfy these requirements, the satellite needs to continuously turn around the Earth-pointing Z-axis, ensuring that the Y-axis aligns with the solar panel and stays perpendicular to the Sun direction.

The positive X-axis aligns with the hemisphere where the Sun is located and completes the orthogonal, right-handed coordinate frame. This concept is referred to as the nominal YS mode. An illustration exemplifying satellite maneuvering in YS mode is provided in Figure 2.3 (Chapter 2) and is provided in a simplified form below.

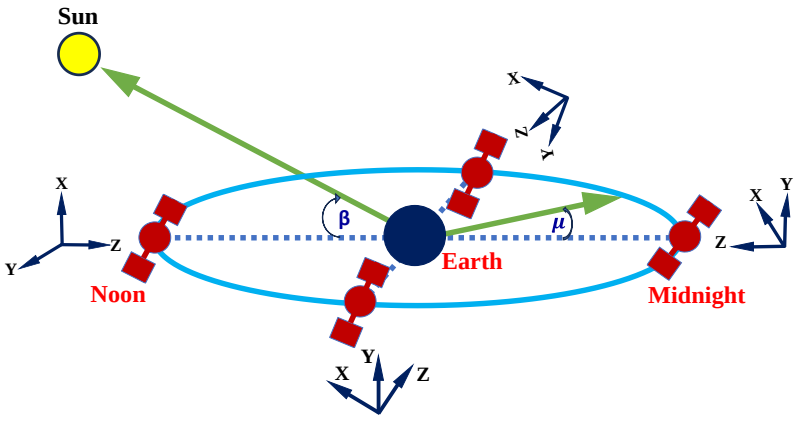

Figure 5.2: An example of yaw steering mode.

5.2.3 Orbit Normal Mode

As indicated by Montenbruck et al., (2015), the satellite attitude is aligned with the local orbital frame in the orbit normal mode. The X-axis points toward the velocity vector of the satellite. The Y-axis is oriented perpendicular to the orbital plane. The Z-axis points towards the center of the Earth.

In orbit-normal (OB) mode, the side facing away from the Sun changes on the satellite panels. The panels facing in different directions (+Z, +X, -Z) get illuminated one after the other. Similarly, either the +Y or -Y panel is always lit. These changes should be carefully taken into account when modelling radiation pressure, and they might pose a challenge for accurately determining the satellite orbit.

The switch from YS to OB mode occurs when the magnitude of $\|\beta\|$ (Figure 5.2) falls below a threshold, around 20° for QZS-1 and about 4° for BeiDou. As per Dai et al. (2015), the control center determines the exact moment of the mode switch (from YS to OB), which may vary slightly from the idealised values.

5.3 Advances in BDS Satellite Orientation Modelling

As indicated in Section 5.2, the BDS-2 MEO and IGSO satellites were originally configured to operate in YS mode. However, during prolonged periods of deep eclipse seasons, when these satellites frequently pass through Earth's shadow in each orbit, they seamlessly transition to the ON mode (refer to Section 5.2.3). Here, it is necessary to highlight that the solar angle, necessary in defining the eclipse session, is depicted in Figure 5.2 as the angle between the Z-axis and the solar unit vector. In mathematical terms, the solar unit vector can be expressed as

$$\overrightarrow{Sun} = [Sin\beta \;\; 0 \;\; Cos\beta] \tag{5.3}$$

Geometrically, the illustration of the Sun vector in the satellite fixed frame is shown in Figure 5.3.

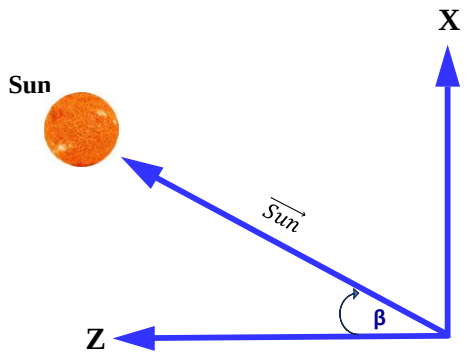

Figure 5.3: Geometry of the sun vector in the satellite fixed frame.

The eclipse season initiates when the solar angle β of the satellite falls below a designated threshold, approximately 13° for MEO and 8.5° for IGSO satellites. This adaptive shift serves to prevent abrupt yaw turns during the midnight and noon points

by modifying the attitude mode of the satellites. This data is crucial for preserving the stability of the satellite fixed coordinate system and accurately determining the solar vector. Beyond that, details like the solar angle (β) play a vital role in computing the solar radiation pressure, a key factor in orbit determination. Consequently, this information significantly assists ACs in comprehensively determining satellite orientation and calculating various satellite products.

Regardless of the efforts to accurately model the satellite attitude, different ACs apply unique techniques in the generation of satellite precise products. As indicated by Cao et al. (2018), the satellite attitude terms such as beta angle and the beginning and ending time for yaw maneuvers vary. This leads to an inconsistency between the solution achieved by the PPP user and the server side. As a way of combating this inconsistency, Loyer et al. (2021) suggested the use of attitude quaternions encoded in the ORBit EXchange (ORBEX) format. In their work, the impact of the satellite attitude quaternions generated by different AC was compared using GPS, GLONASS, and Galileo dual-frequency PPP. BDS constellation was not covered and being a new GNSS, it needs further investigation.

Since BDS supports multi-frequency signals, this thesis firstly extends the dual frequency model to quad- or more, and then parameterises it in terms of hardware biases and attitude quaternions. The following part (Section 5.4) concentrates on describing the satellite attitude through the use of quaternions.

5.4 Reparameterisation of Attitude Quaternions in PPP

An AC requires the satellite attitude information for different purposes such as for modelling PCO for the satellite antenna, and phase wind-up effect. In particular, the yaw satellite attitude errors are a sum of such effects. In order to explore the effect of the attitude errors on GNSS data processing, the yaw biases are incorporated in the PPP functional model. This follows that, in addition to the phase and code biases in the GNSS observations, the yaw biases are included to express the difference between the

true satellite attitude and the used attitude model. To estimate an accurate position in GNSS, all the biases in between the satellite and the receiver should be modelled or corrected. Hence, the PPP mathematical model in Equation (3.2) is reparameterised as

$$\begin{cases} \Phi_{fi}^{k} = \rho_{i}^{k} + c \cdot \left(\Delta t_i + \delta_{fi,\Phi} + \Delta\delta_{fi,\Phi}\right) - c \cdot \left(\Delta t^{k} + \delta_{f,\Phi}^{k} + \Delta\delta_{f,\Phi}^{k}\right) + \\ \qquad MF \cdot ZWD_{i}^{k} + \lambda_f N_{fi}^{k} + \vartheta_{i}^{k} + \epsilon_{fi}^{k} \\ P_{fi}^{k} = \rho_{i}^{k} + c \cdot \left(\Delta t_i + \delta_{fi,P} + \Delta\delta_{fi,P}\right) - c \cdot \left(\Delta t^{k} + \delta_{f,P}^{k} + \Delta\delta_{f,P}^{k}\right) + \\ \qquad MF \cdot ZWD_{i}^{k} + \vartheta_{i}^{k} + \varepsilon_{fi}^{k} \end{cases} \tag{5.4}$$

As indicated in the previous Chapters, the code and phase hardware biases on the receiver and satellite side are absorbed by the clocks for both the pseudorange and carrier phase observables. As for the carrier phase observable, the biases also lump with the ambiguity term. Therefore, in Equation (5.1), ϑ_{i}^{k} denotes the yaw bias which is simply the inconsistency between the true satellite attitude and the used attitude model. According to Loyer et al. (2021), this bias in the satellite attitude can be represented using a set of four quaternions (Q_n where n = 0 to 3) as

$$Q_n = Q_0 + Q_1 + Q_2 + Q_3 \tag{5.5}$$

Equation (5.5) can be split into a scalar and vector components as

$$\begin{cases} s = Q_0 \\ \vec{V} = [Q_1 \;\; Q_2 \;\; Q_3] \end{cases} \tag{5.6}$$

where s and $\vec{V}$ represent the scalar and vector parts, respectively. With such a framework, the quaternions provide a convenient means to represent 3D rotations using a concise four-element vector. This vector signifies a rotation of angle about an axis described by a unit vector. Hence, the expression presented in Equation (5.3) can also be rewritten as

$$Q_{rot,\vec{u}} = \left(cos\left(\frac{rot}{2}\right) \quad sin\left(\frac{rot}{2}\right).\vec{u}\right) \tag{5.7}$$

where rot denotes the rotation angle; $\vec{u}$ denotes the unit vector.

Since the quaternion can be expressed using scalar and vector components, setting the scalar to zero allows for the representation of a 3D vector in quaternion format. With the scalar component set to zero, the quaternion will be expressed as a vector in the quaternion format as

$$Q_{0,\vec{\varrho}} = (0 \quad \vec{\varrho}) \tag{5.8}$$

where $\vec{\varrho}$ denotes the 3D vector. Therefore, to define the errors due to improper satellite attitude modelling, the 3D expression of the body frame of the satellite is used. The unit vector in 3D can be expressed as

$$\varrho_{3D} = (\varrho_x, \varrho_y, \varrho_z) \tag{5.9}$$

In the realm of GNSS satellite orientation, quaternions serve to describe the conversion between the ECEF frame and the satellite-body frame. As indicated by Montenbruck et al. (2015), the relationship between the ECEF and satellite coordinate systems can be established through a rotation matrix (R) defined by the unit vectors in the satellite-body frame.

Therefore, the yaw angle (ϑ_i^k) refers to the angle formed between ϱ_x and the direction of motion of the satellite in orbit. Therefore, the parameterisation of the unit vectors in the satellite-body frame can be expressed as follows:

$$\varrho_x = \begin{bmatrix} Q_0^2 + Q_1^2 - Q_2^2 - Q_3^2 \\ 2(Q_1Q_2 - Q_0Q_3) \\ 2(Q_1Q_3 + Q_0Q_2) \end{bmatrix}$$
$$\varrho_y = \begin{bmatrix} 2(Q_1Q_2 + Q_0Q_3) \\ Q_0^2 - Q_1^2 + Q_2^2 - Q_3^2 \\ 2(Q_2Q_3 - Q_0Q_1) \end{bmatrix} \quad (5.10)$$
$$\varrho_z = \begin{bmatrix} 2(Q_1Q_3 - Q_0Q_2) \\ 2(Q_2Q_3 + Q_0Q_1) \\ Q_0^2 - Q_1^2 - Q_2^2 + Q_3^2 \end{bmatrix}$$

with

$$\begin{cases} Q_0 = 0.5\left(\sqrt{1 + \left(R_{(1,1)} + R_{(2,2)} + R_{(3,3)}\right)}\right) \\ Q_1 = \left(R_{(3,2)} - R_{(2,3)}\right)\left(\dfrac{1}{2\sqrt{1 + \left(R_{(1,1)} + R_{(2,2)} + R_{(3,3)}\right)}}\right) \\ Q_2 = \left(R_{(1,3)} - R_{(3,1)}\right)\left(\dfrac{1}{2\sqrt{1 + \left(R_{(1,1)} + R_{(2,2)} + R_{(3,3)}\right)}}\right) \\ Q_3 = \left(R_{(2,1)} - R_{(1,2)}\right)\left(\dfrac{1}{2\sqrt{1 + \left(R_{(1,1)} + R_{(2,2)} + R_{(3,3)}\right)}}\right) \end{cases}$$

In the provided expression, Equation (5.7), R signifies the rotation matrix that establishes the relationship between the ECEF and satellite coordinate systems. These unit vectors play a crucial role in defining the satellite attitude, which is essential for computing both the phase center positions and the satellite wind-up correction at the user end.

In the process of calculating a PPP solution, it is imperative for the user to employ the identical attitude model utilised in the computation of the satellite products. Failure to do so can lead to inaccuracies in modelling error sources such as satellite phase center corrections and phase wind-up effects. These error sources significantly impact the precision of phase observations and consequently affect the ambiguity fixing process (refer to Section 5.4). The subsequent subsections elaborate on the parameterisation of biases relative to satellite orientation.

5.4.1 Formulation of Biases on the Network Side

As demonstrated in Chapter 4, the biases in a multi-frequency PPP scenario can be derived after applying the MGEX precise products. Thus, after applying such products, the biases lump with the ambiguity parameters, and this makes the ambiguities lose their integer properties. As observed in the aforementioned chapter, after applying the products, all the hardware biases are compensated except the time-variant biases on the third frequency. Therefore, the time-variant biases on the third frequency and the systematic biases as a result of the yaw attitude combine with the phase observation residuals as

$$\hat{\epsilon}_{\Phi j}^{k} = \epsilon_{i,j}^{k} + \vartheta_{i,j}^{k} \tag{5.11}$$

where $\hat{\epsilon}_{\Phi j}^{k}$ denotes the phase observation residual that has combined with random errors and the satellite attitude biases on j frequency. For instance, the equations can be formulated for the quad-frequency observation using the BDS constellation.

$$\begin{aligned} \hat{\epsilon}_{\Phi 1}^{k} &= \epsilon_{i,1}^{k} + \vartheta_{i,1}^{k} \\ \hat{\epsilon}_{\Phi 2}^{k} &= \epsilon_{i,2}^{k} + \vartheta_{i,2}^{k} \\ \hat{\epsilon}_{\Phi 7}^{k} &= \epsilon_{i,7}^{k} + \vartheta_{i,7}^{k} \\ \hat{\epsilon}_{\Phi 6}^{k} &= \epsilon_{i,6}^{k} + \vartheta_{i,6}^{k} \end{aligned} \tag{5.12}$$

where 1, 2, 7, and 6 denote B1C, B1I, B2I, and B3I, respectively.

5.4.2 Formulation of Biases on the PPP User

Taking BDS precise products as an example, the biases can be estimated using BDS precise products. As indicated in Chapter 3, the satellite clocks for BDS can be obtained from the IF combination using B1I and B3I frequency signals. For instance, using the MGEX precise products such as WUM products, it will be

$$\Delta\hat{t}_{i,WUM}^{k} = c \cdot \Delta t_i + \delta_{IF,i}^{k} + \Delta\delta_{IF,i}^{k} \tag{5.13}$$

Taking WUM precise products, for example, the satellite attitude inconsistency above will lump with the integer phase delay as

$$\begin{aligned}\Delta\hat{t}_{i,CLK}^{k} &= \hat{t}^{k} + \left(\gamma_2\lambda_1\delta_{\Phi 1}^{k} - \lambda_2\delta_{\Phi 2}^{k}\right)/(\gamma_2 - 1) + \\ &\quad \left(\gamma_2\vartheta_{1,WUM}^{k} - \vartheta_{2,WUM}^{k}\right)/(\gamma_2 - 1)\end{aligned} \tag{5.14}$$

with

$$\vartheta_{f,Product}^{k} = \gamma_2\vartheta_{1,WUM}^{k} - \vartheta_{2,WUM}^{k}$$

Due to linear dependency, it is hard to estimate the multi-frequency hardware biases using the WUM precise products directly. To overcome the rank deficiency, the biases are estimated using the triple-frequency IF carrier phase observables, for example $\Phi_{r,IF3}^{k}$ as demonstrated in Section 4.4.2 (Chapter 4). In this case, the variable phase biases and the satellite attitude errors lump with the ambiguity parameters. For instance,

taking BDS triple-frequency signals such as B1I/B2I/B3I, the new ambiguity terms that have absorbed the biases can be expressed as:

$$\left.\begin{aligned}\widehat{N}_{12}^{k} &= N_{12}^{k} + \frac{\left(\gamma_2\delta_{P1}^{k} - \delta_{P2}^{k}\right)}{\lambda_{12}(\gamma_2 - 1)} - \vartheta_{12,WUM}^{k} - \delta_{\Phi 12}^{k} \\ \widehat{N}_{23}^{k} &= N_{23}^{k} + \frac{\left(\gamma_2\delta_{P1}^{k} - \delta_{P2}^{k}\right)}{\lambda_{23}(\gamma_2 - 1)} - \vartheta_{23,WUM}^{k} - \delta_{\Phi 23}^{k}\end{aligned}\right\} \tag{5.15}$$

with

$$\begin{cases}\vartheta_{12,WUM}^{k} = \dfrac{\vartheta_{1,WUM}^{k}}{\lambda_1} + \dfrac{\vartheta_{2,WUM}^{k}}{\lambda_2} \\ \vartheta_{23,WUM}^{k} = \dfrac{\vartheta_{2,WUM}^{k}}{\lambda_2} + \dfrac{\vartheta_{3,WUM}^{k}}{\lambda_3} \\ \delta_{\Phi 12}^{k} = \delta_{\Phi 1}^{k} + \delta_{\Phi 2}^{k} \\ \delta_{\Phi 23}^{k} = \delta_{\Phi 2}^{k} + \delta_{\Phi 3}^{k} + \Delta\delta_{\Phi 3}^{k}\end{cases}$$

where $\widehat{N}_{12}^{k}$ and $\widehat{N}_{23}^{k}$ denote the float ambiguity parameters on B1I/B2I and B2I/B3I frequency signals, respectively. These float ambiguity terms have lumped with the biases emanating from the satellite attitude and the hardware biases; $\vartheta_{12,WUM}^{k}$ and $\vartheta_{23,WUM}^{k}$ denote the satellite yaw attitude errors corresponding to B1I/B2I and B2I/B3I frequency signals, respectively; $\delta_{\Phi 12}^{k}$ and $\delta_{\Phi 23}^{k}$ denote phase biases on B1I/B2I and B2I/B3I, respectively. Here, $\Delta\delta_{\Phi 3}^{k}$ is the carrier phase time-dependent bias on the third frequency. According to Geng et al. (2010), these biases can be extracted as fractional components through integer rounding. Hence, generalising the above combination to any triple-frequency combination, the phase biases can be expressed as

$$\left.\begin{aligned}\hat{\delta}_{\Phi 1}^{k} &= \frac{\delta_{P}^{k}}{\lambda_{1}} - \delta_{\Phi 1}^{k} - \frac{\vartheta_{1,WUM}^{k}}{\lambda_{1}} \\ \hat{\delta}_{\Phi 2}^{k} &= \frac{\delta_{P}^{k}}{\lambda_{2}} - \delta_{\Phi 2}^{k} - \frac{\vartheta_{2,WUM}^{k}}{\lambda_{2}} \\ \hat{\delta}_{\Phi j}^{k} &= \frac{\delta_{P}^{k}}{\lambda_{j}} - \delta_{\Phi j}^{k} - \frac{\vartheta_{j,WUM}^{k}}{\lambda_{j}} - \Delta\delta_{\Phi j}^{k}\end{aligned}\right\} \tag{5.16}$$

After applying the code OSB corrections, the code biases can be described as

$$\left.\begin{aligned}\hat{\delta}_{P1}^{k} &= \beta_{12}\left(\delta_{P1}^{k} - \delta_{P2}^{k}\right) \\ \hat{\delta}_{P2}^{k} &= \alpha_{12}\left(-\delta_{P1}^{k} + \delta_{P2}^{k}\right) \\ \hat{\delta}_{Pj}^{k} &= \delta_{P}^{k} - \delta_{Pj}^{k}\end{aligned}\right\} \tag{5.17}$$

Therefore, the PPP user can apply the phase and code biases to recover the ambiguities. In addition to recovering the ambiguities, this bias treatment also mitigates the yaw satellite attitude errors and the time-variant hardware bias on the third frequency. This means that ambiguities and the phase residuals at any frequency can be formulated as

$$\begin{cases}\widehat{N}_{j}^{k} = N_{j}^{k} + \delta_{\Phi j} - \delta_{Pj} + \lambda_{j}\beta_{12}\left(\delta_{P1}^{k} - \delta_{P2}^{k}\right) \\ \hat{\epsilon}_{f}^{k} = \epsilon_{f}^{k}\end{cases} \tag{5.18}$$

For example, the residual vector for the multi-frequency combination involving signals such as B1C, B1I, B2I, and B3I can be expressed as

$$\hat{\epsilon}_{f}^{k} = [\epsilon_{1}^{k}, \epsilon_{2}^{k}, \epsilon_{7}^{k}, \epsilon_{6}^{k}]^{T} \tag{5.19}$$

where ϵ_{1}^{k}, ϵ_{2}^{k}, ϵ_{7}^{k}, and ϵ_{6}^{k} denote the phase residuals on B1C, B1I, B2I, and B3I, respectively. The estimated carrier phase residuals, including the influence of the phase

biases on the satellite maneuver, are discussed in Section 5.6 which particularly highlights the validation approach used to test the proposed technique.

The processing observations in a multi-GNSS scenario necessitates appropriate stochastic modelling. The forthcoming section will explore the stochastic modelling specifically tailored for combined data processing of BDS and Galileo.

5.5 Stochastic Modelling and Data Refining

In the domain of GNSS data processing, stochastic modeling significantly influences various stages, impacting parameter optimisation and the reliability of solutions. Stochastic modelling is essential for gauging the quality of estimated parameters by representing and measuring the uncertainties in GNSS observations. The subsequent subsections elaborate on the stochastic models proposed in this thesis. Additionally, criteria for managing GNSS data, aimed at excluding unnecessary observations that may introduce imperfections and discontinuities in the estimated parameters, are put forth.

5.5.1 Stochastic Modelling

Quantifying errors and uncertainties in GNSS relies on the quality of satellite observations and the capabilities of the receiver. The receivers equipped with different hardware and software configurations have unique capabilities for tracking GNSS signals. Consequently, uncertainties in GNSS observations depend on factors like the SNR, satellite cutoff angle, and quality of satellite precise products.

Considering that BDS encompasses satellites in diverse orbits, this thesis accounts for variations in orbit quality. GEO satellites exhibit slightly lower quality than IGSO and MEO satellites. Therefore, distinct weights are assigned to these sets of satellites in the processing filter. The IGSO and MEO satellites receive a weight of 1, while GEO

satellites are assigned a weight of 4, as determined in Equation 3.6 (refer to Section 3.5.3, Chapter 3).

For processing BDS and Galileo datasets, the GNSS weighting is employed alongside elevation-dependent weighting. Both BDS-3 and Galileo are assigned equal weights of 1 under GNSS weighting. Therefore, the variance after incorporating elevation and GNSS weighting is formulated as follows:

$$\begin{cases} \sigma_m^2 = \dfrac{\sigma_{m,0}^2}{Sin^2(E)}(w_{GNSS}) \\ \quad = \dfrac{\sigma_{m,0}^2}{Sin^2(E)} \end{cases} \tag{5.14}$$

Here, σ_m^2 represents the variance, and m denotes the measurement, while $\sigma_{m,0}^2$ signifies the variance of the raw measurement. By acknowledging that phase observations typically exhibit higher precision than code observations, this thesis adopts distinct precisions for each, as detailed in Section 3.5.3 of Chapter 3. Notably, the STDs ($\sigma_{m,0}$) for the measurements are set at 3 mm and 300 mm for phase and code observations, respectively. The term w_{GNSS} represents the GNSS weighing factor.

5.5.2 Data Refining

Satellites in proximity to the horizon receive lower weighting compared to those near the zenith, adjusting the standard deviation of observations accordingly. This practice is grounded in the observation that residuals of geodetic receivers are generally correlated with the elevation angle, as illustrated in Chapter 3, Figures 3.13 and 3.14. Hence, an elevation mask of 7° is introduced to exclude satellites very close to the horizon, in conjunction with a weighting system based on satellite elevation. Moreover, observations exhibiting a low SNR are excluded.

Furthermore, the exclusion criteria extend to observations devoid of precise orbit or clock information, as well as satellites presenting missing code biases. Notably, the removal of satellites lacking phase biases is specifically reserved for the ambiguity-fixing process. Typically, instances of data gaps or invalid information manifest more frequently in real-time correction streams than in post-processed satellite products.

5.6 Model Validation using MGEX Datasets

To validate the proposed method described above, the MGEX datasets with BDS tracking capability were used. Specifically, 30 seconds observations were employed at both the network and the PPP user sides. On the network side, the test comprises the estimation of clocks necessary for the PPP user. Firstly, these products were generated using the traditional approach that utilises the nominal attitude. Secondly, they were also generated using attitude quaternions. The two approaches were employed to investigate the influence of satellite attitude modelling on the clock products. The underlying justification is that the biases lump with the satellite clocks (as already shown in the previous Chapters). Furthermore, the impact of the proposed model is also verified using the observation residuals through PPP experiments. Figure 5.4 shows the geographic locations of MGEX stations that support BDS signal frequencies.

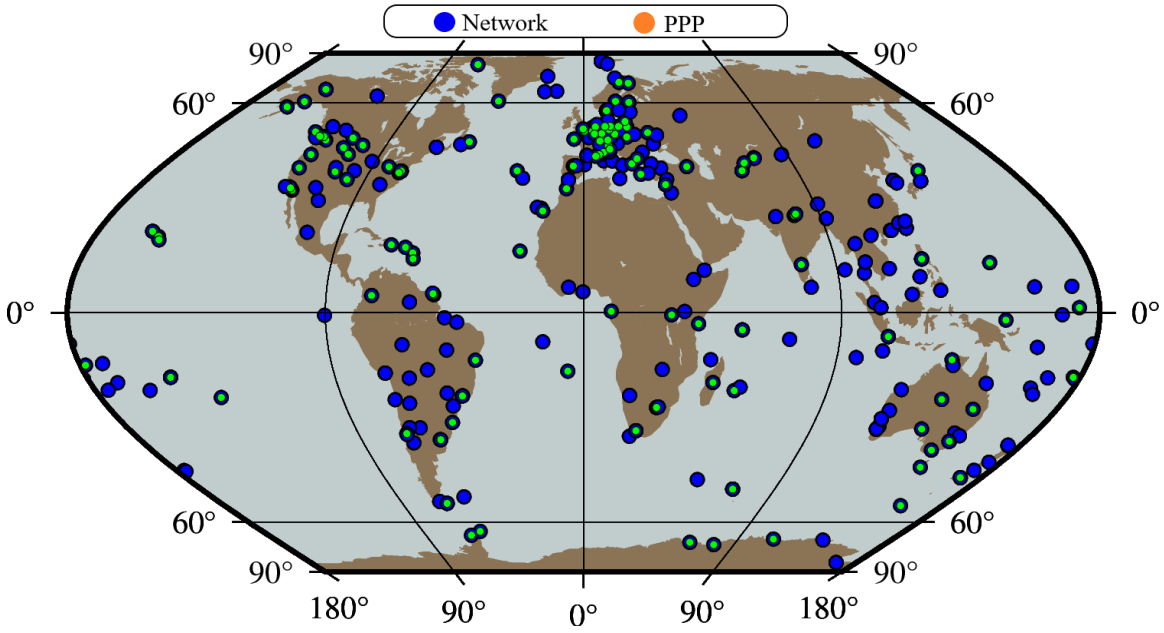

Figure 5.4: Distribution of BDS tracking stations.

The blue stations (326) were used for the generation of clocks, whereas those spotted with green colour (134) were used for PPP tests for the dataset window spanning from DOY 091 to 120 in 2022 (i.e:, 1st — 30th April, 2022). The errors due to the ocean tidal loading, solid earth tides, and pole tides were corrected using similar models as those applied in Chapters 3 and 4. The biases that lumped with the phase ambiguities carrier were resolved using the integer rounding approach. Using this multi-session adjustment technique, the epochs with a limited number of satellites (such as < 4) were discarded. In addition, due to poor orbits, the BDS GEO satellites were excluded from the ambiguity resolution tests. Figure 5.5 shows the BDS-2 (blue) and BDS-3 (red) satellite tracks on DOY 110 in 2022 computed using WUM orbit products. In this figure, the short blue patches illustrate the locations of the BDS-2 GEO satellites in orbit.

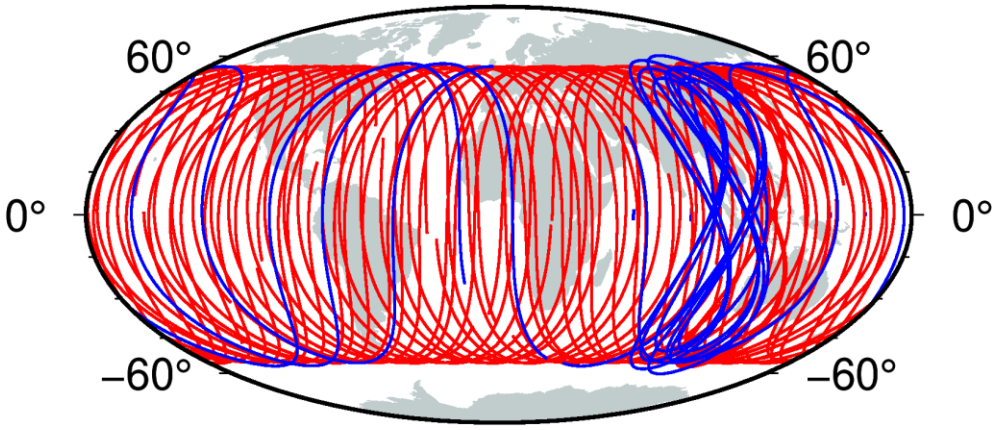

Figure 5.5: BDS-2 and BDS-3 satellite tracks on DOY 110 in 2022.

5.6.1 Considering Attitude Quaternions in GNSS Data Processing

As already mentioned, the processing strategy comprises the nominal and attitude quaternions schemes. Here, both constellations that can broadcast quad- or more frequency signals were considered in the validation following the batches of modernised satellites. Therefore, the tests were undertaken using BDS and Galileo constellations. Using WUM products, two data processing schemes were employed to thoroughly examine the proposed method, namely using

- nominal attitude, and
- satellite attitude quaternions.

In using the nominal mode simply means processing the data by taking the orientation of the satellite axes aligned with the local orbital reference as described in Section 5.2. In this case, the assumption is that the satellite orientation is constant throughout the observation period. Alternatively, it may generally mean that the satellite maneuvers are negligible during the GNSS data processing. Technically, it may also mean that the data processing is deficient in the precise satellite attitude dataset necessary for

identifying periods when the satellite is in shadow during some hours of the day (for example, when the solar panel is not pointing in the direction of the sun). On the other hand, the use of satellite attitude quaternions implies that the actual variations in a satellite orientation are captured to obtain reliable temporal variations. Hence, the estimation approach proposed in this Chapter is used to better understand the effect of satellite geometry on the positioning solution and observation residuals. The implementation explained here is illustrated in the schematic diagram (Figure 5.6) below.

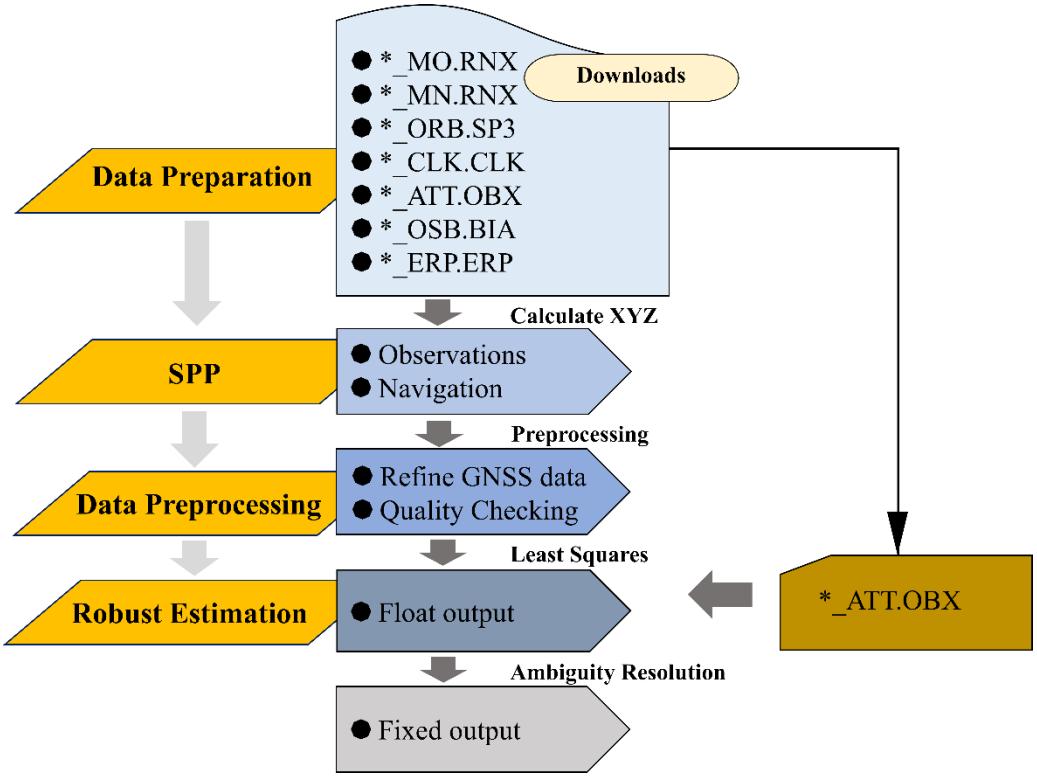

Figure 5.6: Data processing workflow.

The data processing module starts with the data preparation stage where the necessary MGEX data are automatically downloaded to the processing directory. As part of this processing workflow, a Python module was developed to enhance the management and organisation of GNSS datasets. By leveraging multithreading capabilities in Python language, this module facilitates the recursive download of the required datasets during

the preparation stage, simplifying the overall data management process. For example, the downloaded datasets include the observations (*_MO.RNX), navigation files (*_MN.RNX), orbits (*_ORB.SP3), clocks (*_CLK.CLK), attitude quaternions (*_ATT.OBX), biases (*_OSB.BIA), and rotation parameters (*_ERP.ERP). The characters shown in the parentheses are simply the file extensions distinguishing them. After data preparation, the single point positioning (SPP) program is used to compute the initial coordinates for the station. Then, preprocessing is invoked to diagnose the datasets for errors before the robust estimation. The estimator computes the least squares solution: float or fixed. In this implementation, all the necessary products (orbits, clocks, biases, and earth orientation parameters) are applied in data processing apart from the quaternion products to generate the float solution. On the contrary, the fixed solution applies all the products including the quaternions. However, for the sake of comparison, the float and fixed strategies were also conducted using different frequency combinations. Table 5.1 depicts the PPP processing schemes. In this table, D-F, T-F, and Q-F are the dual-frequency, triple-frequency, and quad-frequency processing schemes, respectively. The testing frequencies are shown in last column of this table.

Table 5.1: PPP processing strategies for validation.

Scheme	Kinematic	Static	Frequency
D-F	Nominal	Nominal	B1I/B3I
T-F	Nominal	Nominal	B1I/B3I/B2a
Q-F	Nominal	Nominal	B1I/B3I/B1C/B2a
D-F	Quaternion	Quaternion	B1I/B3I
T-F	Quaternion	Quaternion	B1I/B3I/B2a
Q-F	Quaternion	Quaternion	B1I/B3I/B1C/B2a

Using the nominal and quaternion processing schemes, the float ambiguities for different satellites for BDS-3 and Galileo were estimated for the test period. This was performed to identify the contribution of individual satellites to the positioning solution. To establish a general idea for the overall performance of the model, the STD of the

float ambiguities for each satellite was used to assess the quality and reliability of the solution. Taking the quad-frequency solution as an example, Figures 5.7 and 5.5 illustrate the IF and WL STD of the float ambiguities for BDS-3 and Galileo using nominal and quaternions, respectively. In both figures, the IF and WL are shown in blue and red colours, respectively. As can be seen, the IF float ambiguities were estimated with a STD of about 0.069 cycles in both schemes. A similar trend of performance is illustrated for the WL float ambiguities using the nominal and quaternion processing schemes of about 0.021 and 0.019 cycles, respectively. Errors such as satellite clock errors can introduce uncertainties in the measurement and degrade the estimated ambiguities. Therefore, since the processing model using the nominal and attitude quaternions were subjected to similar models, the slightly better STD in the WL ambiguities derived from the PPP solution using the quaternions may indicate a better compensation of satellite clock errors as a result of accurate representation of antenna orientation, for example, in Loyer et al. (2021). The following subsections present the validation results using different frequency combinations.

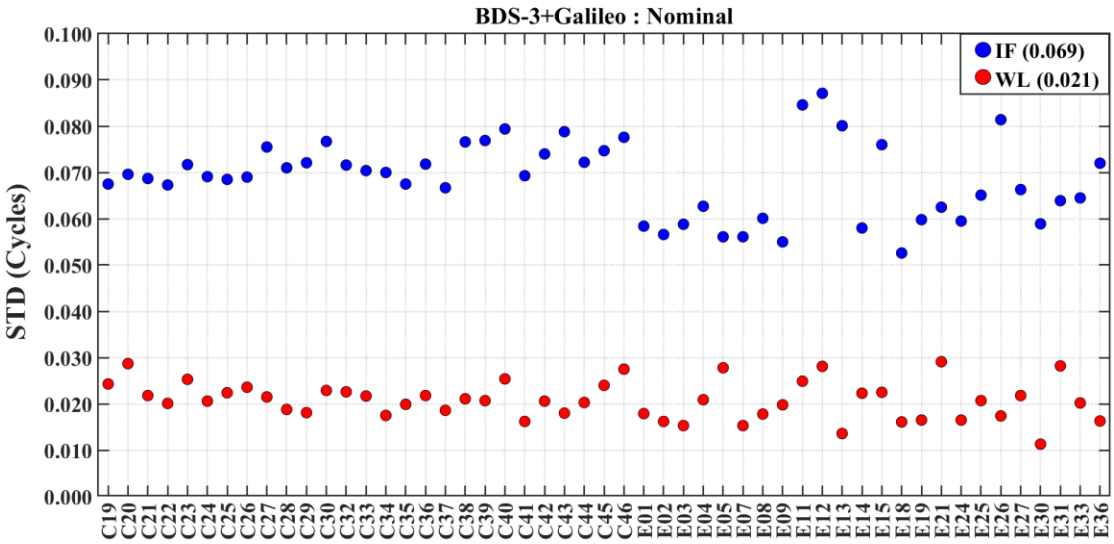

Figure 5.7: BDS-3+Galileo IF and WL standard deviations using nominal attitude.

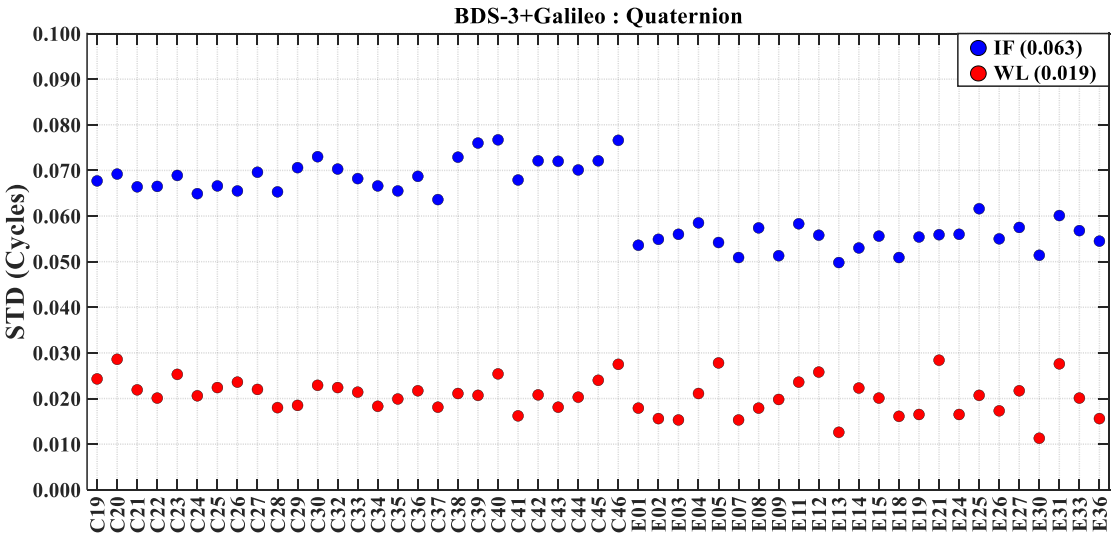

Figure 5.8: BDS-3+Galileo IF and WL standard deviations using attitude quaternions.

5.6.2 Impact of Attitude Quaternions on Position Solution

For the nominal processing strategy, the static PPP performance using the nominal and satellite attitude quaternions are shown in Figures 5.9 and 5.10, respectively. The performance is analysed in terms of North, East, and Up positioning solution, convergence time, and the corresponding performance due to the ambiguity resolution. The first subplot (left) compares the STD of the North, East, and Up positions for three schemes: D-F, T-F, and Q-F. The STD are illustrated using the bins in different colour codes for both the float and the fixed strategies.

For the position solution, the distinct colours represent the performance in different components of the two strategies (float and fixed) as shown in the legend (N, E, and U denote the North, East, and Up). The subplot in the middle compares the convergence time in minutes for the three different frequency combinations. Similar to the first panel, the different colour codes also represent the float and fixed solutions. For this one, the Y-axis represents the convergence time in minutes.

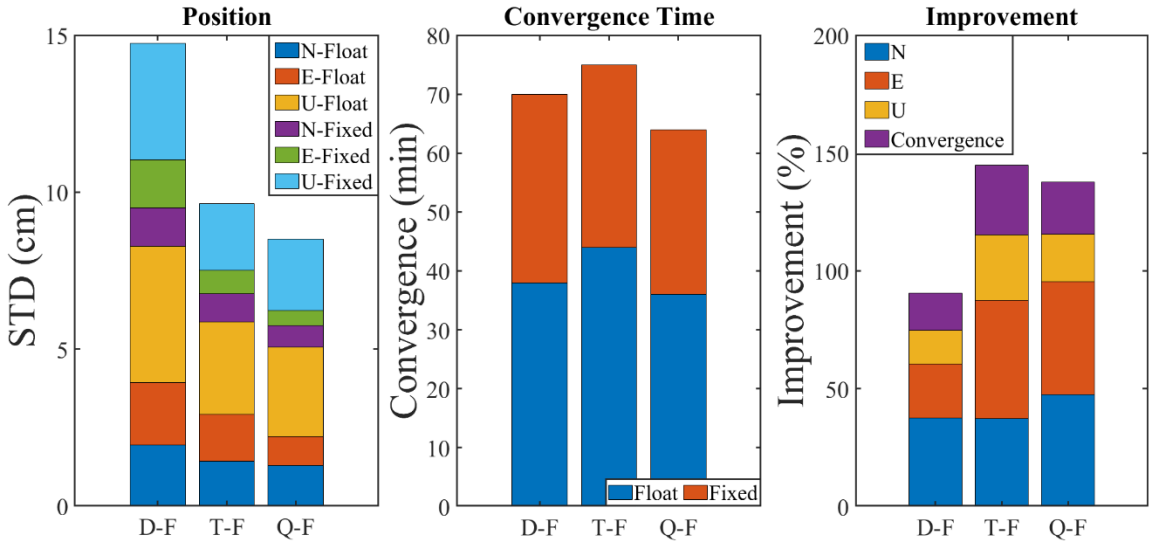

Figure 5.9: Static PPP performance using nominal attitude on different schemes.

To express the degree of influence of the proposed model, the improvement of the strategies is compared in the last panel (right). This panel expresses the improvement (%) for the North, East, Up components, and the overall convergence period.

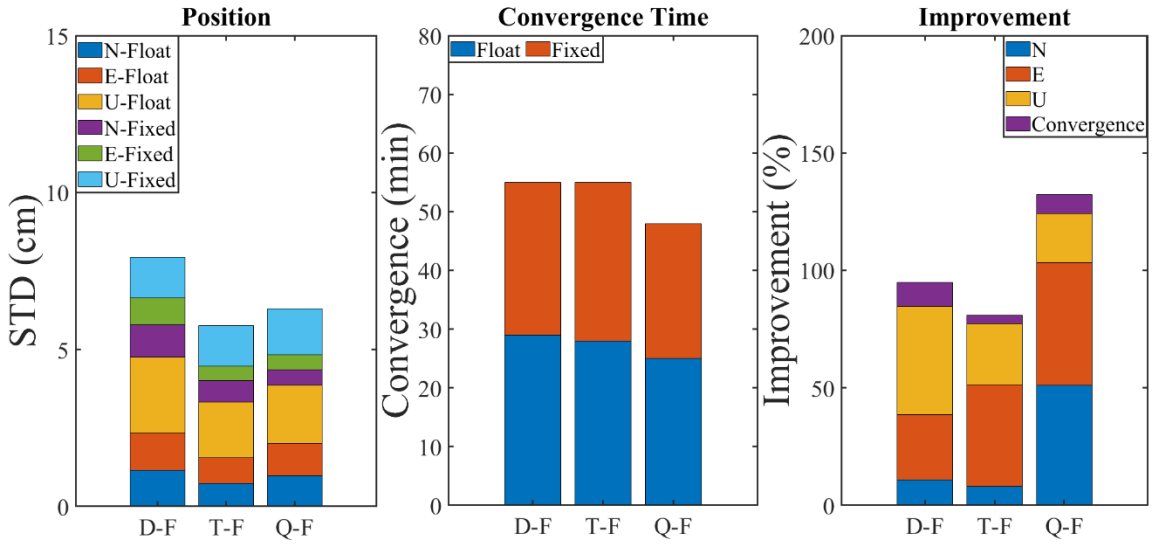

Figure 5.10: Static PPP performance using attitude quaternion on different schemes.

From the two figures, it can be observed that the approach that uses the satellite attitude quaternions exhibits lower STD values for the North, East, and Up components in both float and fixed techniques. This indicates improved accuracy and stability in position estimation compared to the first dataset. Similarly, this scheme also demonstrates lower convergence times for all three-frequency combinations, suggesting a faster convergence to achieve the desired solution than in the float solution. Additionally, the use of attitude quaternions in the ambiguity-fixed solution demonstrates higher improvement in both the positioning solution and the convergence period than the nominal approach. Moreover, the static PPP Q-F model generally outperforms the other PPP models in terms of both position solution and convergence period.

Just like the static PPP tests, the results for kinematic PPP using nominal and satellite attitude quaternions are presented in Figure 5.11 and Figure 5.12, respectively. Since the performance in the vertical component is always poorer than in the North and East components, the bins for both float and fixed solutions are the highest in Figure 5.11 and Figure 5.12. From the two figures, it is evident that the positioning performance that uses the quaternions is better than that of the nominal attitude. In the case of the convergence time, the fixed solution achieves the best in both scenarios (nominal and quaternions).

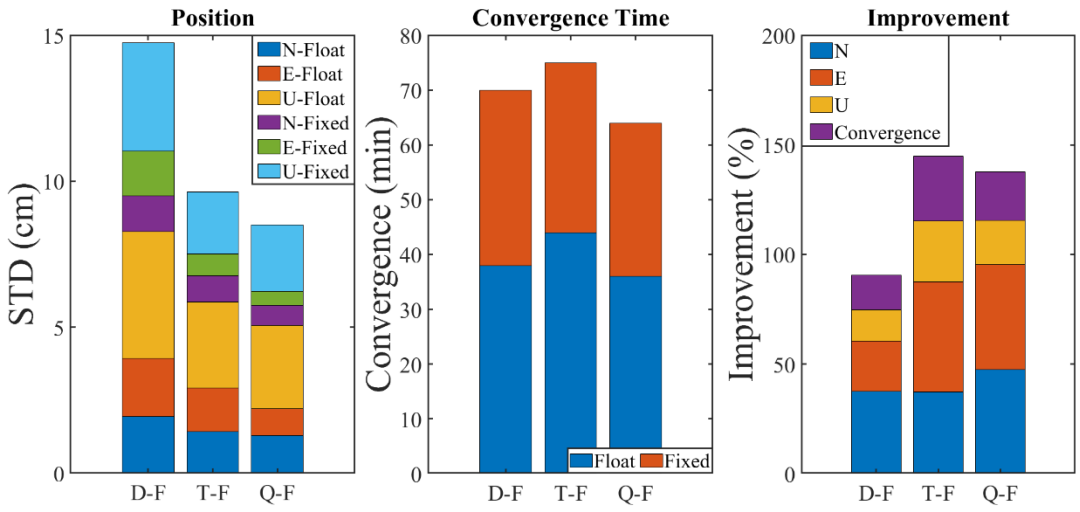

Figure 5.11: Kinematic PPP performance using nominal attitude.

Moreover, the Q-F scheme consistently demonstrates the best performance across different metrics such as positioning solution and convergence time in both nominal and quaternion approaches. Particularly, it consistently achieves smaller values in position solution, slightly shorter convergence time, and significant improvement in the North, East, and vertical component.

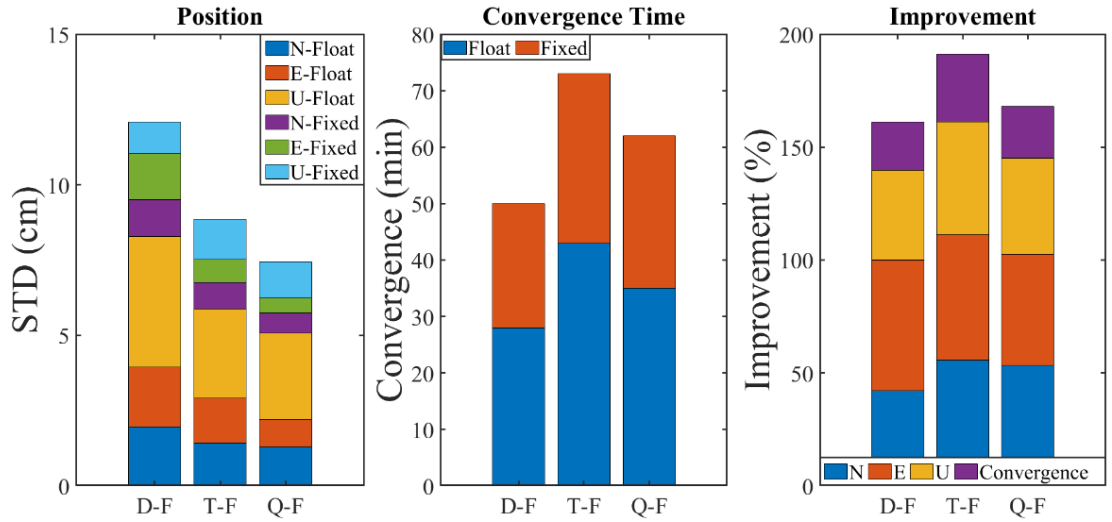

Figure 5.12: Kinematic PPP performance using attitude quaternion.

The overall better results in the Q-F scenario may be attributed to increased signal robustness in the BDS quad-frequency combination. The combination of multiple signals is an extra advantage in case signal failure. As highlighted by Geng et al. (2010), the additional frequencies provide redundant information about the unknown integer ambiguity that assists in narrowing down the ambiguity search space. In particular, the Q-F model exploits the merits of each frequency band in the Kalman filter or least squares adjustment. This means the signals provide additional independent observations that can assist in ambiguity resolution, which is a critical step in high-precision GNSS.

According to Amiri-Simkooei et al. (2016), the correlation between integer ambiguities at distinct frequencies can be reduced by employing multi-frequency signals. That is to say, the decorrelation permits for independent measurements thereby increasing the success rate of integer ambiguity in carrier phase observations. Here, it is worth mentioning that multi-frequency signals offer benefits in float solutions; in that, they increase the number of observations in the processing model.

As mentioned in Chapter 1, Galileo constellation offers quad- or more frequency signals just like BDS. As such, this Chapter validates the quad-PPP positioning solution for BDS with Galileo constellation. Figures 5.13 and 5.14 compare the Q-F PPP positioning solutions processing with the nominal and attitude quaternions strategies for BDS and Galileo, respectively. The correlation in BDS is positive (with correlation coefficient of about 0.92), with the nominal and quaternion schemes scoring averages (3D solutions) of approximately 1.66 and 1.70 cm, respectively. Similarly, Galileo registers a positive correlation of about 0.96, and averages of about 1.70 and 1.75 cm in 3D position for nominal and quaternion schemes, respectively, indicating comparable performance to BDS Q-F PPP strategy.

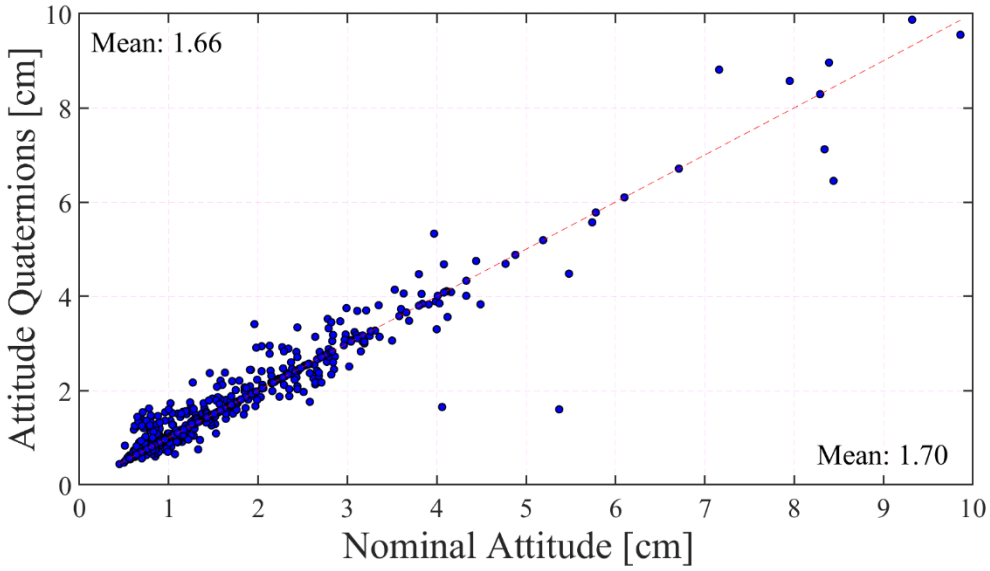

Figure 5.13: Overall positioning comparison between the nominal and attitude quaternions schemes for BDS.

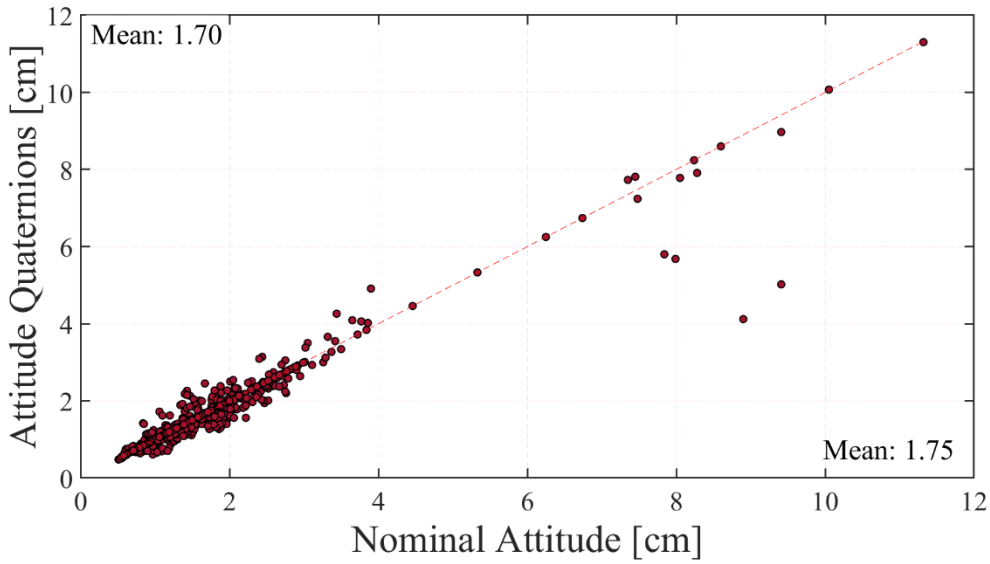

Figure 5.14: Overall positioning comparison between the nominal and attitude quaternions schemes for Galileo.

The results presented here concur with those presented in literature, for example, in a study by Loyer et al. (2021) in terms of positioning solutions. While the said study did not tackle static PPP and convergence time in the evaluation of the model, this study

unveils that considering the attitude quaternions can have a positive impact on both kinematic and static PPP solutions. This may be attributed to that the attitude geometry through the quaternions ensures improved numerical stability, thereby enabling more efficient computation for position estimation.

Furthermore, according to Schmid et al. (2015), the satellite attitude quaternions are crucial in defining the satellite antenna and the position that is necessary for GNSS data processing. This is so because, the phase observations are affected by the phase wind-up as the satellite rotates with respect to the sun as evidenced by Wu et al. (1993). Therefore, the variations in the satellite-receiver geometry caused by the satellite rotation, in trying to maintain its orientation to the direction of the sun, can be mitigated. Thus, this form of compensation assists in aligning the phase observations from various epochs, thereby improving the consistency of the observations, and in turn, assisting the ambiguity resolution.

5.6.3 Impact of Attitude Quaternions on Estimated Residuals

One application of the attitude quaternions is that they can be used to account for any misalignment between the receiver antenna and the reference datum used for data processing. Any misalignment can introduce systematic errors in the pseudorange and carrier phase observations, leading to increased measurement residuals. Therefore, by estimating and compensating for this misalignment through the attitude modelling, the impact on residuals can be investigated. In this section, the residuals on both phase and code observations are evaluated.

To investigate the impact of attitude modelling, observations from ABMF00GLP station located in Les Abymes (Guadeloupe) on DOY 100 in 2022 is used as an example. This station is equipped with a SEPT POLARX5 receiver, and it can track multi-frequency BDS and Galileo observations. Figures 5.15 and 5.16 depict the phase and code residuals for distinguish processing schemes using BDS and Galileo constellations, respectively.

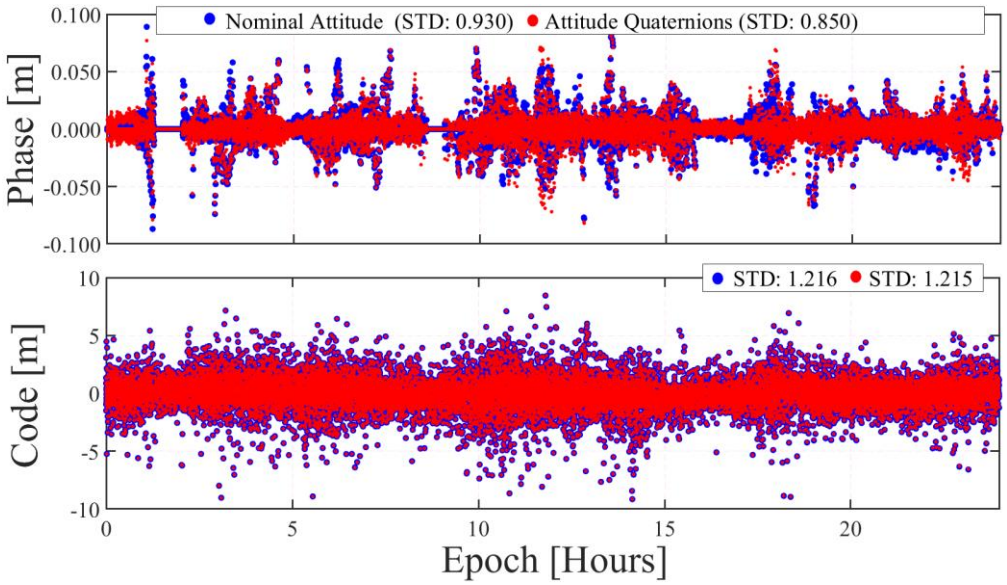

Figure 5.15: BDS phase and code residuals from different processing schemes.

In both figures, the dots are the estimated residuals for different satellite PRN. The different colours are used to distinguish the performance between the nominal (blue) and satellite attitude quaternions (red) processing schemes. The BDS time series illustrates a slight change in the STD for the estimated residuals between the nominal and quaternions schemes. The results in the two plots demonstrate apparent numerical variation as the STD for the phase residuals change from 0.93 to 0.85 m due to the application of the attitude quaternions. On the other hand, the code residuals have no meaningful change between the nominal and quaternion processing strategies, for example, the STD are pegged at around 1.22 m in both. The situation is also similar for

Galileo constellation where the phase residuals exhibit no valid change (from 0.97 to 0.94 m), and completely no change in the code residuals.

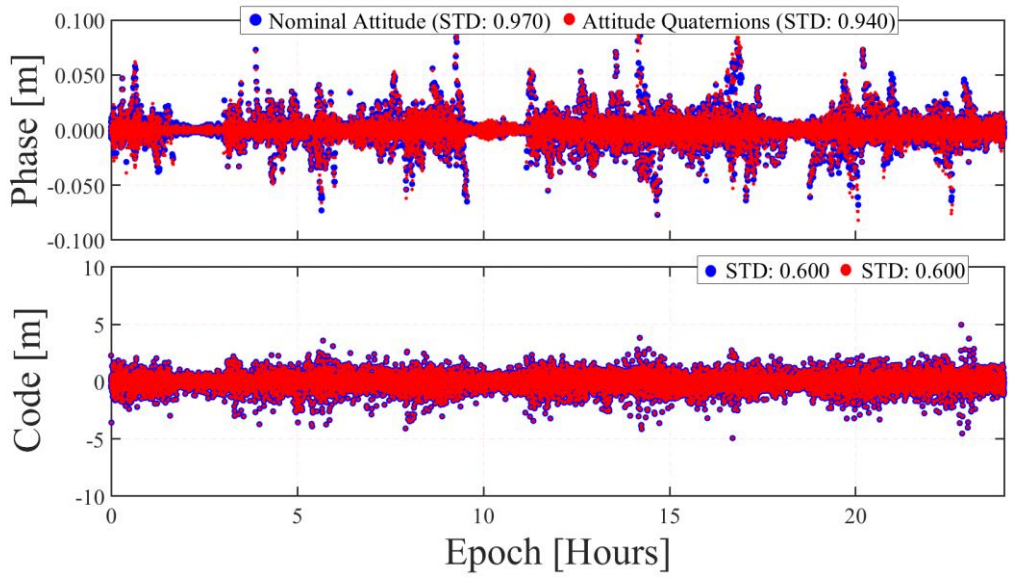

Figure 5.16: Galileo phase and code residuals from different processing schemes.

5.6.4 PPP during Satellite Eclipse Seasons

The initial sections of this Chapter highlighted that quaternions serve in satellite position calculations. However, it is crucial to recognise that satellite orientation undergoes changes during eclipse periods. Thus, this section evaluates the impact of satellite orientation on PPP during eclipsing seasons, considering both data processing with and without satellite attitude quaternions.

For illustrative purposes, the AJAC station, equipped with a LEICA GR50 receiver and TRM115000.00 antenna, is utilised. The station, also identified as AJAC00FRA in a lengthy filename nomeclature, is situated in Ajaccio in France, at a latitude of 41.927° and a longitude of 8.763°. Figures 5.17 and 5.18 illustrate positioning solutions for BDS-3 and Galileo using the AJAC station on DOY 118, 2022.

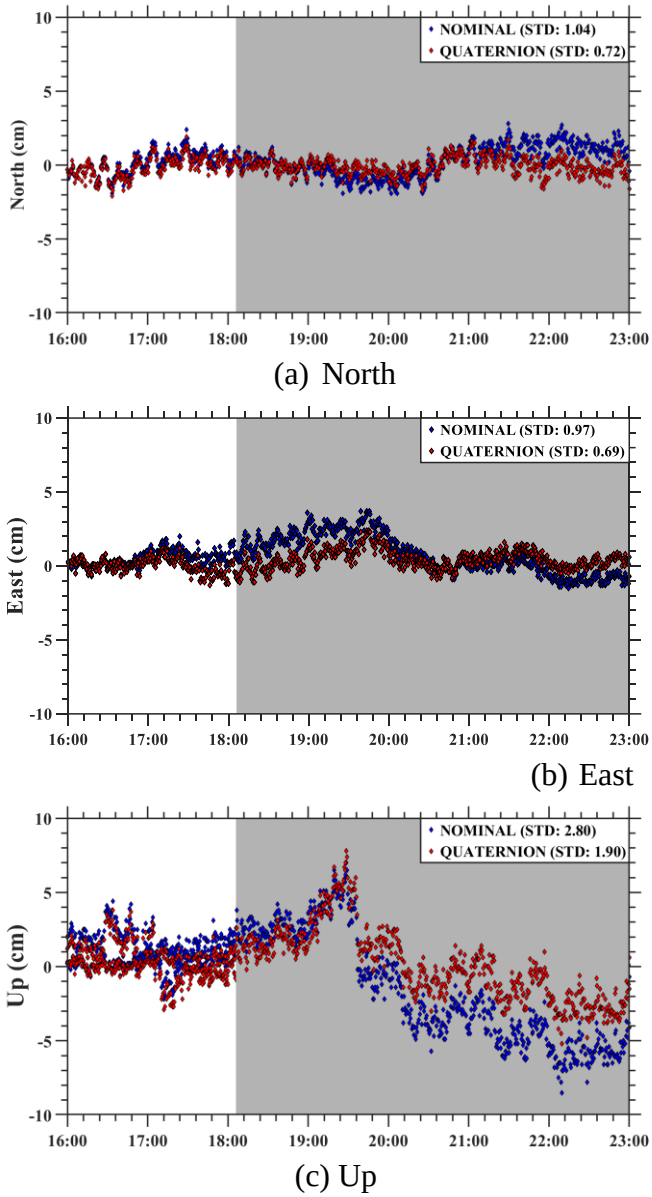

Figure 5.17: BDS-3 positioning accuracy at AJAC station.

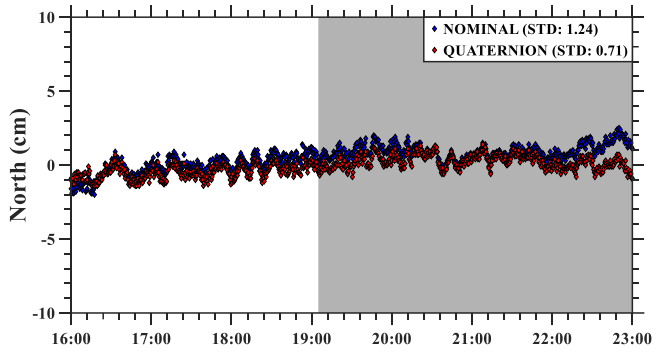

(a) North

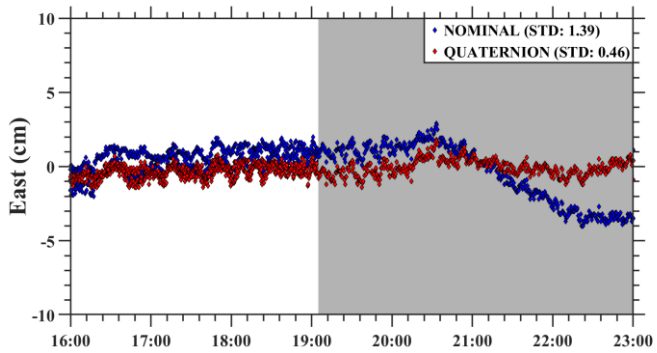

(b) East

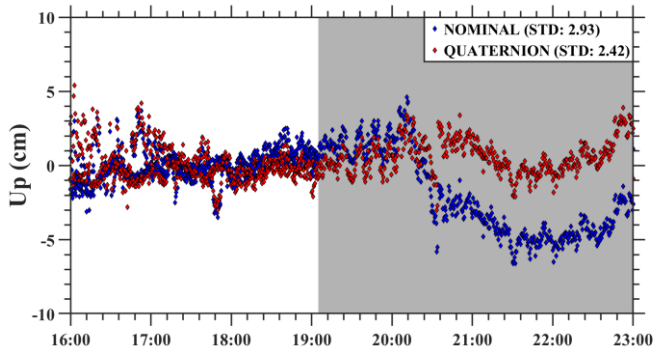

(c) Up

Figure 5.18: Galileo positioning accuracy at AJAC station.

In these figures, the blue and red diamonds represent nominal and quaternion solutions, respectively, with shaded regions indicating satellite eclipse seasons. The C46 and E36 define the shaded regions for BDS-3 and Galileo, respectively. For BDS-3, solutions without quaternions result in errors of 1.04 cm, 0.97 cm, and 2.80 cm in the North, East, and Up components. The quaternion-based solutions improve these to 0.72 cm, 0.69 cm, and 1.90 cm in the respective directions, marking improvements of approximately 30.77%, 28.87%, and 32.14%. Conversely, Galileo exhibits slightly larger standard

deviations (STD) of 1.24 cm, 1.39 cm, and 2.93 cm in the North, East, and Up components. Using quaternions improves Galileo solutions to 0.71 cm, 0.46 cm, and 2.42 cm in the North, East, and Up directions, showing improvements of about 42.74%, 66.91%, and 17.42%, respectively.

The AJAC station was also employed as an example to assess the influence of the eclipsing season on the estimated residuals. Figures 5.19 and 5.20 illustrate code residuals observed at AJAC station on DOY 118 in 2022 for BDS-3 and Galileo, employing both nominal and satellite attitude quaternions. In both figures, the upper panels depict solutions with nominal attitude, while the lower panels show solutions with attitude quaternions. The colour bars indicate STDs for the estimated residuals, and the gray zones highlight eclipsing periods for the C46 and E36 satellites in BDS-3 and Galileo, respectively.

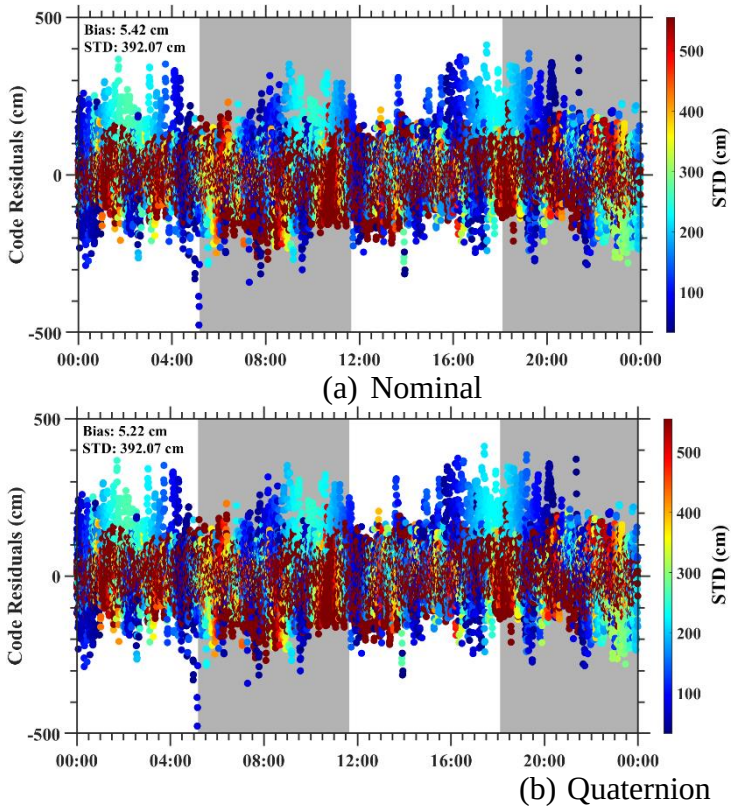

Figure 5.19: BDS-3 pseudorange residuals using nominal and quaternion.

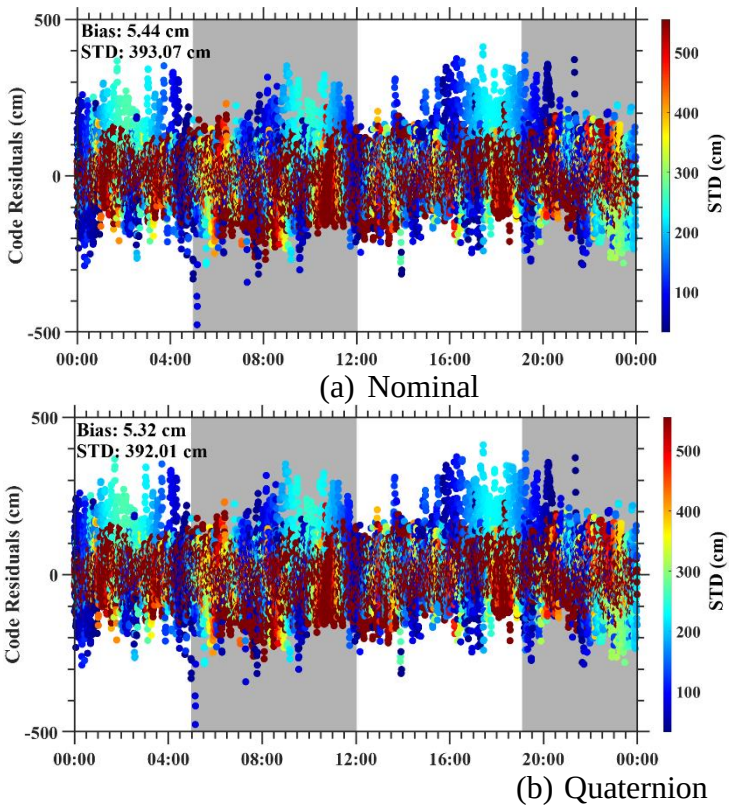

Figure 5.20: Galileo pseudorange residuals using nominal and quaternion.

For BDS-3, employing nominal schemes results in a bias of approximately 5.42 cm and a substantial STD of around 392.07 cm (Figure 5.19). Introducing quaternions does not notably affect the STD for BDS-3 estimated code residuals, although it slightly improves the bias for pseudorange residuals, yielding an STD of about 5.22 cm (Figure 5.19). Turning to Galileo, adopting nominal attitude leads to a bias of -1.55 cm and an STD of 407.71 cm (Figure 5.20). Conversely, employing attitude quaternions results in slightly better outcomes, with a bias and STD of -1.52 cm and 407.69 cm (Figure 5.20), respectively. Despite Galileo exhibiting a larger magnitude of STD, their estimated STD proves marginally superior to that of BDS-3 in both processing schemes.

In addition to evaluating code residuals, an examination of carrier phase residuals was conducted. Figure 5.21 illustrates carrier phase residuals estimated during distinct time intervals: from 07:00 to 14:00 hrs (upper panel) for BDS-3 and from 10:00 to 17:00 hrs (lower panel) for Galileo. The solutions for nominal and quaternion schemes are denoted by blue and red diamonds, respectively. The violet line represents the satellite elevation angle (C46 and E36 for BDS-3 and Galileo, respectively). Notably, utilising both nominal and quaternion processing methods yields nearly identical fluctuations in the carrier phase time series for both satellite systems. Despite the stability in these time series, a slight variation exists in the estimated averages.

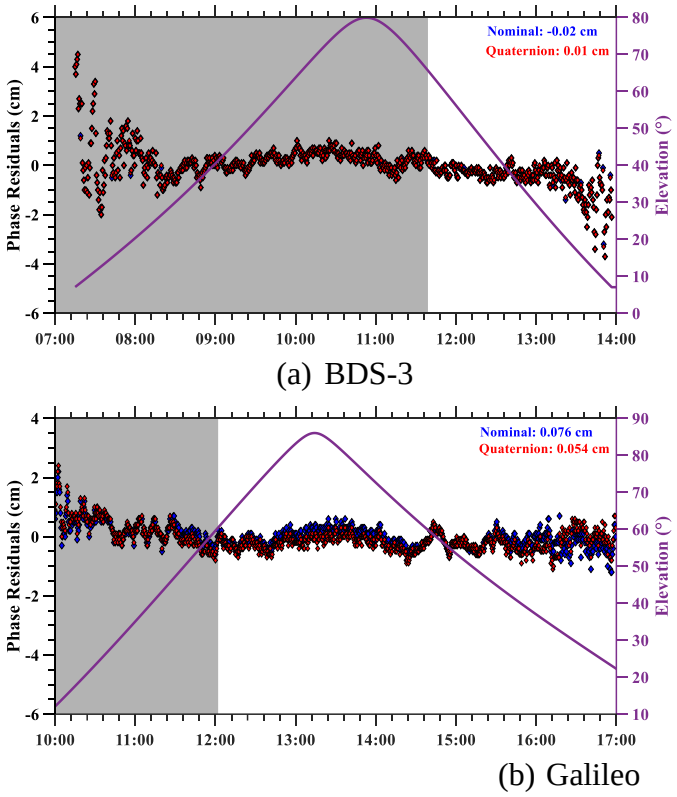

Figure 5.21: BDS-3 and Galileo carrier phase residuals during ecliping period.

5.7 Chapter Summary

This chapter focused on the influence of the satellite attitude on GNSS data processing. The treatment of biases in the PPP estimation model is revisited in terms of attitude modelling. The impact of biases in multi-frequency observations is evaluated by considering different attitude modelling. To better understand the characteristics of biases, the traditional dual-frequency PPP model is modified to accommodate the satellite attitude quaternions. Furthermore, the model is validated using the nominal and the attitude quaternions in both kinematic and static techniques. Moreover, the influence of such modelling on the estimated residuals also is investigated. The results generally indicate that the proposed technique can improve the positioning solutions in both modes. On the other hand, the impact of the estimated residuals is minor especially on the code residuals than on the phase residuals. The next chapter summarises this thesis, and generally reiterates the relationship between different issues of this work followed by the outlook for future work.

Chapter 6: Conclusions and Future Research Work

6.1 Introduction

The new satellites and signals bring about outstanding opportunities such as in PPP ambiguity resolution, convergence time, and robust positioning performance. However, multiple satellite constellations need appropriate mathematical models for combining satellites belonging to distinct systems. Moreover, multiple signals also attract unnecessary biases which require proper treatment in GNSS data processing. This chapter presents the brief conclusions and outlook on the positioning algorithms for addressing the aforementioned challenges.

6.2 Conclusions

The goal of modelling biases in GNSS data processing has been achieved in this thesis. To enhance compatibility and interoperability in multi-constellation GNSS, the combined processing is necessary. To account for differences existing between BDS-2 and BDS-3, this work accomplished the combined data processing through the introduction of the ISB. In particular, a mathematical model is developed for estimating the ISB using different MGEX precise products. The accurate knowledge of satellite orbits is essential for determining the temporal locations of satellite. The satellites are equipped with onboard clocks that enable precise timing synchronisation. Therefore, the orbits and clock products that support GEO, IGSO, and MEO satellites are carefully investigated before recommending an optimal processing scheme for BDS data processing. The experimental tests with real data have revealed that the effect of the ISB is more significant on the pseudorange than carrier phase observations.

Having developed the mathematical model for estimating ISB, the model for handling hardware biases has also been proposed. To ultimately have better positioning solutions, this research parameterised the multi-frequency PPP algorithm for handling the

hardware biases. The characteristics of such biases have been demonstrated both theoretically and practically. Just like BDS, Galileo can also broadcast multiple frequency signals, as such, numerical verification is conducted by using both BDS and Galileo constellations. Multipath can introduce errors and distortions in the received signals, leading to inaccurate solutions. Before the signal bias estimation, the multipath errors are evaluated. It is unveiled that the modernised signals for both BDS-3 and Galileo have the least multipath and noise. Furthermore, the variation in the estimated OSB between BDS-3 and Galileo constellation has been examined. The impact of the OSB corrections on positioning solution has been compared between BDS-3 and Galileo constellations. This thesis has established that the BDS-3 suffers more than Galileo from the lack of quad-frequency tracking stations. Despite that, the quad-frequency model performs better than the dual-frequency strategy using the available data from the existing MGEX network.

Accurate knowledge and modelling of satellite orientation are essential for precise GNSS data processing. The inaccurate modelling of the satellite attitude introduces errors that in turn affect the satellite clocks. The high-precision data processing is characterised by the application of precise clocks to account for that. The IGS has standard attitude models for different constellations to account for attitude errors. Currently, satellite attitude quaternions are an alternative product for addressing errors emanating from satellite orientation. This thesis has illustrated the impact of considering such products in PPP in addition to the clocks and OSB products. The experimental validation using BDS and Galileo observations has indicated that the proposed technique affects the phase residuals more than the pseudorange residuals.

6.3 Future Research Work

The work in this thesis is limited to the BDS constellation and most of the tests are conducted using its observations. While the proposed models are meant for BDS, they can also be applied to the other GNSS constellations with the CDMA signal structure.

Therefore, in addition to what is presented in this thesis, the following may be considered for further research.

Having established the ISB parameterisation in BDS, the model may be revised to address the other GNSS systems. As such, another research dimension could be exploring the characteristics of ISB between BDS and the other GNSS constellations, considering different signal structures, receiver configurations, and environmental factors.

The other part of this thesis involved an investigation of the BDS hardware biases. Due to the availability of bias products generated by different ACs, another potential research direction could be exploring the potential of using machine learning algorithms in the estimation and correction for such biases in GNSS data processing.

The use of satellite attitude quaternions in modelling satellite orientation is still at its early stage in the GNSS community. Therefore, another study could involve developing calibration techniques specific to the estimation of satellite orientation using quaternions. This could be used for modelling biases and noise in satellite observations. Since BDS-3 is still new, this could be a fundamental step towards the investigation of the solar radiation pressure for BDS precise orbit determination.

The algorithms developed in this thesis apply to smartphone data, including data collected from GPS watches. However, it is important to note that the characteristics of the GNSS measurements made influence the quality and type of the estimated solution. Smartphones are equipped with low-cost chips and antennas, typically providing low-quality measurements. In the context of this work, the focus was on novel PPP performance using geodetic-grade GPS receivers. The smartphone datasets were not considered. Therefore, this presents another possibility for further research to exploit the PPP performance using Android data.

The forthcoming Galileo High-Accuracy Service (HAS) has the potential to significantly enhance the popularity of PPP. With Galileo HAS offering real-time improved user positioning performances down to a decimetre level in ideal conditions, and based on a user PPP processing algorithm, the future outlook for PPP is promising. It is poised to emerge as, at a minimum, a competitive alternative to the currently market-leading relative positioning methods and dense reference networks. There is even the possibility that multi-GNSS PPP could eventually surpass these dominant relative positioning techniques. Hence, another research direction in multi-GNSS and multi-frequency PPP involves developing algorithms to exploit the high-accuracy augmentation services.

References

Amiri-Simkooei, A.R., Jazaeri, S., Zangeneh-Nejad, F. and Asgari, J. (2016). Role of stochastic model on GPS integer ambiguity resolution success rate. *GPS Solutions*, 20(1), pp. 51- 61. https://doi.org/10.1007/s10291-015-0445-5.

Banville, S., Geng, J., Loyer, S., Schaer, S., Springer, T. and Strasser, S., (2020). On the interoperability of IGS products for precise point positioning with ambiguity resolution. *Journal of Geodesy*, 94(1). 1-5. https://doi.org/10.1007/s00190-019-01335-w.

Bock, H., Dach, R., Jäggi, A. and Beutler, G., (2009). High-rate GPS clock corrections from CODE: support of 1 Hz applications. *Journal of Geodesy*, 83, pp.1083-1094. https://doi.org/10.1007/s00190-009-0326-1.

Böhm, J., Heinkelmann, R. and Schuh, H., (2007). Short note: a global model of pressure and temperature for geodetic applications. *Journal of Geodesy*, 81, pp.679-683. https://doi.org/10.1007/s00190-007-0135-3.

Boehm, J., Werl, B. and Schuh, H., (2006). Troposphere mapping functions for GPS and very long baseline interferometry from European Centre for Medium-Range Weather Forecasts operational analysis data. *Journal of Geophysical Research: Solid earth*, *111*(B2). https://doi.org/10.1029/2005JB003629.

Böhm, J., Niell, A., Tregoning, P. and Schuh, H., (2006). Global Mapping Function (GMF): A new empirical mapping function based on numerical weather model data. *Geophysical research letters*, *33*(7). p.L07304. doi:10.1029/2005GL025546.

Cai, C. and Gao, Y., (2013). Modeling and assessment of combined GPS/GLONASS precise point positioning. *GPS Solutions*, *17*, pp.223-236. https://doi.org/10.1007/s10291-012-0273-9.

Chen, J., Zhang, Y., Wang, J., Yang, S., Dong, D., Wang, J., Qu, W. and Wu, B., (2015). A simplified and unified model of multi-GNSS precise point positioning. *Advances in Space Research*, *55*(1), pp.125-134. https://doi.org/10.1016/j.asr.2014.10.002.

Choy, S., Bisnath, S. and Rizos, C., (2017). Uncovering common misconceptions in GNSS Precise Point Positioning and its future prospect. *GPS Solutions*, *21*, pp.13-22. https://doi.org/10.1007/s10291-016-0545-x.

CNES (2020). CNES, PPP-Wizard Project, Centre National D'Etudes Spatiales (CNES), CNES. Available at: http://www.ppp-wizard.net/products/%7BREAL-TIME%7D/ (Accessed: 11 November 2020).

CNSO (2017). BeiDou Navigation Satellite System Signal in space interface control document open service signal B2a (version 1.0). China Satellite Navigation Office. http://en.beidou.gov.cn/.

CNSO (2019). BeiDou navigation satellite system signal in space interface control document open service signal B1I (Version 1.0). China Satellite Navigation Office. http://en.beidou.gov.cn/

CNSO (2020). The BDS-3 Constellation Deployment Is Fully Completed Six Months Ahead of Schedule UNOOSA Sends a Congratulation Letter, BeiDou Navigation Satellite System (BNSS). Available at: http://en.beidou.gov.cn/ (Accessed: 23 June 2020).

CNSO (2023). BeiDou System Status — Constellation Status, China Satellite Navigation System Management Office Test Evaluation Research Center. Available at: http://www.csno-tarc.cn/system/constellation (Accessed: 23 May 2023).

CSNO (2022). Testing and Evaluation Research Center of China Satellite Navigation System, Current Location: Service Performance - Space Signal Accuracy. Available at: http://www.csno-tarc.cn/performance/sisre (Accessed: 8 July 2022).

Dai, X., Ge, M., Lou, Y., Shi, C., Wickert, J. and Schuh, H., (2015). Estimating the yaw-attitude of BDS IGSO and MEO satellites. *Journal of Geodesy*, *89*, pp.1005-1018. https://doi.org/10.1007/s00190-015-0829-x.

Deng, Z., Fritsche, M., Uhlemann, M., Wickert, J. and Schuh, H., (2016). Reprocessing of GFZ multi-GNSS product GBM. In *IGS workshop* (pp. 08-12). Feb. 2016, Sydney Australia.

Dilssner, F., Laufer, G., Springer, T., Schonemann, E. and Enderle, W., (2018). The BeiDou attitude model for continuous yawing MEO and IGSO spacecraft. *Presentation, EGU General Assembly*.

El-Mowafy, A., Deo, M. and Rizos, C., (2016). On biases in precise point positioning with multi-constellation and multi-frequency GNSS data. *Measurement Science and Technology*, *27*(3), p.035102. https://doi.org/10.1088/0957-0233/27/3/035102.

Fan, L., Shi, C., Li, M., Wang, C., Zheng, F., Jing, G. and Zhang, J., (2019). GPS satellite inter-frequency clock bias estimation using triple-frequency raw observations. *Journal of Geodesy*, *93*, pp.2465-2479. https://doi.org/10.1007/s00190-019-01310-5.

Ge, M., Chen, J., Douša, J., Gendt, G. and Wickert, J., (2012). A computationally efficient approach for estimating high-rate satellite clock corrections in realtime. *GPS Solutions*, *16*, pp.9-17. https://doi.org/10.1007/s10291-011-0206-z.

Geng, J., Meng, X., Dodson, A.H. and Teferle, F.N., (2010). Integer ambiguity resolution in precise point positioning: method comparison. *Journal of Geodesy*, *84*, pp.569-581. https://doi.org/10.1007/s00190-010-0399-x.

Geng, J., Meng, X., Dodson, A.H., Ge, M. and Teferle, F.N., (2010). Rapid re-convergences to ambiguity-fixed solutions in precise point positioning. *Journal of Geodesy*, *84*, pp.705-714. https://doi.org/10.1007/s00190-010-0404-4.

Geng, J., Chen, X., Pan, Y. and Zhao, Q., (2019). A modified phase clock/bias model to improve PPP ambiguity resolution at Wuhan University. *Journal of Geodesy*, *93*, pp.2053-2067. https://doi.org/10.1007/s00190-019-01301-6.

Geng, J., Wen, Q., Zhang, Q., Li, G. and Zhang, K., (2022). GNSS observable-specific phase biases for all-frequency PPP ambiguity resolution. *Journal of Geodesy*, *96*(2), p.1-18. https://doi.org/10.1007/s00190-022-01602-3.

Geng, J. and Bock, Y., (2016). GLONASS fractional-cycle bias estimation across inhomogeneous receivers for PPP ambiguity resolution. *Journal of Geodesy*, *90*(4), pp.379-396. https://doi.org/10.1007/s00190-010-0404-4.

Gleason, S. and Gebre-Egziabher, D. (2009). GNSS Applications and Methods. Artech House, Norwood, MA.

Guo, F., Zhang, X., Wang, J. and Ren, X., (2016). Modeling and assessment of triple-frequency BDS precise point positioning. *Journal of Geodesy*, *90*, pp.1223-1235. https://doi.org/10.1007/s00190-016-0920-y.

Guo, J. and Geng, J., (2018). GPS satellite clock determination in case of inter-frequency clock biases for triple-frequency precise point positioning. *Journal of Geodesy*, *92*(10), pp.1133-1142. https://doi.org/10.1007/s00190-017-1106-y

Gu, S., Lou, Y., Shi, C. and Liu, J., (2015). BeiDou phase bias estimation and its application in precise point positioning with triple-frequency observable. *Journal of Geodesy*, *89*(10), pp.979-992. https://doi.org/10.1007/s00190-015-0827-z.

Hauschild, A. and Montenbruck, O., (2009). Kalman-filter-based GPS clock estimation for near real-time positioning. *GPS Solutions*, *13*, pp.173-182. https://doi.org/10.1007/s10291-008-0110-3.

Ishijima, Y., Inaba, N., Matsumoto, A., Terada, K., Yonechi, H., Ebisutani, H., Ukawa, S. and Okamoto, T., (2009), March. Design and development of the first Quasi-Zenith satellite attitude and orbit control system. In *2009 IEEE Aerospace Conference* (pp. 1-8). IEEE. https://doi.org/10.1109/AERO.2009.4839537.

Jiao, G., Song, S. and Jiao, W., (2019). Improving BDS-2 and BDS-3 joint precise point positioning with time delay bias estimation. *Measurement Science and Technology*, *31*(2), p.025001. https://doi.org/10.1088/1361-6501/ab41cf.

Karaim, M., Elghamrawy, H., Tamazin, M. and Noureldin, A., (2017), December. Investigation of the effects of White Gaussian Noise jamming on commercial GNSS receivers. In *2017 12th International Conference on Computer Engineering and Systems (ICCES)* (pp. 468-472). IEEE. https://doi.org/10.1109/ICCES.2017.8275353.

Kazmierski, K., Sośnica, K. and Hadas, T., (2018). Quality assessment of multi-GNSS orbits and clocks for real-time precise point positioning. *GPS Solutions*, *22*, pp.1-12. https://doi.org/10.1007/s10291-017-0678-6.

Kazmierski, K., Zajdel, R. and Sośnica, K., (2020). Evolution of orbit and clock quality for real-time multi-GNSS solutions. *GPS Solutions*, *24*(4), p.111. https://doi.org/10.1007/s10291-020-01026-6.

Kouba, J., (2009). A guide to using International GNSS Service (IGS) products. Geodetic Survey Division Natural Resources Canada Ottawa. Available at: http://graypantherssf.igs.org/igscb/resource/pubs/UsingIGSProductsVer21.pdf.

Laurichesse, D. and Blot, A., (2016). Fast PPP convergence using multi-constellation and triple-frequency ambiguity resolution. In *Proceedings of the 29th International Technical Meeting of The Satellite Division of the Institute of Navigation (ION GNSS+ 2016)* (pp. 2082-2088). https://doi.org/10.33012/2016.14633.

Leick, A., Rapoport, L. and Tatarnikov, D. (2015). GPS Satellite Surveying. Fourth Edition. John Wiley & Sons.

Li, H., Zhou, X., Wu, B. and Wang, J., (2012). Estimation of the inter-frequency clock bias for the satellites of PRN25 and PRN01. *Science China Physics, Mechanics and Astronomy*, *55*, pp.2186-2193. https://doi.org/10.1007/s11433-012-4897-0.

Li, H., Chen, Y., Wu, B., Hu, X., He, F., Tang, G. and Chen, J., (2013). Modeling and initial assessment of the inter-frequency clock bias for COMPASS GEO satellites. *Advances in Space Research*, *51*(12), pp.2277-2284. https://doi.org/10.1016/j.asr.2013.02.012.

Li, H., Li, B., Xiao, G., Wang, J. and Xu, T., (2016). Improved method for estimating the inter-frequency satellite clock bias of triple-frequency GPS. *GPS Solutions*, *20*, pp.751-760. https://doi.org/10.1007/s10291-015-0486-9.

Li, M., Zhang, B., Yuan, Y. and Zhao, C., (2019). Single-frequency precise point positioning (PPP) for retrieving ionospheric TEC from BDS B1 data. *GPS Solutions*, *23*, pp.1-11. https://doi.org/10.1007/s10291-018-0810-2.

Li, P., Zhang, X., Ge, M. and Schuh, H., (2018). Three-frequency BDS precise point positioning ambiguity resolution based on raw observables. *Journal of Geodesy*, *92*, pp.1357-1369. https://doi.org/10.1007/s00190-018-1125-3.

Li, P. and Zhang, X., (2014). Integrating GPS and GLONASS to accelerate convergence and initialization times of precise point positioning. *GPS Solutions*, *18*, pp.461-471. https://doi.org/10.1007/s10291-013-0345-5.

Liu, X., Jiang, W., Chen, H., Zhao, W., Huo, L., Huang, L. and Chen, Q., (2019). An analysis of inter-system biases in BDS/GPS precise point positioning. *GPS Solutions*, *23*(4), p.1-14. https://doi.org/10.1007/s10291-019-0906-3.

Liu, Y., Song, W., Lou, Y., Ye, S. and Zhang, R., (2017). GLONASS phase bias estimation and its PPP ambiguity resolution using homogeneous receivers. *GPS Solutions*, *21*, pp.427-437. 10.1007/s10291-016-0529-x

Lou, Y., Zheng, F., Gu, S., Wang, C., Guo, H. and Feng, Y., (2016). Multi-GNSS precise point positioning with raw single-frequency and dual-frequency measurement models. *GPS Solutions*, *20*, pp.849-862. https://doi.org/10.1007/s10291-015-0495-8.

Loyer, S., Banville, S., Geng, J. and Strasser, S., (2021). Exchanging satellite attitude quaternions for improved GNSS data processing consistency. *Advances in Space Research*, *68*(6), pp.2441-2452. https://doi.org/10.1016/j.asr.2021.04.049.

Lu, M., Li, W., Yao, Z. and Cui, X., (2019). Overview of BDS III new signals. *Navigation*, *66*(1), pp.19-35. https://doi.org/10.1002/navi.296.

Mi, X., Zhang, B., Odolinski, R. and Yuan, Y., (2020). On the temperature sensitivity of multi-GNSS intra-and inter-system biases and the impact on RTK positioning. *GPS Solutions*, *24*, pp.1-14. https://doi.org/10.1007/s10291-020-01027-5.

Montenbruck, O., Hugentobler, U., Dach, R., Steigenberger, P. and Hauschild, A., (2012). Apparent clock variations of the Block IIF-1 (SVN62) GPS satellite. *GPS Solutions*, *16*, pp.303-313. 10.1007/s10291-011-0232-x.

Montenbruck, O., Hauschild, A., Steigenberger, P., Hugentobler, U., Teunissen, P. and Nakamura, S., (2013). Initial assessment of the COMPASS/BeiDou-2 regional navigation satellite system. *GPS Solutions*, *17*, pp.211-222. 10.1007/s10291-012-0272-x.

Montenbruck, O., Schmid, R., Mercier, F., Steigenberger, P., Noll, C., Fatkulin, R., Kogure, S. and Ganeshan, A.S., (2015). GNSS satellite geometry and attitude models. *Advances in Space Research*, *56*(6), pp.1015-1029. https://doi.org/10.1016/j.asr.2015.06.019.

Montenbruck, O., Steigenberger, P., Prange, L., Deng, Z., Zhao, Q., Perosanz, F., Romero, I., Noll, C., Stürze, A., Weber, G. and Schmid, R., (2017). The Multi-GNSS

Experiment (MGEX) of the International GNSS Service (IGS)–achievements, prospects and challenges. *Advances in Space Research*, *59*(7), pp.1671-1697. https://doi.org/10.1016/j.asr.2017.01.011.

Montenbruck, O., Hauschild, A. and Hessels, U., (2011). Characterization of GPS/GIOVE sensor stations in the CONGO network. *GPS Solutions*, *15*, pp.193-205. https://doi.org/10.1007/s10291-010-0182-8.

Nadarajah, N., Teunissen, P.J., Sleewaegen, J.M. and Montenbruck, O., (2015). The mixed-receiver BeiDou inter-satellite-type bias and its impact on RTK positioning. *GPS Solutions*, *19*, pp.357-368. https://doi.org/10.1007/s10291-014-0392-6.

NASA (2021a). GBM is changed to Long Product File Name since GPS Week 2038, National Aeronautics and Space Administration, Available: https://www.igs.org/mgex/data-products/products/. (Accessed: 1 January 2021).

NASA (2021b). NASA's Archive of Space Geodesy Data, National Aeronautics and Space Administration, NASA. Available at: https://cddis.nasa.gov/archive/gnss/products/%0Amgex/ (Accessed: 1 January 2021).

Odijk, D., Zhang, B., Khodabandeh, A., Odolinski, R. and Teunissen, P.J., (2016). On the estimability of parameters in undifferenced, uncombined GNSS network and PPP-RTK user models by means of S-system theory. *Journal of Geodesy*, *90*(1), pp.15-44. 10.1007/s00190-015-0854-9.

Pan, L., Li, X., Zhang, X., Li, X., Lu, C., Zhao, Q. and Liu, J., (2017). Considering inter-frequency clock bias for BDS triple-frequency precise point positioning. *Remote Sensing*, *9*(7), p.734. https://doi.org/10.3390/rs9070734.

Pan, L., Xiaohong, Z. and Fei, G., (2017). Ambiguity resolved precise point positioning with GPS and BeiDou. *Journal of geodesy*, *91*, pp.25-40. https://doi.org/10.1007/s00190-016-0935-4.

Petit, G. and Luzum, B., (2010). IERS technical note no. 36. *IERS conventions*, *179*. International Earth Rotation and Reference Systems.

Saastamoinen, J., (1972). Contributions to the theory of atmospheric refraction. *Bulletin Géodésique (1946-1975)*, *105*(1), pp.279-298. https://doi.org/10.1007/BF02521844.

Schmid, R., Rothacher, M., Thaller, D. and Steigenberger, P., (2005). Absolute phase center corrections of satellite and receiver antennas: Impact on global GPS solutions and estimation of azimuthal phase center variations of the satellite antenna. *GPS Solutions*, *9*, pp.283-293. https://doi.org/10.1007/s10291-005-0134-x.

Schönemann, E., Becker, M. and Springer, T., (2011). A new approach for GNSS analysis in a multi-GNSS and multi-signal environment. *Journal of Geodetic Science*, *1*(3), pp.204-214. https://doi.org/10.2478/v10156-010-0023-2.

Senior, K.L., Ray, J.R. and Beard, R.L., (2008). Characterization of periodic variations in the GPS satellite clocks. *GPS Solutions*, *12*, pp.211-225. https://doi.org/10.1007/s10291-008-0089-9.

Shen, J. and Geng, C., (2019). Update on the BeiDou navigation satellite system (BDS). In *32nd International Technical Meeting of the Satellite Division of The Institute of Navigation (ION GNSS+ 2019)*, *Miami, FL*. https://doi.org/10.33012/2019.16901.

Shi, C., Wu, X., Zheng, F., Wang, X. and Wang, J., (2021). Modeling of BDS-2/BDS-3 single-frequency PPP with B1I and B1C signals and positioning performance analysis. *Measurement*, *178*, p.109355. https://doi.org/10.1016/j.measurement.2021.109355.

Steigenberger, P. and Montenbruck, O., (2020). Consistency of MGEX orbit and clock products. *Engineering*, *6*(8), pp.898-903. https://doi.org/10.1016/j.eng.2019.12.005.

Strode, P.R. and Groves, P.D., (2016). GNSS multipath detection using three-frequency signal-to-noise measurements. *GPS Solutions*, *20*, pp.399-412. https://doi.org/10.1007/s10291-015-0449-1.

Su, K. and Jin, S., (2021). Three Dual-Frequency Precise Point Positioning Models for the Ionospheric Modeling and Satellite Pseudorange Observable-Specific Signal Bias Estimation. *Remote Sensing*, *13*(24), p.5093. https://doi.org/10.3390/rs13245093.

Tegedor, J., Øvstedal, O. and Vigen, E., (2014). Precise orbit determination and point positioning using GPS, GLONASS, Galileo and BeiDou. 10.2478/jogs-2014-0008.

Teunissen, P.J.G. and Khodabandeh, A., (2015). Review and principles of PPP-RTK methods. *Journal of Geodesy*, *89*(3), pp.217-240. https://doi.org/10.1007/s00190-014-0771-3.

Torre, A.D. and Caporali, A., (2015). An analysis of intersystem biases for multi-GNSS positioning. *GPS Solutions*, *19*, pp.297-307. https://doi.org/10.1007/s10291-014-0388-2.

Villiger, A., Schaer, S., Dach, R., Prange, L., Sušnik, A. and Jäggi, A., (2019). Determination of GNSS pseudo-absolute code biases and their long-term combination. *Journal of Geodesy*, *93*, pp.1487-1500. https://doi.org/10.1007/s00190-019-01262-w.

Wanninger, L. and Beer, S., (2015). BeiDou satellite-induced code pseudorange variations: diagnosis and therapy. *GPS Solutions*, *19*, pp.639-648. https://doi.org/10.1007/s10291-014-0423-3.

Weber, G. and Mervart, L., (2007). The BKG Ntrip Client (BNC). In *Report on EUREF symposium*. Available: *http://epncb.eu/documentation/papers/eurefsymposium2007/.* (Accessed: 11 October 2020).

Wu, J.T., Wu, S.C., Hajj, G.A., Bertiger, W.I. and Lichten, S.M., (1992). Effects of antenna orientation on GPS carrier phase. *Astrodynamics 1991*, pp.1647-1660.

Yao, Z., Zhang, J. and Lu, M., (2016). ACE-BOC: dual-frequency constant envelope multiplexing for satellite navigation. *IEEE Transactions on Aerospace and Electronic Systems*, *52*(1), pp.466-485. 10.1109/TAES.2015.140607.

Ye, S., Zhao, L., Song, J., Chen, D. and Jiang, W., (2018). Analysis of estimated satellite clock biases and their effects on precise point positioning. *GPS Solutions*, *22*, pp.1-14. https://doi.org/10.1007/s10291-017-0680-z.

Zhang, X., Li, X. and Guo, F., (2011). Satellite clock estimation at 1 Hz for realtime kinematic PPP applications. *GPS Solutions*, *15*, pp.315-324. https://doi.org/10.1007/s10291-010-0191-7.

Zhao, L., Ye, S. and Song, J., (2017). Handling the satellite inter-frequency biases in triple-frequency observations. *Advances in space research*, *59*(8), pp.2048-2057. https://doi.org/10.1016/j.asr.2017.02.002.

Zhao, Q., Wang, G., Liu, Z., Hu, Z., Dai, Z. and Liu, J., (2016). Analysis of BeiDou satellite measurements with code multipath and geometry-free ionosphere-free combinations. *Sensors*, *16*(1), p.123. https://doi.org/10.3390/s16010123.

Zumberge, J.F., Watkins, M.M. and Webb, F.H., (1997). Characteristics and applications of precise GPS clock solutions every 30 seconds. *Navigation*, *44*(4), pp.449-456. https://doi.org/10.1002/j.2161-4296.1997.tb02360.x.